UNIVERSITÀ DEGLI STUDI DI PADOVA

Dipartimento di Ingegneria Industriale DII

Corso di Laurea Magistrale in Ingegneria Dei Materiali

Topological Optimization Studies of Ceramic Scaffolds obtained by means of Advanced Additive Manufacturing

Relatore

Prof. Enrico Bernardo

Correlatore

Prof. Dr. Nahum Travitzky

Laureando

Elia Cescon

Matr. n. 1197369

Anno Accademico 2018/2019

"I am human,
and I think nothing human is alien to me."

DECLARATION

This thesis work is the result of a collaboration between the CERAM-GLASS group of the University of Padua and the Institute of Glass and Ceramics of the Friedrich-Alexander-Universität Erlangen-Nürnberg. This work was made possible by Prof. Bernardo (University of Padua) and Prof. Dr. Nahum Travitzky (group leader for Additive Manufacturing at Friedrich-Alexander-Universität Erlangen-Nürnberg). The work was partially and forcibly stopped by the outbreak of the 2020 coronavirus pandemic (COVID-19) in March 2020.

ABSTRACT

Calcite ($CaCO_3$) is a well-known bioceramic material of great interest in the field of biomaterials for bone tissue engineering, thanks to its biocompatibility and bioactivity. The work, carried out at the University of Padua and the Friedrich-Alexander-Universität Erlangen-Nürnberg, deals with the additive manufacturing of scaffolds by means of *Direct Ink Writing* (or *robocasting*) technique, starting from pre-ceramic polymers and fillers. The final content of calcite, after pyrolysis in nitrogen at 600°C, is between 65%wt to 70%wt.

The first part aims to compare scaffolds based on two different pre-ceramic polymers, Silres MK® and Silres H44®, with the presence or absence of carbon fibers.

Subsequently, scaffolds consisting of different filament cross-sections in terms of shape and configuration are produced and compared. As a result, the extrusion of circular, square, hollow and co-extruded filaments is investigated. The thesis explores and discusses the optimization of the pre-ceramic inks and the printing parameters together with the mechanical, physical and microstructural characterization of the printed lattices.

The final purpose will be the production of bifunctional scaffolds, capable not only to promote the regeneration of new tissue, but also to kill cancerous cells by exploiting the photothermal effect of carbon fibers and "free" carbon deriving from the pyrolysis of the pre-ceramic polymer.

SOMMARIO

La calcite ($CaCO_3$) è un bioceramico che riscuote grande interesse nel campo dei biomateriali per la rigenerazione osseo-tissutale, grazie alla sua biocompatibilità e bioattività. Il lavoro, svolto presso l'Università degli Studi di Padova e la Friedrich-Alexander-Universität Erlangen-Nürnberg, affronta la manifattura additiva di scaffolds tramite la tecnologia *Direct Ink Writing* (oppure *robocasting*), partendo da polimeri pre-ceramici e fillers. Il contenuto finale di calcite, dopo pirolisi in azoto a 600°C, è compreso tra il 65% e il 70% in peso.

La prima parte dell'elaborato riguarda il confronto di scaffolds basati su due diversi polimeri pre-ceramici, Silres MK® e Silres H44®, con la presenza o meno di fibre di carbonio.

Successivamente, sono state prodotti e confrontati scaffolds formati da diffrenti sezioni trasversali del filamento in termini di forma e configurazione. Di conseguenza, è stata studiata l'estrusione di filamenti a sezione circolare, quadrata, cava, co-estrusa. La tesi esplora e discute l'ottimizzazione degli inchiostri pre-ceramici e dei parametri di stampa insieme alla caratterizzazione meccanica, fisica e microstrutturale dei reticoli stampati.

L'obiettivo finale sarà la produzione di scaffolds bifunzionali, in grado non solo di favorire la rigenerazione di nuovo tessuto, ma anche di uccidere le cellule cancerose, sfruttando l'effetto fototermico delle fibre di carbonio e del carbonio "libero"derivante dalla pirolisi del polimero pre-ceramico.

ACKNOWLEDGMENTS

Firstly, I want to thank my family for always "sponsoring" me and leaving me free to choose my path during these 5 years of study.

I want to thank Prof. Bernardo for being always available, lightning-quick and understanding, even during my stay in Germany. I want to thank Prof. Travitzky for his humanity, the *off-topic* conversations and for teaching me that *"thinking means to compare"*.

I really have to thank Hamada, always present to welcome my doubts and perplexities, and Larissa, who welcomed me to Erlangen and supervised me, leaving aside her research many times. I will always be grateful to both.

I want to thank all the people I met during the work in Padua, during my mobility in Germany and in the laboratories. Thank you to Eng. Corradini and Eng. Sottoriva for the coffee(s) together.

Then I want to thank my roommates during my years in Padua, in particular Rod, Kevin, Mauro and the other one with the "M". Thank you Alessia for motivating me during the past three years. Thank you to all my friends that made my last years unforgettable: Alice, Chiara, Enrico, Mode, Tondo, Pego, Diamantino, Pinc and all the others. Thank you Sofija for supporting me these months. Thank you to all my "friends of the sea" and thanks to all the people I forgot to thank.

Finally, thank you Padua, with your hills, for adopting me during these exciting years. You will always be with me.

... Spaziale!

CONTENTS

LIST OF FIGURES

LIST OF TABLES

1 INTRODUCTION

This chapter aims to give a context to the work presented in this thesis. After defining the objectives, the necessary background is briefly explained.

Firstly, polymer derived ceramics (PDC) are presented in terms of their chemistry and manufacturing, with a special focus on Si-derived pre-ceramic polymers.

Then, biomaterials and especially bioceramic scaffolds are discussed, making some considerations about the feature requested from the point of view of both material and geometry.

The following section will focus on photothermal effect and photothermal therapy, paying special attention to carbon-based photothermal agents.

Finally, additive manufacturing (AM) is described with a focus on direct ink writing (or robocasting) technique.

1.1 TARGETS

The development of bone tissue engineering is directly related to advances in materials science and technology. This field is highly interdisciplinary and requires knowledge going from medicine and biology to material science and mechanical engineering.
This means not only to study the interaction between implant and body from a clinical point of view, but also the inclusion of better filler materials that can be used in the reconstruction of large orthopaedic defects and then the manufacture of orthopaedic implants that are mechanically more suitable to their biological environment [1] in terms of mechanical strength, elastic modulus, surface roughness, etc.

Among all different types of biomaterials, ceramics have aroused great interest because of their high biocompatibility and bioactivity, 1.3.2. This work investigates scaffolds derived from pre-ceramic polymers and fillers, produced through additive manufacturing technologies. This work aims at two different goals. During the time spent at the University of Padua, the focus was on the comparison between two pre-ceramic precursors, Silres MK® and Silres H44®, firstly added only with calcite and then with both calcite and carbon fibers. Later, during the time spent at the Friedrich-Alexander-Universität Erlangen-Nürnberg, the goal was to produce and compare different filament cross-section shapes.

1.2 POLYMER DERIVED CERAMICS

Polymer Derived Ceramics (PDCs), as the name suggests, represents a synthesis route for the realization of ceramic components through the controlled pyrolysis of polymeric precursors [2]. The main advantage of this technique is in terms of formability with the possibility of adopting traditional plastic molding techniques and, for example, machining before ceramization avoids the problems connected to tool wear and brittle fracture. Other important advantages are the great variety and availability of precursors, their low cost and their easy handling, in addition to the relatively low synthesis temperatures, usually around 800°C in nitrogen or argon atmosphere (pyrolysis).

The following sections means to give a brief introduction to this class of polymers with a focus on silicon-based pre-ceramic polymers.

1.2.1 *Chemistry of silicon-based pre-ceramic polymers*

The general formula of a silicon-based pre-ceramic polymer is presented in fig. 1.1. It consists of Si atoms bonded to a generic X group, that defines the class of the pre-ceramic polymer.

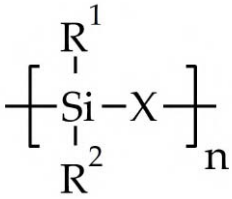

Figure 1.1: General formula of silicon-based pre-ceramic polymer.

The different classes obtainable by changing the X group are visible in fig. 1.2, while by changing the functional groups R^1 and R^2, it is possible to modify properties as the thermal stability, the solubility of the polymer and also the electronic, optical and rheological properties. These substituents are usually carbon-based e.g. hydrogen, aliphatic or aromatic groups. Then, the possibility of obtaining a wide range of possible polymeric compositions and, therefore, physical and chemical properties by combining different X, R^1 and R^2 groups represents a great advantage. Consequently, the possibility of varying and adjusting the chemical and physical macroscopical properties of PDCs, allows the design of the molecular precursor. The cited side-groups, R^1 and R^2, are critical in two different moments:

- during cross-linking: it is necessary to achieve the right structure in order to allow the polymer setting through cross-linking reactions before the pyrolysis step, which is strictly related to the side groups involved (e.g. condensation reactions in the case of

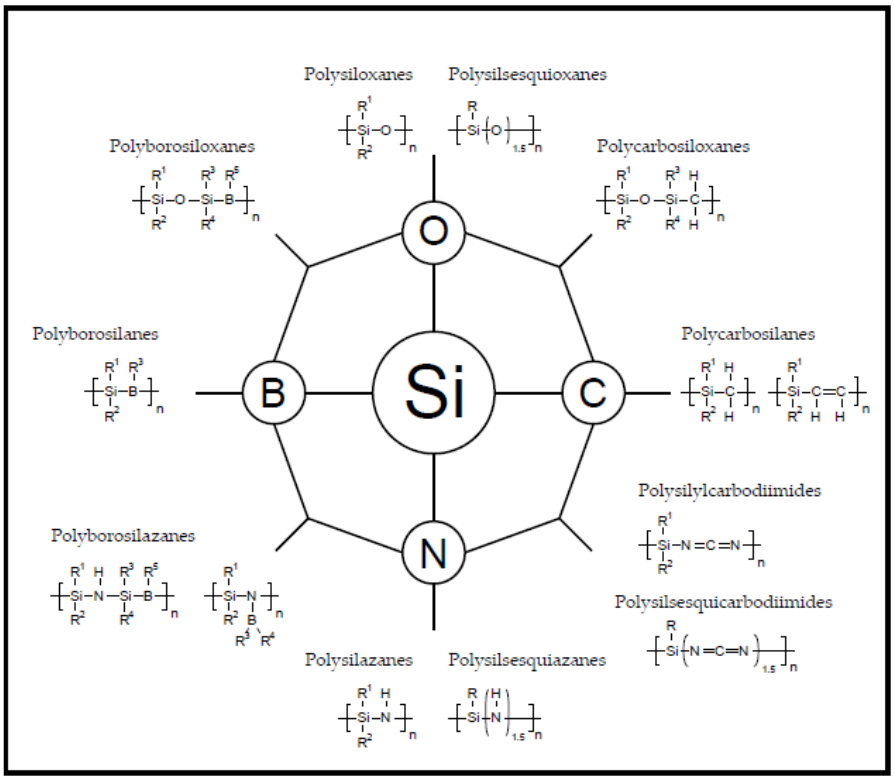

Figure 1.2: Main classes of Si-based pre-ceramic polymers.

–OH functionalities and addition reactions in the case of –vinyl groups);

- during pyrolysis: the nature and quantity of the different side groups will determine the residual C content in the final ceramics (if a non-oxidizing atmosphere is used during pyrolysis);

The second point is fundamental in the specific case, where the goal is to exploit the photothermal effect of this carbon domains, 1.1.

The main classes of Si-based pre-ceramic polymers are four, fig. 1.2: polysiloxanes (*X*=O) and polycarbosilanes (*X*=C), polysilazanes (*X*=N) and polyborosilanes (*X*=B). However, the most studied are polysiloxanes and polysilsesquioxanes (*X*=O) because of their high thermo-chemical stability, non-toxicity and low price. They can be supplied as both solids or liquids. If solids, they are easily soluble in organic compounds or meltable at low temperature (<150°C [2]).

Typically, the most common starting materials for the production of silicon-based pre-ceramic polymers are chlorosilanes [3], i.e. R_xSiCl_{4-x} (x=0-3; where R is an organic side group), thanks to their commercial availability and their low cost.

1.2.2 *Polysiloxanes and poly(organo)silsesquioxanes*

During this thesis work, poly(organo)silsesquioxanes were used as preceramic polymers. They are denoted as silicones and their structure is visible in fig. 1.2. More generally, polysiloxanes are characterized by a Si-O backbone while poly(organo)silsesquioxanes, even if very similar to polysiloxanes, can have different configurations, such as random, ladder, double decker, cage and partial cage structures [2]. The repeating block is -[RSi-$O_{1.5}$]$_n$-, meaning that the Si is sometimes bonded with two oxygen atoms. Thanks to their high branching level, this class of polymer is known as siliconic resins. They are generally solid at room temperature and they have very high ceramic yields upon pyrolysis.

Polysiloxanes and poly(organo)silsesquioxanes give the formation of amorphous $Si_xO_yC_z$ after pyrolysis in inert atmosphere. The proportion between Si, O and C depends both on the nature of the polymer backbone and the side chain group. The presence of both Si-C and Si-O covalent bonds leads to interesting properties like high thermal stability and creep, oxidation and corrosion resistance. They appear black due to the residual "free" C present inside the material.

On the other hand, pyrolysis in oxidizing atmosphere leads to the formation of an amorphous silica matrix due to the removal of carbon by oxidation reaction, fig. 1.3. A totally inert atmosphere, e.g Ar, does not react with the material while N_2 atmosphere could interact increasing the nitrogen content (nitridation reaction) [4]. However, if the temperatures involved during pyrolysis are low (e.g. 1000°C), nitrogen will not react.

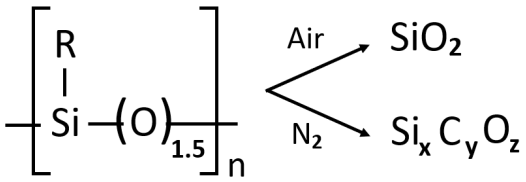

Figure 1.3: Influence of the pyrolysis atmosphere on the final composition.

The general synthesis method for the preparation of polysiloxanes comprises the reaction of chloro(organo)silanes with water, but other synthesis routes have also been proposed, such as the polycondensation reaction of functionalized linear silanes and ring-opening polymerization of cyclic silaethers, leading to hybrid materials combining the properties of polysilanes with those of polysiloxanes [2].

1.2.3 *Manufacturing of engineering ceramic components*

Leaving the polymer synthesis from mono- or oligomer precursor compounds, the manufacturing of engineering ceramic components from polymer precursors typically involves different steps.

SHAPING can consist on extrusion, dip coating, spin coating, chemical vapour deposition (CVD), fiber drawing, casting, injection moulding, pressing, additive manufacturing. All the common and well-known plastic forming technologies can be applied to pre-ceramic polymer: having a polymeric material and system allows the fabrication of compact green bodies, without requiring the addition of binders. Some shaping techniques are visible in fig. 1.4.

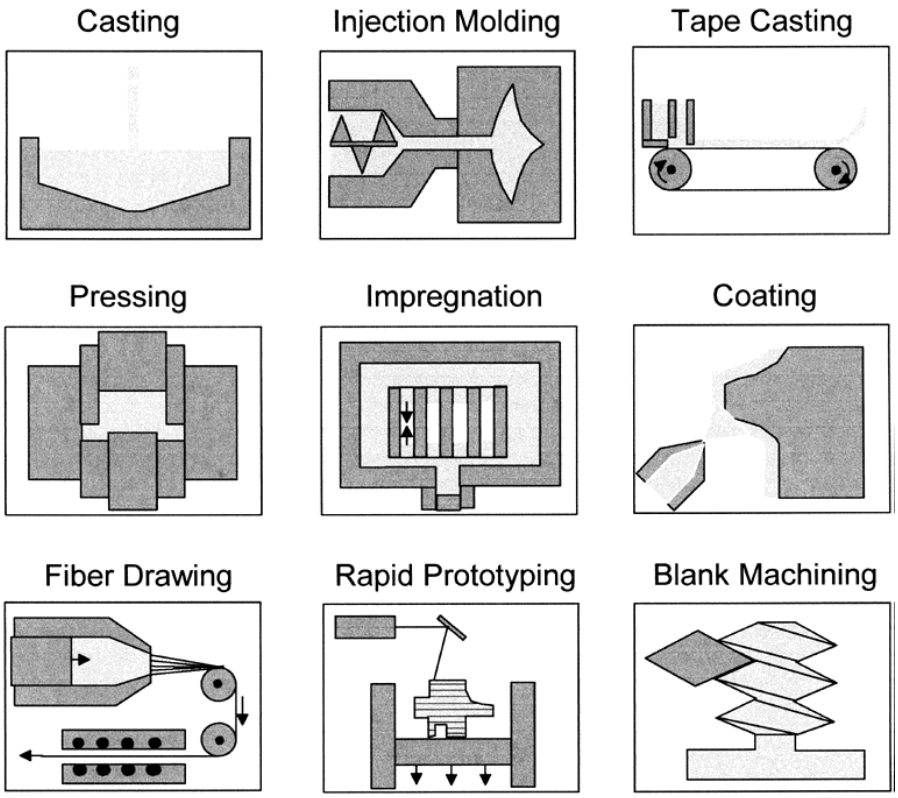

Figure 1.4: Shaping techniques for polymer derived ceramics [5].

CROSS-LINKING is the conversion of the pre-ceramic precursor into a thermoset polymer, capable of maintaining the shape, by curing at 150°C-250°C [5]. These temperatures can be lowered using catalysts or initiators. Furthermore, other strategies can be employed, such as UV-radiation (requiring proper photosensitive groups), γ-rays, electron-beams, selective laser curing.

The cross-linking step represents one of the most important and delicate steps. It permits to achieve the set of the polymeric phase through condensation or addition reactions, thanks to -OH, -H or

-vinyl groups. Depending on the curing atmosphere, a release of gaseous by-products (e.g. water, ethanol) takes place with the possibility of bubbles formation that could remain trapped inside the ceramic part. This is a disadvantage if the goal is to prepare monolithic objects, but it becomes an advantage when preparing porous components by the self-foaming process.

This step is also important in determining the final ceramic yield (i.e. the ratio between the mass of the starting polymer and the mass of the final ceramic) that could be up to more than 90 wt.% (or even up to 105 wt.% when reactive atmosphere is used [6]). A good cross-linking step reduces the formation of oligomers and low molecular weight chains that could volatilize (reducing the final ceramic yield), leading to the formation of highly branched/higher molecular weight polymeric molecules.

Finally, if the pre-ceramic polymer is highly filled, this step could not be necessary because the filler material will give sufficient support to the shape upon heating. The component can then be machined before its ceramization, allowing more precise shape avoiding problems of tool wear and ceramic brittleness.

POLYMER-TO-CERAMIC CONVERSION is the conversion of the polymeric precursor into the final ceramics by pyrolysis in inert or reactive atmosphere: typically between 500°C and 1500°C involving the organic-inorganic transition between 400°C-800°C. During this step, a totally inorganic, non-volatile residue is created through structural rearrangements and radical reactions. On the other hand, non-thermal processes can be applied, such as ion irradiation.

This process is chemically complex and it involves structural rearrangement and radical reactions: Si-H, Si-C, C-H chemical bonds are broken releasing organic compounds (e.g. methyl, phenyl, vinyl groups) and eliminating Si-H, Si-OH or Si-NH_x groups [2]. For polysiloxane, 1.2.2, for example, in the 600–800°C range methane is the main volatile species released, while at higher temperature (600–1100 °C) the release of hydrogen is observed [7]. This gas releases can cause the formation of cracks and porosity as well as the shrinkage of the component.

The microstructural transition, starting from pre-ceramic polymer synthesis to the polymer-to-ceramic conversion is illustrated in fig. 1.5. An increase in density by a factor of 2-3 is generally observed after the pyrolysis. Typically, after the polymer-to-ceramic conversion, the structure is amorphous and constituted by a mixture of covalent bonds (e.g Si-C, Si-O). At higher temperatures, the amorphous network could eventually modify and rearrange bringing to phase separation and crystallization of different phases, depending on the structure of the

starting pre-ceramic polymer.

Therefore, the chemical composition of the final ceramics is determined by two main factors: chemistry of the starting precursor and treatment conditions (temperature, atmosphere, pressure, humidity, etc.).

The structure can remain amorphous up to 1000°C-1800°C [2], depending on the molecular structure and composition of the precursor. Nevertheless, at higher temperature or long dwelling time, the devitrification of the amorphous network could start leading to local crystallization of different phases and separation of a "free" carbon phase subjected to a graphitization process.

Furthermore, the insertion of additional additives or modifiers (filler) can change the properties of the final ceramic.

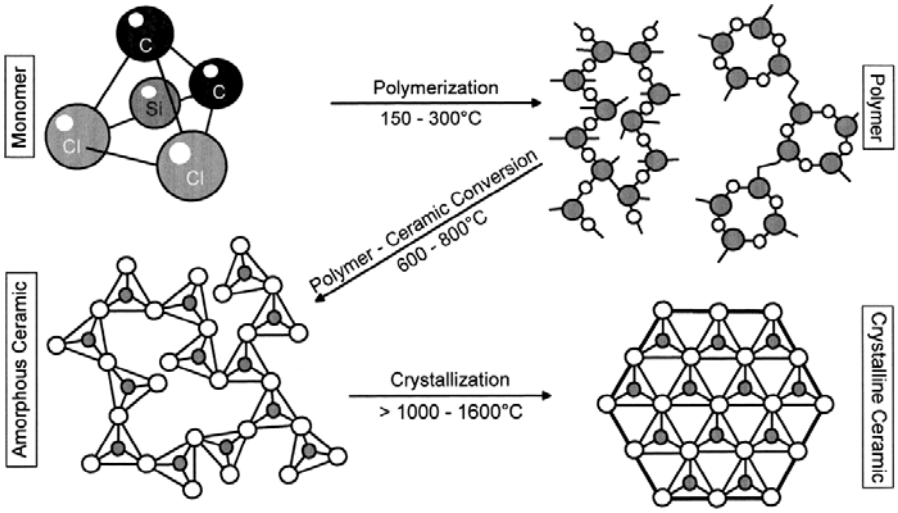

Figure 1.5: Evolution of a pre-ceramic polymer [5].

1.2.4 *Pre-ceramic polymers with fillers*

The main problem of using pre-ceramic polymers is the extraordinarily high volume shrinkage that follows the polymer-ceramic conversion. This is mainly caused by the structural changes in the polymer-derived phase and the impossibility of relaxing by viscous flow or diffusion. The shrinkage can exceed 50% leading to large defects such as cracks or pores that compromise the mechanical integrity of the object and reduce the final density. The conversion of a pre-ceramic component to a dense ceramic is then virtually unachievable, unless its dimension is typically below a few hundred micrometers, as in the case of foams, fibers and coatings.

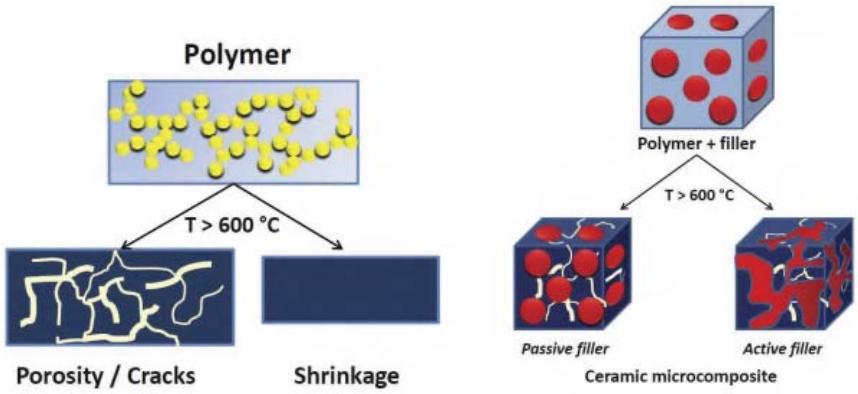

(a) *Filler-free polymer pyrolysis.*

(b) *active filler controlled polymer pyrolysis with near-net-shape conversion.*

Figure 1.6: Microstructural changes during the polymer-ceramic conversion [2].

The introduction of fillers (polymeric, metallic, ceramic) is the main strategy that can be used to avoid or reduce this volume shrinkage. They can be of different shapes (powders, platelets, nanotubes, fibers) and dimensions (nano-size, micro-size or even centimeters).
Furthermore, they do not only reduce shrinkage and defects, but they can also be used to obtain a composite material, to achieve higher densities or to give some mechanical, electrical or magnetic properties. Fillers can be divided into two different categories (fig. 1.6):

- **inert (or passive)**: non-reactive at any stage with the pre-ceramic polymer, its residue or heating atmosphere, i.e. they remain totally inert during the whole manufacturing process. The main function is to reduce the shrinkage of the component upon ceramization and eliminate the presence of macro-defects, i.e. cracks or large pores. Furthermore, even if inert, they can impart interesting features to the component such as better mechanical (i.e. strength, toughness [5]) and thermal (i.e. lower coefficient of thermal expansion) properties, higher wear resistance or even conductivity. On the other hand, the introduction of passive fillers can also reduce the final cost of the product. Examples are SiC, Si_3N_4, Al_2O_3, B_4C, BN powders but also carbon, glass and SiC fibers or carbon nanotubes and graphene sheets;

- **reactive (or active)**: they mainly interact with the gaseous products generated during the polymer-to-ceramic conversion, but also with the heating gas and/or the ceramic residue, generating carbides, nitrides, oxides, silicides. They can expand during the reaction allowing a near-net-shape conversion thanks to the compensation of the polymer shrinkage by appropriate expansion. The resulting material is thus generated by the combination of

four components that must be carefully studied: pre-ceramic polymer, active filler introduced, gaseous by-products deriving from the decomposition of the pre-ceramic polymer and the treatment atmosphere. Examples are metallic and intermetallic fillers.

In addition, oxide fillers can be both inert or reactive, depending on the heating atmosphere, firing temperature and dimensions. For example, when processing in air to obtain oxide ceramics, γ-alumina micrometer-sized remains unreacted upon 1400°C. After mixing with polysiloxane, it starts to transform into mullite at T>1500°C [8]. However, if nanosized γ-alumina powder is used, the reaction occurs at lower temperatures (influence of the dimensions).

Fillers can also constitute the majority of the volume of the final part: in this case, the pre-ceramic polymer acts as a low-loss binder that could increase the density of the final part. Anyway, the introduction of fillers modifies the ceramic component, which becomes a composite material constituted by two or more phases: one derived from the pyrolysis of the pre-ceramic polymer and one or more secondary phases related to the incorporation of fillers.

1.3 BIOMATERIALS

One of the main accepted definition of biomaterials is the one employed by the American National Institute of Health that describes biomaterials as *"any substance or combination of substances, other than drugs, synthetic or natural in origin, which can be used for any period of time, which augments or replaces partially or totally any tissue, organ or function of the body, in order to maintain or improve the quality of life of the individual"* [9]. All materials, therefore, elicit a response from the host tissue and the most important requirement for a biomaterial is its lack of toxicity.

To consider a material also as a biomaterial, it is necessary to satisfy two conditions:

- biocompatibility: material has to establish interactions that are "not unfavorable" with the living system;
- biofunctionality: the implant has to offer reasonable physical and mechanical properties.

In other words, any material that is implanted into the body should be biocompatible i.e. non-cytotoxic (not toxic to cells).

There are three different classes of non-cytotoxic materials [10]:

- **bioinert**: chemically and physically stable after implantation (only minimal interactions). There are not materials that are completely inert, but the only response is the encapsulation of the implant by fibrous tissue (scar tissue). The main limitation is that they require revision surgery after about 25 years [11]. Examples are alumina, zirconia, stainless steel, HDPE;
- **bioresorbable**: materials that dissolve in contact with body fluids and whose dissolution products can be secreted via the kidneys [11]. Examples are poly(glycolic acid), PGA, poly(lactic acid), PLA, calcium phosphates;
- **bioactive**: material that stimulates a biological response from the body such as bonding to living tissue [12]. There are two classes of bioactive materials. Class B materials bond to hard tissue (bone) and stimulate growth along the surface of the bioactive material, i.e. they are osteoconductive. Examples are hydroxyapatite and tricalcium phosphate ceramics. Class A materials are both osteoconductive and osteoproductive, i.e. they stimulate the growth of new bone also on the material away from the bone/implant interface. Examples are bioactive glasses.

The mechanism of bone-bonding to bioactive materials is due to the formation of a hydroxyapatite (HA) layer on the surface after

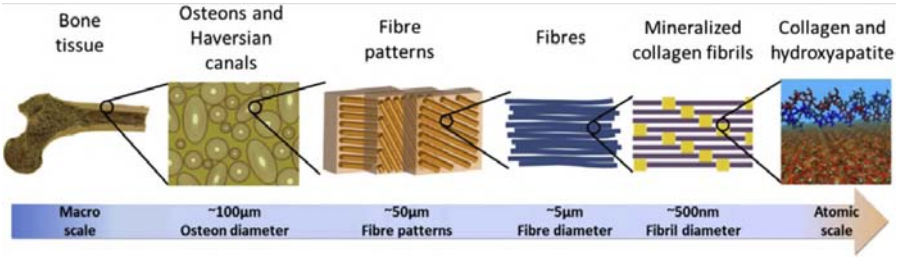

Figure 1.7: The hierarchical structure of bone ranging from micro-scale skeleton to nanoscale collagen and hydroxyapatite [14].

immersion into the body fluid [11]. This layer, very similar to normal and natural apatite, can form a very strong bond with the implant.

1.3.1 *Scaffolds for bone repair*

Life expectancy is increasing as healthcare and technology improve, but not all body parts can maintain their function with the aging process. Bone and cartilage are needed to support the aging body even though the cells that produce them become less active with age, while the heart, kidneys, and liver must operate for much longer than ever before. The most common disease is the loss a bone density caused by a reduction in the number of osteogenic cells (osteoblasts), i.e. osteoporosis, an increasing disease due to the aging of the global population [13].

Nowadays, surgical procedures for the repair of tissue lost as a result of trauma or cancerous tissues involve graft implants that can be taken from a donor site in the same patient, from another human donor or from other living or non-living species. However, there are several usage limitations such as the limited material availability, complicated or numerous surgeries, risk of disease transmission [15]. An approach that demonstrated to be promising is the use of synthetic substitutes, designed to act as a scaffold for the regeneration of tissues. That is the fundamental goal of bone tissue engineering. Bone tissue engineering has also be defined as *"an interdisciplinary field that applies the principles of engineering and life science towards the development of biological substitutes that restore, maintain, or improve tissue function"* [16].

When the defect size is very large, i.e. segmental bone defects, the natural healing process is not able to bridge the gap without a supporting scaffold: in these cases, the role of such porous scaffolds can be really important.

Before designing a scaffold it is important to understand the structure of the bone itself. Bones can be divided in two main types: cortical and trabecular bone. The former is a dense structure with high me-

chanical strength (compact bone) while the latter is a network of struts, called *trabeculae*, that enclose large voids, fig. 1.7. Typically, trabecular bones are present at the ends of long bones (e.g. femur).
Bone is then a natural composite, made of collagen (polymer) and bone mineral (ceramic) [11]. The former provides a framework for the bone and it is made by a triple helix of protein chains with high tensile and flexural strength. On the other hand, mineral bone is a crystalline calcium phosphate i.e. hydroxyapatite, $Ca_{10}(PO_4)_6(OH)_2$, that gives stiffness and compressive strength. For example, the elastic modulus of the femur, 17 GPa (in tension), is intermediate between apatite and collagen [17]. But, its strength is higher than both of them because the inorganic phase, HAp, is made of tiny crystallites embedded in a collagen matrix, fig. 1.7.

The compressive strengths of some different classes of bones are shown in tab. 1.1. The compressive strength of trabecular bone is usually estimated at around 2–12 MPa [18, 19]. Trabecular bones create a porous environment where the porosity can range from 50% to 90% [20] combined with pore sizes at the order of 1 mm in diameter. Typical apparent density values for femoral cortical bone is $1.85 \simeq 0.06$ g/cm^3. On the other hand, cortical bone has a more solid structure with some voids (i.e. haversian canals, with a cross-sectional area of 2500–12000 µm^2) that lead to porosities of 3-12%. The density associated to compact bones is about 1.8-2.0 g/cm^3 [21].

The ideal scaffold, fig. 1.8, is able to mimic the extracellular material, acting as a template in which cells can attach, multiply, migrate [11]. To achieve those goals, a scaffold should satisfy these following main requirements [22]:

- it is made of a *biocompatible* and *bioactive* material, 1.3, i.e. it will not lead to the formation of scar tissue;
- the *resorption rate* is equal to the rate as the tissue is repaired generating products that are non-toxic and easily excreted by the body i.e. via urinary system;
- the surface texture (*microporosity*) is able to promote cell adhesion and adsorption of biological metabolites;
- pores diameter higher than 100 micron [20] (*macroporosity*) for cell penetration, tissue ingrowth, vascularization, and nutrient delivery;
- the *mechanical properties* are adequate to allow a good regeneration of the tissue;

The last two points are very interesting from the design and engineering point of view and one of the main issues is to manufacture

Table 1.1: Mechanical properties of bone [20].

Type of bone	Direction and type of load	Ultimate Strength [MPa]	Elastic Modulus [GPa]
Cortical (midfemoral)	Longitudinal tension	133	17
	Longitudinal compression	193	17
	Longitudinal shear	68	3
	Transverse tension	51	11.5
	Transverse compression	33	11.5
Trabecular (proximal tibia)		5.3	0.445
Trabecular (proximal femoral)	Axial	6.8	0.441

scaffolds with the elastic modulus as close as possible to that of natural bone. In fact, the bone will adapt to the load under which it is placed (Wolff's law). In particular, if the loading acting on a specific point increases, the bone will re-model in order to become stronger and resist to that load, while if the load decreases, the bone will lose density (osteopenia) becoming weaker because of the lack of stimulus to tissue growth. The latter is a typical issue when using a metal implant. Therefore an ideal bone-implant should be such that it exhibits an identical response to loading as real bone and is also biocompatible with existing tissue.

1.3.2 *Bioceramics for bone repair*

Ceramic materials used for biomedical applications are called bioceramics and they follow the classification proposed above (1.1): bioinert, bioactive or bioresorbable, depending on the type of response in the body. Typically, the choice of a bioceramic depends on three factors [11]:

- physical and mechanical properties;
- degradation of the material in the body;

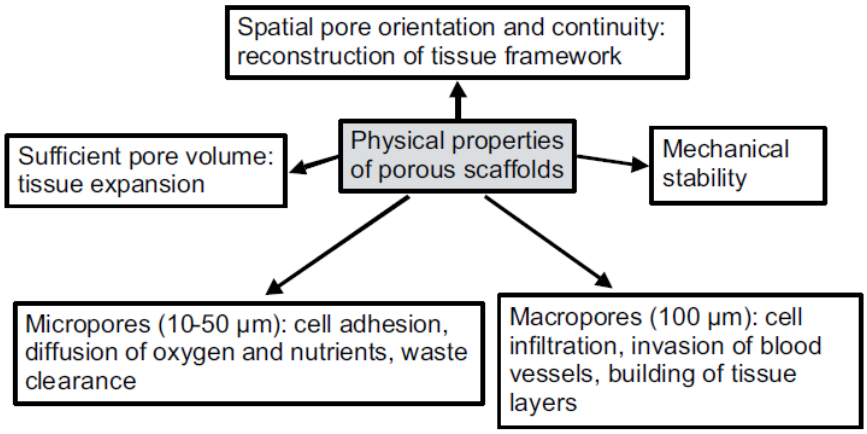

Figure 1.8: Ideal features of a scaffold for bone tissue engineering [11].

- biocompatibility.

The most promising bioceramics are bioactive ceramics for the reasons explained in the previous section, 1.1.

Therefore, the main ceramic biomaterials are briefly described in the following lines [11].

HYDROXYAPATITE [HA, $Ca_{10}(PO_4)_6(OH)_2$] is the main constituent of bones and teeth and that is the main reason for interest. HAp's bioactivity lies in its ability to form an additional layer of calcium phosphate on its surface while the bulk of the material is unchanged [23]. Phase pure HAp resorbs only very slowly, with numerous papers showing negligible resorption even years after implantation [24–26]. Consequently, because of slow in vivo resorption and a high brittleness, which have caused clinicians to be concerned about slow bone formation, hydroxyapatite is not commonly used alone as an osteoconductive bone substitute [27].

TRICALCIUM PHOSPHATE (e.g, β-TCP, $Ca_3(PO_4)_2$, with Ca/P=1.5) is an osteoconductive material, resorbable in the body. Typically, it is used combined with synthetic HA to improve the resorbability of HA. Tricalcium phosphate is less brittle and has a faster resorption rate than hydroxyapatite i.e. 95% of calcium phosphate is resorbed in twenty-six to eighty-six weeks [27]. So, tricalcium phosphate and hydroxyapatite are usually combined to form a biphasic calcium phosphate composite, more easily resorbable than pure HA.

Therefore, it is possible to control the bioactivity by manipulating the HA/β-TCP ratio.

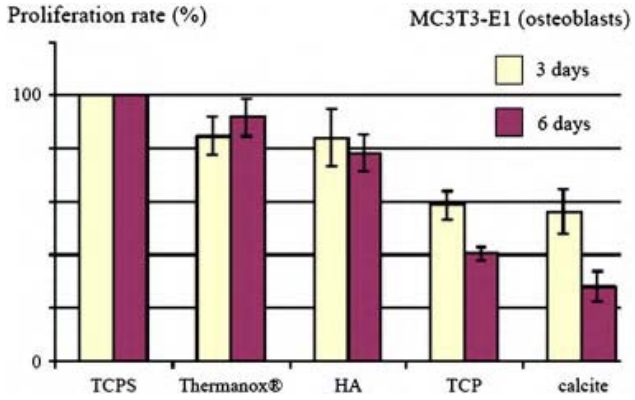

(a) *Cellular proliferation.*

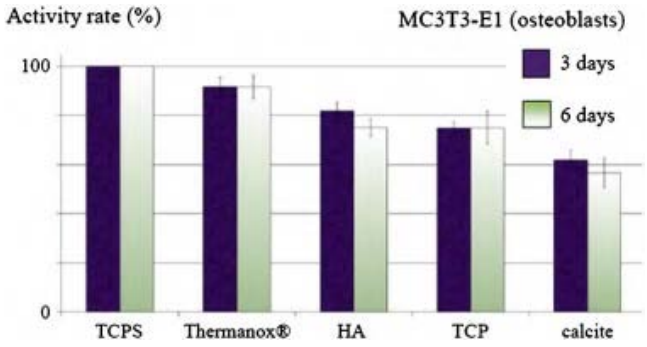

(b) *Cellular activity.*

Figure 1.9: Cellular proliferation and cellular activity (Alamar-Blue test) on controls and macro-porous ceramics during 3 and 6 days [30].

BIOACTIVE GLASS (e.g. 45S5 Bioglass®) exhibits unique properties for this application showing osteoinductive behaviour, ability to bond to soft tissue as well as to hard tissue and to form a carbonated hydroxyapatite layer (HCA) when exposed to biological fluid [28]. This layer is responsible for the strong bonding between bioactive glasses and human bone. Therefore, the glass is resorbable and the dissolution stimulates seven families of genes that regulate osteogenesis and the production of growth factors. It was observed that ionic dissolution products from Bioglass® (e.g. Si, Ca, P) and from other silicate-based glasses stimulate expression of several osteoblastic cell genes [29]. This is the reason why some compositions of bioactive glasses, that are especially effective in promoting bone growth, are class A bioactive materials.

CALCIUM CARBONATE [$CaCO_3$] is a well-established material for implantation purposes, due to its high biocompatibility and bioactivity. For this reason, marine corals (99% $CaCO_3$, aragonite polymorph-1% organic) have been used since the 80s and 90s [31, 32] and Ohgushi *et al.* demonstrated that bone formation in calcium carbonate derived from marine corals is comparable to the bioactive hydroxyapatite

(HAp) [33]. Nowadays, implants of natural origin like corals are no longer accepted in orthopedics, due to serious drawbacks, such as supply difficulties, biological variability, risks of viral or bacterial contamination [30]. Synthetic CaCO3-based porous materials are therefore highly attractive, although conditioned by some processing problems. For example, the thermal decomposition of $CaCO_3$ at a relatively low temperature represents a strong limitation to the sintering.

Monchau *et al.* [30] compared the biological properties of synthetic $CaCO_3$ with those of HAp and β-tricalcium phosphate (β-TCP) demonstrating that synthetic $CaCO_3$ could be an interesting alternative not only to coralline aragonite but also to calcium phosphate ceramics, particularly in bone sites with the large bone remodelling. The study demonstrate that pure synthetic calcite is non-cytotoxic. Furthermore, calcite osteoblastic activity (vitality and proliferation) is comparable to that of HA and β-TCP, fig. 1.9. A similar result was obtained by Lemos *et al.* [34] who revealed that porous $CaCO_3$ leads to the formation of a di-calcium phosphate di-hydrate ($CaHPO_4 \cdot 2H_2O$), known as brusite. Besides brusite, they found other acicular calcium phosphate phases in the samples soaked in the SBF (simulated body fluid) that seems to appear mainly from the pores.

1.3.2.1 *The "composite approach"*

The "composite approach" consists of using pre-ceramic polymers, e.g. silicone resins, as matrices for $CaCO_3$ following the work already done in previous experiments carried out by the CERAMGLASS [35] group at the University of Padua [36–43]. The particular matrix enabled the transformation into silica-calcite composites by thermo-oxidative transformation of the polymer.
Therefore, it is possible to obtain two different composite structures depending on the heat treatment.

WOLLASTONITE-DIOPSIDE-CARBON COMPOSITE [36, 41, 42] is a bioceramic in the CaO-MgO-SiO_2 system, well-known for bone tissue engineering application [44]. Single-phase silicates, such as wollastonite ($CaSiO_3$) [45] and diopside ($CaMgSi_2O_6$) [46] can exhibit excellent bioactivity and cytocompatibility. The manufacturing process starts from a silicone-based mixture incorporating micro-sized fillers. In particular, Silres MK®, i.e. methyl polysilsesquioxane resin, behaves as SiO_2 precursor, while $Mg(OH)_2$ and $CaCO_3$, i.e. micro-sized filler, are the MgO and CaO precursors respectively. The mixture is firstly homogenized by supercritical CO_2-assisted extrusion and foamed at 350°C in air. Then it is pyrolyzed at 1100°C in nitrogen atmosphere. The process yield to a final ceramic with two silicate phases: wollastonite, $CaSiO_3$, and diopside, $CaMgSi_2O_6$, embedded in an amorphous matrix. The microstructure of the final ceramic can not

be attributed to the formation of a homogeneous silicon carbide matrix (SiOC), as shown previously in fig. 1.3, but the amorphous material that surrounds the wollastonite and diopside phases consists of a nano-composite, with C domains immersed in a silicate glass phase. It can be concluded that the presence of reactive fillers conditions the pyrolysis of the silicone resin leading to carbon in the form of a separate nano-sized phase, enhancing silica formation instead of SiOC [42].

SILICA-CARBON-CALCITE COMPOSITE was successfully 3D-printed by Elsayed *et al.* [40, 43] from a paste comprising a silicone polymer, i.e. Silres MK®, and calcite powders. The mixture was fired at 600°C in N_2 after preliminary cross-linking step at 350°C, determining the transformation of the polymer matrix into a silica-carbon nanocomposite embedding unreacted calcite particles. The firing temperature is the main difference from the wollastonite-diopside-carbon composite. The aim is to avoid the decomposition of $CaCO_3$, which occurs at about 700-800°C, to exploit its biocompatibility and bioactivity. The particular atmosphere led to composites with a silica-rich matrix including calcite and pyrolytic carbon without the formation of a silicon carbide matrix (SiOC).

The use of pre-ceramic polymers, e.g. silicones, enables easy manufacturing of highly porous scaffolds like three-dimensional reticulated structures, 1.5.

1.3.3 *Carbon fiber composites*

Carbon fiber composites had been investigated as biomaterials since the 1970s [47], mostly because they have multiple potential advantages in developing high-strength biomaterials composites with a density close to the bone, enabling better stress transfer and electrical properties that enhance tissue formation [48]. Petersen [48] compared a rat implant made of bisphenol-epoxy/carbon-fiber-reinforced composite with a similar titanium 6-4 alloy screw. Carbon fibers turn out to have a semi-antioxidant property to remove damaging electron free radicals from the surface of the implant acting as electrically conducting bio-circuits [48]. Carbon fibers can be combined with different matrix materials as polymers (PEEK, UHMWPE, epoxy resin, polyamide, polysulfone, etc.), ceramics (carbon, hydroxyapatite, etc) and also metals.

Carbon fibers have two different features when they interact with a biological system [47]: bioinertness and bioactivity, see 1.3. On one hand, carbon fibers do not corrode *in vivo* (bioinertness) and, on the other hand, bone tissue can easily grow on areas surrounding car-

bon fibers and osteoblasts improve their cell adhesion (bioactivity). Carbon fibers have good biocompatibility and long *in vivo* stability. In particular, carbon fibers of nano-sized diameter (nanofibers) have captured new interest in the last decades [49][50]. Elias *et al.* [49] investigated long-term functions of osteoblasts on unmodified carbon nanofibers, finding out that osteoblast proliferation increased with decreasing carbon fiber diameters (from 60 to 200 nm) and showing the first evidence of enhanced osteoblast proliferation, alkaline phosphatase synthesis, and concentration of extracellular matrix calcium on compacts of carbon with individual nanometer fiber diameters.

1.3.4 *Geometry considerations*

Geometry is an important parameter when design scaffolds for bone tissue engineering, able to affect and guide tissue growth. The fundamental feature is the presence of ample interconnected pores in order to allow the vascularization of the implant in such a way to guarantee tissue ingrowth, cell nutrition and oxygenation [51]. The minimum pore size is 100µm (1.3.1), but subsequent studies of Karageorgiou and Kaplan [20] have shown better osteogenesis for implants with pores >300µm. However, besides this fundamental characteristic that must always be satisfied, it is still possible to guide and stimulate the tissue growth by acting on the scaffold geometry. For example, surface (nano) topography could determine the stem cell fate, facilitate stem cell differentiation towards the osteogenic lineage, and ultimately result in larger volumes of new bone formation [51–54].

Recent evidence, for example, shows that pore shape and surface curvatures could strongly influence the bone tissue regeneration process. Rumpler *et al.* [55] observed that the tissue ingrowth rate is proportional to the surface curvature showing a higher tissue growth rate where the curvature is higher, i.e. in the corners, fig. 1.10. Moreover, the type of curvature turns out to be crucial: the tissue ingrowth process shows a preference for concave surfaces instead of flat or convex. Furthermore, the variation of the same surface curvature can modify the cell attachment rate, migration speed, morphology. This is especially true during the first few weeks after implantation where blood vessels are present mostly in the concavities [51], i.e. concave curvatures favor angiogenesis.

Nevertheless, the crucial role of the material must not be forgotten. Zadpoor [51] dived the bone tissue regeneration into two stages:

1. initial stage (up to a few weeks): the first stage is dominated by cell-material interactions with cell adherence and differentiation being strongly dependent on the material;

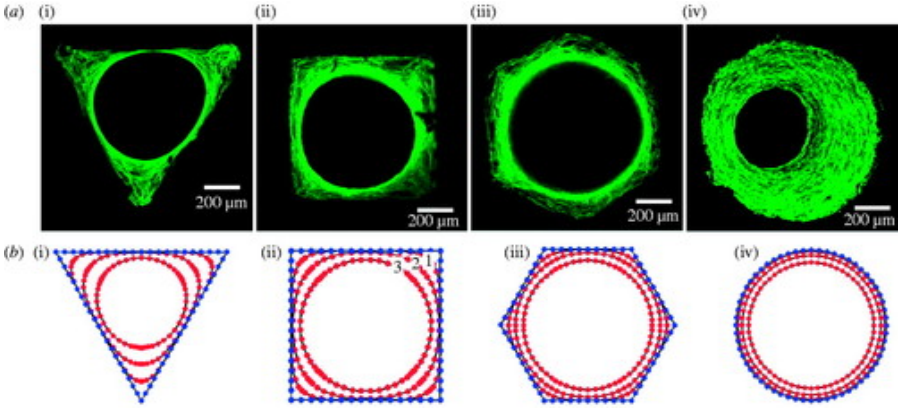

Figure 1.10: (a) New tissue formed in three-dimensional matrix channels (confocal laser scanning microscopy): tissue formation is shown (i–iii) after 21 days and (iv) after 30 days of cell culture in the channels of a (i) triangular, (ii) square, (iii) hexagonal and (iv) round shape introduced into a HA plate *in vitro*. (b) Numerical simulation of tissue formation within channels of various shapes: (i) triangular, (ii) square, (iii) hexagonal and (iv) round (blue line is time zero, while each red line represent ongoing times) [55].

2. second stage: the cells begin to grow within their own matrix and the process shows a dependence from pore size, geometry, surface curvature and substrate stiffness rather than scaffold material properties.

Therefore, in order to evaluate the influence of geometry, long studies and tests are required: a short *in vitro* study can conclude that the geometry does not influence the tissue regeneration, without considering that its role becomes important in the later stages.

Furthermore, it must be said that it is not easy to study the influence of only one parameter, for example, pore size and shape: their modification can cause other changes such pore interconnectivity and scaffold mechanical properties, e.g. stiffness, with a consequent change in load distribution which could distort the results. One approach to overcome this distortion could be to change material together with pore size, in order to have the same stiffness. However, changing material will introduce other distortion, e.g. different surface topographies and surface chemistry. Then, also pore size, porosity and curvature are difficult to separate: the average curvature of a closed curve is connected to its perimeter, P (average curvature $\geq 2\pi/P$). Considering that the curvature is related to the perimeter and the perimeter is strictly connected to the pore size, curvature and pore size are not independent [51].

Anyway, what is clear is that geometrical features with a higher curvature may result in higher levels of stress concentration, and, thus,

higher levels of tissue regeneration stimulus [51]. Furthermore, even if there is currently only limited evidence available as to what kind of curvature is best for tissue, the tissue growth is dependent on the curvature sign (convex or concave) because of the presence of contractile tensile stresses produced by cells near the tissue surface. This can be the reason for the reduced tissue growth on convex surfaces.

1.4 PHOTOTHERMAL EFFECT

Photothermal effect is a physical phenomenon associated with the interaction of electromagnetic radiation with matter that produces a photoexitation of the material, resulting in the production of thermal energy (heat) [56]. The electromagnetic radiation could be for example radiofrequency, microwaves, near infrared irradiation (NIR), or visible light. This effect has attracted great interest, mainly for its application in the field of photothermal therapy (PTT), see 1.4.1.

1.4.1 *Photothermal effect and photothermal therapy*

The photothermal effect can be described as the phenomenon in which a material produce thermal energy from electromagnetic radiation. Once the electromagnetic radiation is absorbed by a material, free electrons will vibrate at a very high frequency, i.e. reach higher energy levels. This vibrational energy is partially converted into the electromagnetic waves and radiate outwards. The rest is transformed into kinetic energy of electrons and converted into heat energy through the relaxation process between electrons and lattices [57].

The procedure of heating a region in the body affected by cancer or other diseases and killing the malignant cells is called hyperthermia [58], which is typically achieved when the temperature is raised to between 40°C and 44°C. This method has gained a lot of interest because of its low toxicity, non-invasiveness, simplicity, and potential to treat tumors in areas difficult to reach with normal surgery. The fundamental consideration at the basis of this therapy is that tumors are more susceptible to heat than healthy cells. There are different ways to induce cancer cells death through heating like degradation of the cell wall membrane, protein denaturation, and the production of reactive oxygen species, leading to necrosis and apoptosis [58]. Hyperthermia can also be combined with chemotherapy and radiotherapy for enhanced treatment of many different types of cancer [59]. It is possible to use different energy sources to achieve hyperthermia, such as magnetic fields, lasers, radiofrequency (RF) pulses, and ultrasound.

In particular, it is possible to talk about photothermal therapy (PTT) when using photothermal agents to generate heat under near-infrared light irradiation (NIR) to ablate tumor cells. This technique is different from chemotherapy and radiotherapy because it is local, with minimal invasiveness and high efficiency. Cells death could follow three mechanisms, fig.1.11 (a): cell membrane destruction, tumoral DNA denaturation, and angiogenesis blocking. NIR lasers, especially those that operate at around 800 nm, seem to be one of the most popular energy sources for photohyperthermia due to NIR light being trans-

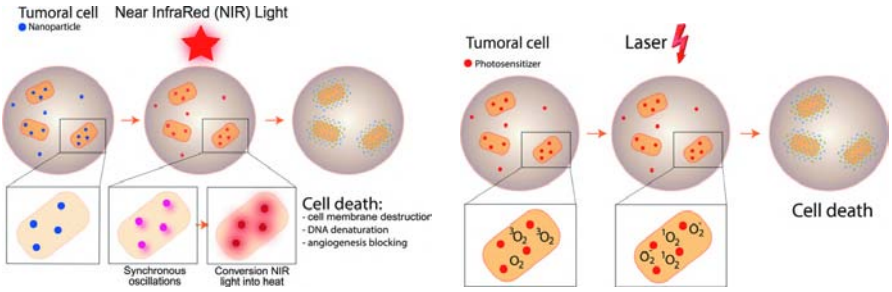

(a) *Photothermal theraphy (PTT)* (b) *Photodynamic therapy (PDT)*

Figure 1.11: Comparison between PTT and PDT [61].

parent through tissues and water. However, although NIR radiation works well in superficial (e.g. subcutaneous) tumors, it may be not suitable for deep-seated tumors. In those cases, microwaves and electromagnetic field could be a solution [58]. Therefore, a crucial point is the choice of laser energy: on one hand, high energy could not be safe for medical applications and, on the other hand, low energy would require very long and time-consuming therapy.

PTT is similar to photodynamic therapy (PDT), a technique that involves two individually non-toxic components that are combined to induce cellular and tissue effects in an oxygen-dependent manner [60]: a photosensitizer, a photosensitive molecule, and light of a specific wavelength able to activate the photosensitizer that can transfer energy to the very close tissue, generating reactive oxygen species (ROS). This ROS mediates cellular toxicity reacting with oxygen and the photosensitizer giving cytotoxic single oxygen. Cell death, fig. 1.11 (b), could follow two different mechanism: direct (necrosis and apoptosis) and indirect (microvascular damage, antitumor immune responses). The most frequent side effect consists of a capillary leak syndrome and skin diseases and long-lasting cutaneous photosensitivity.

Owing to their unique properties of high optical absorption capacity in the near-infrared region and photothermal conversion, graphene-based (e.g. carbon nanotubes [62]) or gold-based (nanorods, nanoshells [58]) nanomaterials are ideal candidates for photothermal therapy. Gold nanospheres, although they are the simplest gold nanostructures to synthesize, possess a peak optical absorption in the visible region and not in the NIR i.e. the penetration depth is too low for reaching tumors.

Furthermore, Herath *et al.* studied the photothermal effect of carbon fibers by carbon fibers under an 808 nm near-infrared radiation of five different power densities, i.e. 0.01, 0.5, 1.0, 1.5, 2.0 W/cm^2 [57]. Interestingly, when testing a 0/90 woven carbon fiber reinforced shape memory epoxy composite (SMPC) made out of prepreg material, the

SMPC has been heated over its glass transition temperature, thanks to its exposition under an 808 nm wavelength near-infrared light with a power density of 1.0 W/cm².

Furthermore, carbon fibers have shown a significant and quick photothermal effect, i.e. they were heated up to 183°C at the power density of 2.0 W/cm². For the carbon fiber, there was no linear relationship between the highest temperature and power density: incrementing the power density, the gaps between the highest temperatures are getting close probably due to the reflectance of NIR radiation by the exposed surface.

1.4.2 *Bifunctional scaffolds with a photothermal activity*

As already explained, scaffolds do not simply act as temporary support for cells at the initial stage, but also contribute the angiogenesis ability, cell migration, and nutrient transport and metabolism abilities, see 1.3.2. However, it is difficult to use these materials for bone defects caused by bone tumor, because the proliferation of residual tumor cells inevitably leads to tumor recurrence. The treatment of such a bone disease typically requires the removal of bone tumor and regeneration of tumor-initiated bone defects simultaneously. Keeping this in mind, it would be useful if the scaffold had also the ability to kill residual tumor cells, allowing the possibility of carrying out a photothermal therapy, 1.4.1.

Ma *et al.* [63] demonstrated the possibility of producing such an implant by manufacturing a bifunctional graphene oxide (GO)-modified β-tricalcium phosphate (GO-TCP) composite scaffold combining a high photothermal effect through 3D-printing and surface modification strategies (β-TCP scaffolds were soaked in GO water solution with different concentrations). This scaffold presents an excellent photothermal activity when irradiated with an 808 nm near-infrared laser thanks to the graphene oxide, even at relatively low power densities (e.g. 0.36 W/cm²). Specimens were heated up in the range 40-90°C by changing the amount of GO, surface modification time and power density of the laser. The effectiveness of the material was tested both *in vitro* (for osteosarcoma cells, MG-63) and *in vivo* (mice).

Furthermore, Fu *et al.* [64] employed polymer-derived ceramics (PDCs) strategy combined with 3D printing technique in order to manufacture free carbon-embedding larnite (larnite/C) scaffolds exhibiting photothermal effect. The manufacturing process combine a silicone resin, Silres MK®, loaded with $CaCO_3$, following the insights from CERAMGLASS group [35] at the University of Padua, 1.3.2.1. After printing, the lattices were treated at different temperatures (1000°C, 1100°C, 1200°C) in argon atmosphere. The photothermal effect was

evaluated by irradiating the samples with an 808 nm near-infrared laser using different power densities (0.5 W/cm², 0.75 W/cm², 1 W/cm²). The scaffolds were then tested both *in vitro* (for osteosarcoma cells, MNNG/HOS) and *in vivo* (mice). This work clearly demonstrate the possibility of employing the free carbon derived from the pre-ceramic polymer as photothermal agent to kill bone tumor cells *in vitro* and *in vivo*.

In addition, a very recent work from Zhu *et al.* [65], proposed the manufacturing of forsterite (Mg_2SiO_4) scaffolds sintered in an argon atmosphere combining 3D printing and polymer-derived ceramics (PDCs) strategy. The samples exhibited excellent photothermal effect and could inhibit the growth of Staphylococcus aureus (S. aureus) and Escherichia coli (E. coli) *in vitro*, i.e. photothermal effect can be exploited not only for killing tumor cells but also for fighting bacterial infections of the implant i.e. antibacterial activity.

From here, the idea of exploiting photothermal properties of carbon in two of its forms: pyrolytic carbon, deriving by pre-ceramic polymer decomposition, and carbon fibers, inserted as a filler.

1.5 ADDITIVE MANUFACTURING

Additive manufacturing (AM), also designated as solid free-form fabrication (SFF), Rapid Prototyping (RP), or 3D printing, describes a class of technologies in which a part is directly generated from a virtual model by adding material to form the part [66]. It is defined by ASTM F2792-12a (Standard Terminology for Additive Manufacturing Technologies) as the *"process of joining materials to make objects from 3D model data, usually layer upon layer, as opposed to subtractive manufacturing methodologies, such as traditional machining"* [67]. This technology is well known for its great versatility that derives from the possibility of generating parts with arbitrary geometries without the need of adapting the typical manufacturing process itself. Therefore, starting from a virtual 3D model and from the material in the form of powders or pastes (ink), the desired sample is obtained by direct forming, i.e. adding material for overlapping and subsequent layers, following the geometry proposed by the 3D model. Consequently, it is the opposite of conventional subtractive techniques.

Additive manufacturing allows the design and production of complex structures with engineered porosity, with precise control of the dimension not obtainable using other manufacturing methods. Therefore, it opens new fields of research and application that not compete with other traditional manufacturing processes. This is even more true for ceramic materials that are not easily mechanically workable because of their brittle behaviour. In particular, any modern biomaterial for bone tissue applications must obey strict morphological requirements and three-dimensional network structures (1.3.1) with interconnected macro-pores which are needed for cell ingrowth and vascularization to be effective.

Additive manufacturing techniques can be divided into two main categories [66]:

- **direct**: the material is directly deposed in the position that gives the desired final shape. Examples are direct ink writing (DIW)/robocasting, fused deposition modeling (FDM), direct inkjet printing (DIP);
- **indirect**: after the deposition of a layer of material, the cross-section (*slice*) of the part is inscribed in the layer. The process is then repeated until the final shape is reached. Therefore, excess material surrounding the part is removed to release the final object. The inscription step can be carried out in different ways, determining different types of indirect techniques. Examples are powder-based 3D printing (P-3DP), powder-based selective laser sintering (P-SLS), stereolithography (SL), slurry-based 3D

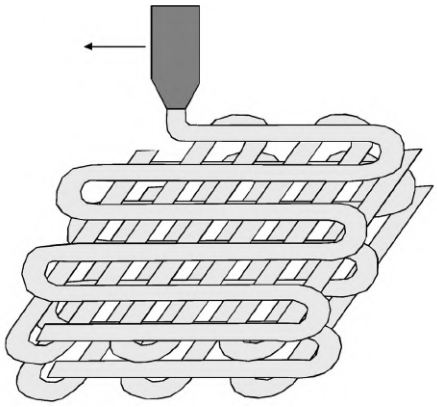

Figure 1.12: Scheme of the direct ink writing process [69].

printing (S-3DP), slurry-based selective laser sintering (S-SLS), laminated object manufacturing (LOM).

The technology used during this thesis is direct ink writing (DIW) or robocasting, thus, the following section aims to explain briefly the principles behind this technique. For further information on the other techniques, both direct and indirect, see the two excellent reviews by Zocca *et al.*[66] and Travitzky *et al.* [68].

1.5.1 *Direct ink writing and robocasting*

Direct deposition of ceramic slurries is the most used AM technology used for the generation of porous structures. It consists on the extrusion through a nozzle of a viscous ceramic paste in the form of a filament [66]. The nozzle is moved by following instructions about position and velocity, usually contained in a *g-code* file (or similar). When the first layer is completed, the nozzle is moved up for the second layer or, vice versa, the substrate is moved down. This deposition method allows achieving the desired tridimensional geometry, both monolithic or porous 1.12.

The control on the rheological properties of the filament is essential to prevent the deformation of the part after extrusion and the collapse of the structure. Typically, the so-called *"ink"* is a ceramic suspension with high solid loading that exhibits a shear-thinning behaviour (or pseudoplastic), a necessary condition for printing and shape retention. The ink behaves like a viscous gel when loaded in the printing head but the gel-like structure is broken during extrusion due to the elevated shear stresses, determining a viscosity decrease of several orders of magnitude. As soon as the paste comes out fo the nozzle, the viscosity increase rebuilding the previous gel structure [66]. It is therefore immediately clear that the control of rheology is one of the

most critical issues of the process.

Therefore, the shape retainment right after printing is mainly controlled by two contributes:

- rheology: a shear-thinning behaviour of the paste is often needed;
- drying: the just extruded filament will start to dry as soon as it comes in contact with the external environment, helping shape retainment. This effect is strictly connected to the volatility of the used solvent, being evident for alcohol and almost negligible for water-based slurries. Furthermore, the thickness of the extruded filament and the environment (temperature, humidity) can affect the drying behaviour. On the other hand, premature drying sometimes does not allow a good joint between two successive layers and it is possible to uncouple the printing and the drying process by changing the printing environment (e.g. using oil [43]).

1.5.2 *Polymer derived ceramics for additive manufacturing*

The pre-ceramic polymer approach to obtain polymer-derived ceramics (PDCs) is a good and viable alternative to the powder processing route, not only in terms of conventional manufacturing technologies but also in the context of additive manufacturing. The strong point of polymer-derived ceramics is connected to their relatively simple processing, i.e. it is possible to start from polymeric precursors, which enables the components to be fabricated using technologies suited for polymers [66]. On the other hand, the most critical issue is the release of gaseous species during pyrolysis and associated with shrinkage 1.2.3. The introduction of fillers, 1.2.4, can help to solve this problem.

Therefore, considering the easy formability of organosilicon polymers, 3D printing techniques, and in particular direct ink writing or robocasting, provide a great choice for fabricating silicon-based ceramics with complex structure or porosity.

2

EXPERIMENTAL PROCEDURE AND CHARACTERIZATION METHODS

This chapter means to present the experimental part of this thesis. Firstly, materials and equipments are briefly described. Then, the experimental process, including ceramic scaffold manufacturing and the following thermal treatment are explained. Finally, characterization methods of the 3D printed scaffolds are shown.

2.1 MATERIALS

A commercial polymeric precursor (i.e. pre-ceramic polymer) was used in combination with calcite and carbon fibers for pre-ceramic inks preparation. In some cases, that is while printing with larger nozzle, fumed silica was added to adjust the rheology and obtain a pseudoplastic printable ink, 1.5.

The following pages will present the materials used during the preparation of the pre-ceramic ink.

2.1.1 *Polymeric precursors*

Two polymeric precursors were used for the preparation of the pre-ceramic ink, both of them are available in the form of fine white powder soluble in isopropyl alcohol (or isopropanol, IPA), used as a solvent.

SILRES MK® (Wacker-Chemie GmbH, München, Germany) is a solid methyl silicone resin, belonging to the polysilsequioxane, sec. 1.2, i.e. with general chemical formula -[RSi-$O_{1.5}$]$_n$- [2]. This resin features a silica yield of 84%wt after thermal decomposition in both air and nitrogen [39]. Silres MK® has a melting point in the 35-55°C range. It is possible to achieve the cross-linking of the silicone performing a heat treatment at 350°C. Very little smoke is evolved during this thermal degradation and soot-like decomposition products are not formed. Thermal and physical properties of the powder are resumed in table 2.1.

Wolff *et al.* [70] assigned to Silres MK® the structure visible in fig. 2.1, taking into account that the amorphous material is highly branched since the resin consists of trifunctional building units where hydroxyl and ethoxy side groups can provide a further condensation of this material.

Table 2.1: Technical data of Silres MK® (from datasheet).

Typical general characteristic	Value
Supply form	white powder
Melting range	35-55°C
Bulk density	500 kg/m^3
Thermal decomposition	min. 350°C

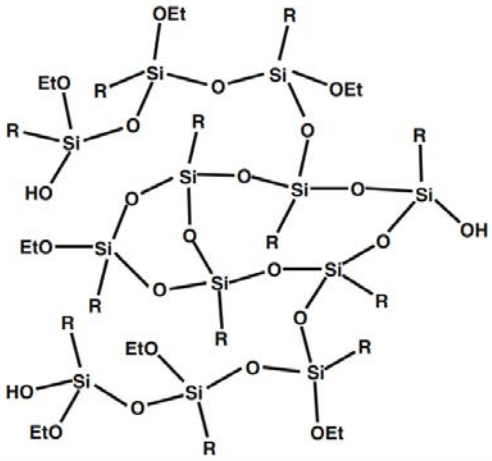

Figure 2.1: Silres MK® structure [70].

SILRES H44® (Wacker-Chemie GmbH, München, Germany) is a solid methyl-phenyl polysiloxane belonging to the polysilsequioxane, 1.2. It shows a silica yield of approximately 84%wt after pyrolysis in oxidative atmosphere, while it features a ceramic yield of about 70%wt in inert atmosphere (e.g. nitrogen).

Table 2.2: Technical data of Silres H44® (from datasheet).

Typical general characteristic	Value
Supply form	white powder
Melting range	45-60°C
Bulk density	450 kg/m^3
Thermal decomposition	min. 350°C

Takahashi *et al.* [71], investigated the rheological properties of both Silres MK® and Silres H44® to understand the relationship between structure and melt behaviour. To achieve this, Takahashi *et al.* [71] characterized the two silicone resins from a molecular and thermal point of view, obtaining the data summarized in the table 2.3.

Table 2.3: Molecular and thermal properties of Silres MK® and Silres H44® [71].

Silicone resin	M_w GPC [g/mol]	M_w / M_n GPC	T_g DSC [°C]	[a]weight loss TGA [%]	[b]weight [%]
MK	9400	3.6	41.9	0.7	a few
H44	2100	1.8	43.0	0.1	3

[a]under air (100°C, 2h) [b]of relative groups where by-products are water, ethanol during cross-linking, according to Wacker-Chemie GmbH (1995)

2.1.2 *Inorganic parts and fillers*

CALCITE (Industrie Bitossi, Italy) represents the biocompatible, bioactive (1.3.2) material as well as the main phase of the ink, 2.3.2. It will also act as a filler helping the shape retainment after printing and reducing shrinkage after pyrolysis. During this work, micro-size calcite, with particles dimension lower than 10 µm, was used allowing a very fine dispersion of the powder within the ink.

UNCOATED CARBON FIBERS MF100 (Ferrari Carbon Srl, Milano, Italy) represent the reinforcement component of the final product (tensile strength = 3.5 GPa, Young modulus = 230 GPa), giving higher stiffness, toughness and resistance to both compressive and flexural loads. They will also help the shape retainment after printing as well as shrinkage reduction after pyrolysis. These fibers feature a diameter of about 7.5 µm and a length of about 100 µm. The XRD pattern of the fibers is shown in fig. 2.2.

FUMED SILICA (Aerosil R106, Evonik Germany) is nano-sized silica, used to modify the rheological properties of the ink. It is typically produced by hydrothermal hydrolysis of chlorosilanes in an oxygen-hydrogen flame. Fumed silica is widely used in industry as an efficient thickening agent providing shear thinning and thixotropy to liquid media. Various parameters control the rheological performance of fumed silica [72]:

- smoothness of the primary particle surfaces which provides high contact area for various types of interactions (H-bonding, Van-der-Waals);
- the space-filling structures of the aggregates that leads to a fluffy structure of agglomerates due to the high fractal dimension of D_m<2.7;

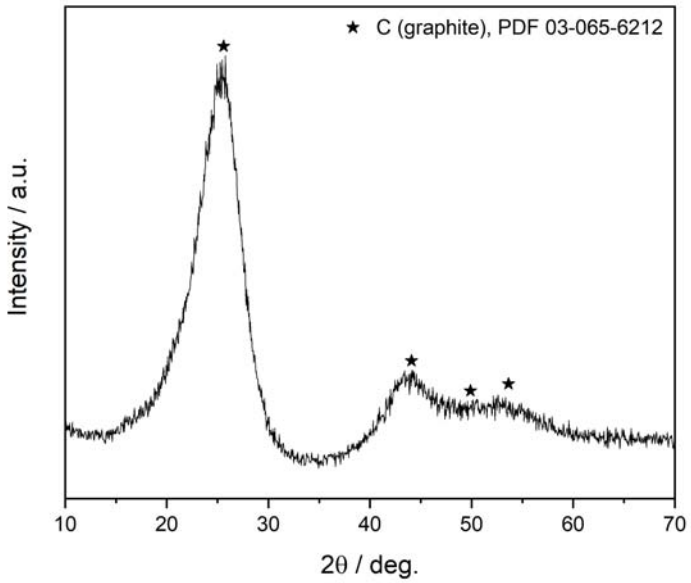

Figure 2.2: XRD pattern of MF100 uncoated carbon fibers (Ferrari Carbon Srl, Milano, Italy).

- the high physico-chemical interaction potential of the fumed silica surface is based on its reactive surface silanol groups (Si-O-H) and to its polar Si-O bonds containing bulk.

Particle interactions are the driving force for agglomeration and network formation. It is sufficient a small amount of fumed silica (<5%wt [72]) to modify the rheology of a fluid, resulting in a more pseudoplastic behaviour and introducing a yield point (or very high viscosity) at zero shear stress.

Figure 2.3 shows how fumed silica can affect the behaviour of a liquid media. When the shear rate (or shear stress) is equal to zero, fumed silica creates a percolating network due to particle interactions, raising the viscosity of the fluid. Then, increasing the shear rate (or shear stress), the percolating network is destroyed inducing a decrease in viscosity, leading to a pseudoplastic behaviour i.e. the viscosity decreases with the increasing of shear forces. The network is then rebuilt when the applied shear rate (or shear stress) is removed.

It is therefore immediate to understand how this can help the ink printability. Applying shear stresses through pressure (or by using a screw system), the viscosity will be low, allowing the easy flow of the paste, right part of the graph in fig. 2.3. Then, as soon as the paste comes out from the nozzle, the viscosity will rapidly increase and the extruded filament can maintain its shape without collapsing, left part of the graph in fig. 2.3.

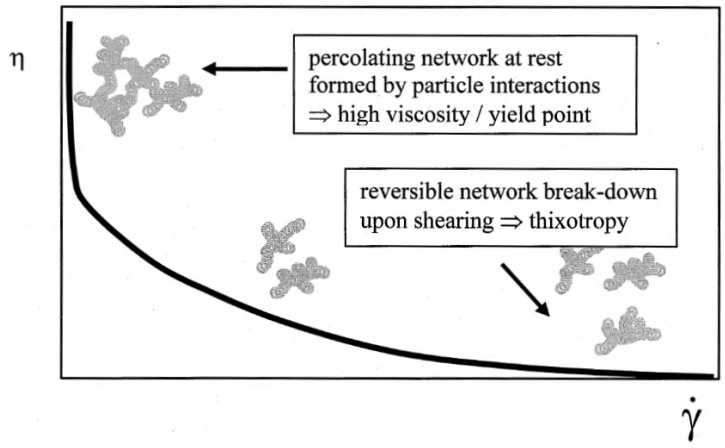

Figure 2.3: Dependence between shear rate, network structure, and viscosity [72].

2.2 EQUIPMENTS

This section will present and briefly explain the instruments used during ink preparations and characterization, manufacturing and printing of the pre-ceramic inks and characterization of the final objects.

2.2.1 *Thinky Mixer*

The centrifugal planetary mixer (ARE-250, Thinky Co., Japan) is a device used for both mixing and degassing a variety of different materials, such as metal pastes, pharmaceuticals, epoxy and polyurethanes, silicones, slurries, conductive pastes, medicines, chemical materials etc. This instrument works without using any agitator blades and, therefore, avoiding any contact between blades and the mixing paste. The material can be inserted with a 45° angle into the mixer through special cups, eventually with the help of proper adapters (also available refrigerated), or syringes. The mixing and degassing steps are carried out exploiting two different movements, fig. 2.4 (b):

- revolution: the material is moved away from the central part of the cup because of centrifugal forces;
- rotation: the container is rotated, allowing the material to flow (rotation and shearing).

The combination of these two mixing modes generates very strong shearing forces, capable of increasing powder dispersion into the liquid and to eliminate bubbles. In particular, the degassing of the paste is possible by changing the balance between revolution and rotation speeds. Firstly, centrifugal force, due to revolution, pushes the bubbles on the surface. Then, a slow rotation is applied, avoiding the

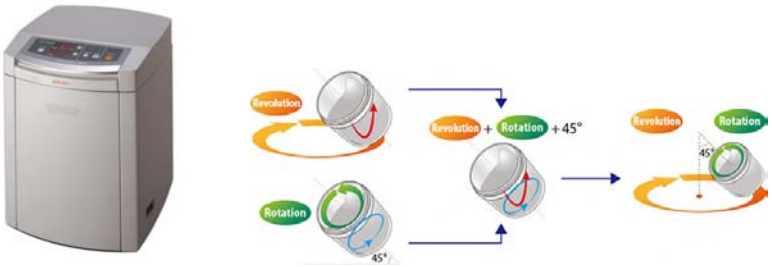

(a) *Centrifugal planetary mixer (ARE-250, Thinky Co., Japan).*

(b) *Mixing modes of Thinky Mixer ARE-250.*

Figure 2.4: Image and working principle of a planetary mixer.

encapsulation of new bubbles. The bubbles that come to the surface can than be eliminated by the shearing forces.

Before starting the mixing, it is necessary to insert the weight of the mixing complex (cup or syringe with eventual adapters), chose between mixing and degassing, set the rotation speed (in rounds/min) and the mixing or degassing time. Thinky Mixer ARE-250 allows inserting a maximum weight of 310 g.

2.2.2 *Rheometer*

MCR 302 viscometer (Anton Paar Germany GmbH, Ostfildern, Germany), fig. 2.5 (a) was used to measure the rheological behavior of the ink.

The setup used in this thesis work, consists on a plate-plate measuring system with an upper profiled plate and a lower sandblasted plate. The measuring parameters are set using a connected computer with a dedicated software supplied by the company.

The patented Toolmaster™ technology, fig. 2.5 (b), ensures automatic recognition of the measuring systems, accessories and all relevant parameters that are automatically transferred to the dedicated software. Many different types of cone and plate are available depending of the pastes to be analyzed.

The instrument is also equipped with a normal force sensor and a high-resolution optical encoder. It gives also the possibility to set the measuring temperature (from -160°C to 1000°C using additional temperature accessories) and to fill the measuring chamber with a desired liquid in order to control the atmosphere.

After setting their gap-height using the dedicated software, the paste is positioned between the two plates.

For viscosity measurement the upper profile plate starts to rotate increasing the speed over time i.e. increasing the shear rate, $\dot{\gamma}$, while

(a) *Overview of the rheometer.*

(b) *Detail of upper plate connection with the machine (Toolmaster™ technology).*

Figure 2.5: MCR 302 rheometer (Anton Paar Germany GmbH, Ostfildern, Germany) [73].

the torque on the upper plate is measured by the machine, allowing the calculation of the shear stress, τ.

Then, the yield stress, τ_0, the storage modulus, G', and the loss modulus, G'', can be measured by amplitude (or oscillatory) tests. After the first step with gamma amplitude of 100%, the paste is left to rest for 1 h maintaining the temperature constant. Finally, the strain is logarithmically ramped from 0.001% to 100% at 1 Hz frequency (always at the same temperature).

2.2.3 *Printers*

During this thesis work, two different printers were used in order to extrude the pre-ceramic pastes. Both of them have been run using compressed air as a source of pressure, allowing paste extrusion of a long single filament that will form the final object.

The first one, 1.5.1, is a direct ink wrinting (DIW) printer, while the second one is a robocaster, 2.2.3.2: the only difference is the movement mechanism of the nozzle, that is accomplished with three arms controlled by as many belts in the first case and with a single six-axis *robotic arm* in the second case. In order to distinguish between the two printers, the first will generally be named *"DIW printer"* (2.2.3.1) while the second one will be named *"robocaster"* (2.2.3.2).

2.2.3.1 *DIW printer*

During the work done at University of Padua, a DELTA WASP 20x40 TURBO 2 printer (WASP, Massa Lombarda, Italy) was used to perform scaffolds direct ink writing.

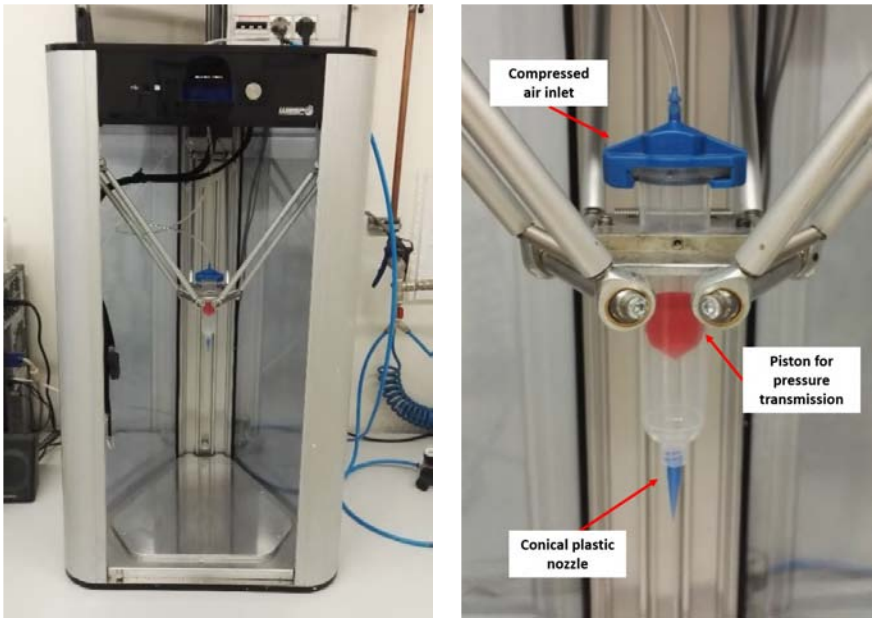

(a) *Overview of DIW printer.*

(b) *Detail of nozzle and syringe used for printing.*

Figure 2.6: DELTA WASP 20x40 TURBO 2 (WASP, Massa Lombarda, Italy) [74].

The printer is visible in fig. 2.6. The ink is firstly inserted into a syringe and then mounted on the device. The syringe is connected to a Teflon pressure channel using a proper adapter as shown in fig. 2.6 (a). Then, the paste is extruded through a conical plastic nozzle (Nordson EFD, USA), available with different sizes, by applying external pressure on the piston (in red in fig. 2.6 (b)). The pressure is supplied by compressed air that passes through the Teflon tube and it can be regulated using a valve attached to a pressure gauge, in such a way to modify the ink flow during printing. The printer is also equipped with a digital display where it is possible to set the printing program (uploaded via USB stick), the zero point and the printing speed. The latter can be changed and adjusted also during printing. After the deposition of the first layer, the nozzle will go up, following the instruction given by the selected printing program.

2.2.3.2 *Robocaster*

During the work done at Friedrich-Alexander-Universität Erlangen-Nürnberg, a six-axis robotic system (RobFab, Battenberg ROBOTIC GmbH & Co. KG, Marburg, Germany) was used for scaffolds printing, 2.7.

The robocaster is equipped with a real time tactile and optical sensor control (200 Hz) combined with a extrusion device driven by a

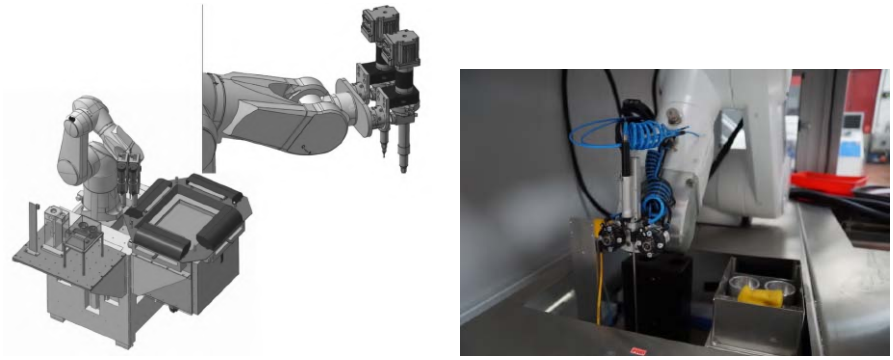

(a) *Scheme of the printing system.* (b) *Detail of the printing arm.*

Figure 2.7: Robocaster system (RobFab, Battenberg ROBOTIC GmbH & Co. KG, Marburg, Germany).

(a) *Circular cross-section nozzle with diameters of 0.5, 0.3, 0.2 mm (from the left).*

(b) *Circular (d_0=1.5 mm) and square (l_0=1.5 mm) nozzles with the possibility of inserting different mandrels to obtain hollow filaments.*

Figure 2.8: Images of nozzles that can be mounted in the robocaster to obtain filament with different shapes.

progressive cavity pump. This system allows a continuous deposition of a gel filament with high geometrical precision (<50 µm) [69]. The 400x400x400 mm^3 fabrication chamber is shown in fig. 2.7. The robocaster can work with both single-screw micro-extruder or using compressed air and it is equipped with a dual channel deposition system, allowing the simultaneous printing of two scaffolds or with two inks. Pressures are controlled during printing by two valves connected to as many pressure gauges. The maximum recommended pressure, to avoid damaging the channels where the compressed air is flowing, is equal to about 6 bar. The paste is extruded through custom stainless steel nozzles (Erker Funkenerosion, Nürnberg, Germany) than can have different shapes, allowing the printing of circular, square and hollow filaments, as shown in fig 2.8.

Also in this case, the ink is loaded into a syringe and positioned inside the robocaster. The latter is connected to a computer that allows to set all the different printing variables (except pressure) by using a dedicated software. Therefore, after machine calibration, it will be pos-

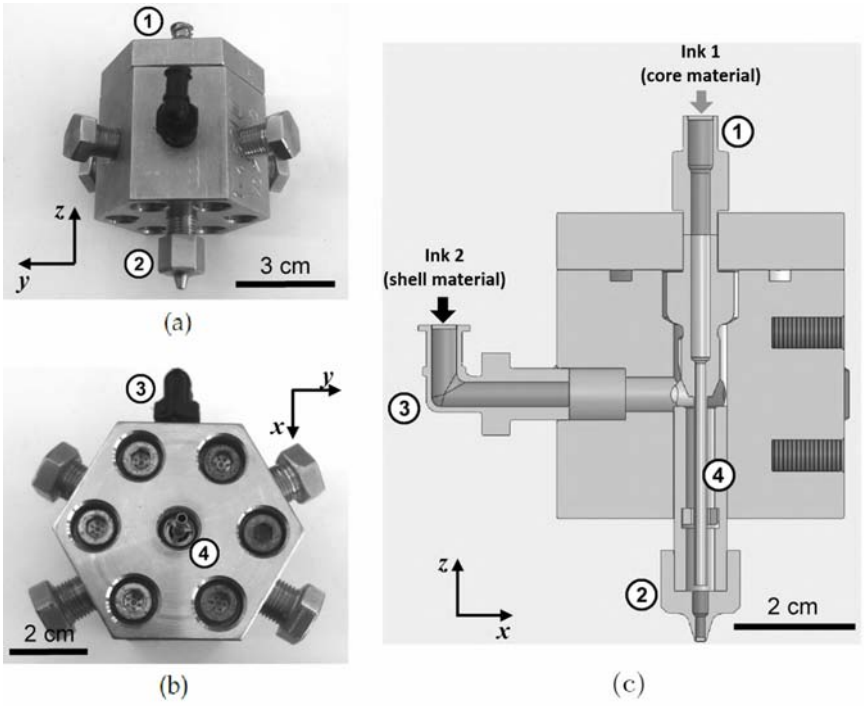

Figure 2.9: Setup of the adapter for co-extrusion [75]. Side (a) and bottom (b) view. Cutaway view from 3D model (c). Different components are enumerated in the figure: ① core ink feeding channel, ② extrusion nozzle, ③ shell ink feeding channel and ④ final part of the core feeding channel.

sible to upload the printing program, set the nozzle-substrate distance and the printing speed. It is not possible to change the printing speed while the robotic arm is moving, action possible with the previously described printer, 2.2.3.1. The printer is closed by doors equipped with an opening sensor that will immediately stop the printing process if they are opened. After the deposition of the first layer, the fabrication chamber will go down, following the instruction given by the selected printing program.

This machine permits also to perform co-extrusion of two different pastes using the dedicated setup shown in figure 2.9 [75]. This setup consists of a stainless steel casing and two different feeding channels, one for the core material and one for the shell material. In particular, the inner feeding channel for the core paste has a diameter of 1.5 mm, fig. 2.9 (b) and (c). The two syringes will be mounted in the two feeding openings, named Ink 1 and Ink 2 in fig. 2.9 (c), and the pressure applied to each of them is regulated by the two already cited valves and pressure gauges.

Figure 2.10: Keyence VHX-6000 (Keyence Deutschland GmbH, Neu-Isenburg, Germany).

2.2.4 *Microscopes*

In the following pages, optical and scanning electron microscopes used during the thesis work are briefly presented and explained.

2.2.4.1 *Optical microscopies*

Two different optical microscopes were used to evaluate the quality of the 3D printed scaffolds.

ZEISS STEMI 2000 C (Carl Zeiss Microscopy, Thornwood, New York, US) allows a magnification up to 50x. The microscope is associated with a digital device, AxioCam ERc5s, and connected to a computer that allows viewing using a dedicated software.

KEYENCE VHX-6000 (Keyence Deutschland GmbH, Neu-Isenburg, Germany) is a new generation optical microscopy featuring a very wide magnification range from 0.1x to 5,000x thanks to the possibility to easily interchange lenses. This instrument is also able to rotate around an object for a full 360-degree inspection. The microscope is provided with a system comprising a dedicated software for image capturing and processing, a 23-inch full HD LCD monitor as well as a 500 GB hard disk drive for easy storage of images, video, and measurement data. It includes also a console for easily accessible XYZ control. Therefore, it will be possible to move the sample (X, Y, Z direction) and the lens (Z direction) acting on the provided joystick, 2.10.

2.2.4.2 *Scanning electron microscope (SEM)*

In order to evaluate the microstructure of printed scaffolds, including eventual open porosity and discontinuity like cracks, it is necessary to use a scanning electron microscope (SEM). In particular, images

were captured using a FEI Quanta 200 (FEI Ltd, Hillsboro, OR, USA). Before SEM analysis, the pyrolyzed samples were polished with a 1µm diamond finish and sputtered with gold. The instrument is also equipped with energy-dispersive X-ray spectroscopy (EDS) that can be used for the elemental analysis or chemical characterization of a sample.

2.2.5 *X-ray diffraction (XRD)*

The study of samples crystalline phases was performed using a X-ray diffraction machine, Bruker AXS D8 Advance (Bruker, Karlsruhe, Germany), fig. 2.11(a), using a Cu-Kα radiation. The material was firstly ground to obtain a fine powder that was later positioned into the machine using a specific sample holder.

X-ray are electromagnetic waves that found interest in the field of crystallography. In fact, their wavelength is comparable (same order of magnitude) to the interatomic distance within a crystalline solid (0.5-2.5 Å[76]), allowing the investigation of the internal structure of a given material.

X-rays are generated from the braking of accelerated electrons within a heavy material such as copper or lead [77]. Electron deceleration causes energy loss by X-ray waves emission. Therefore, an X-ray beam that impacts the material will be scattered with the same wavelength in all the directions by atoms constituting the irradiated crystal. However, in some specific directions, it is possible to observe an increase in the intensity of incident radiation due to the constructive interference of the scattered waves. From fig. 2.11 (b), it easily understandable the condition of constructive interaction. Thus, given an X-ray beam with wavelength λ, impacting a crystal with interplanar distance d at an incident angle θ, constructive interference will be observed when the wavelengths of two reflected X-rays, scattered from different planes, e.g. plane 1 and 2 in fig. 2.11 (b), differ by an integer multiple of the incident monochromatic radiation wavelength. The law that describes this condition is called Bragg's law:

$$2d \sin\theta = n\lambda \tag{2.1}$$

where n is an integer number higher than zero. Using eq. (2.1) and knowing λ and θ, it is then possible to estimate the interplanar distance d. During the measurement, the θ angle is varied by the emitter while the receiver follows its movement simultaneously. The result is diffractogram, that is an intensity-2θ graph characterized by intensity peaks whose positions give us information about the crystalline phase while from their intensity and width it is possible to deduce composition and crystallite dimensions.

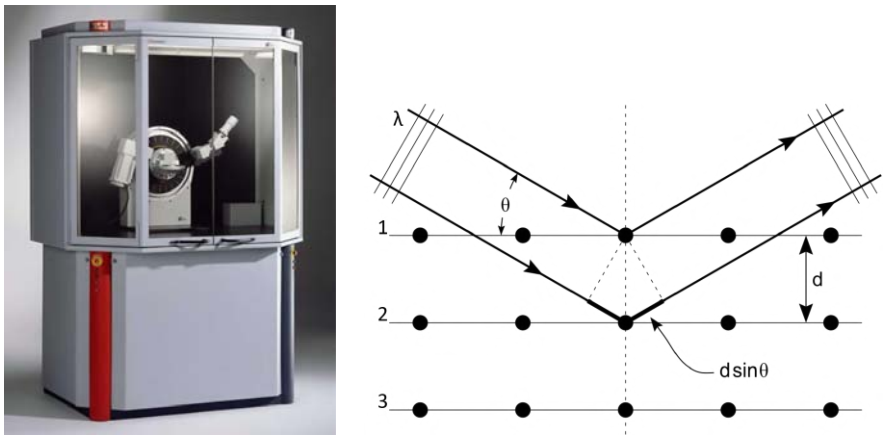

(a) *Bruker AXS D8 Advance (Bruker, Karlsruhe, Germany).*

(b) *Scheme of X-ray diffraction working principle.*

Figure 2.11: X-ray diffraction system and scheme of X-ray diffraction working principles.

The instrument was set using a potential difference of 40 kV and a current intensity of 40 mA in order to produce X-ray with proper characteristics. The 2θ angle was varied between 10° to 70°, using a 0.05° step size every 2 seconds. Phase identification was performed using Match! software package (Crystal Impact GbR, Bonn, Germany) supported by ICDD PDF-2 Powder Diffraction File (International Center for Diffraction Data, Newtown Square, PA, USA) as the reference database.

2.2.6 *Pycnometer*

Gas pycnometry is one of the most reliable techniques for obtaining apparent (or skeletal) and true volumes or densities. A helium Micrometrics Accupyc II 1340 (Micromeretics, USA) pycnometer was used to measure these quantities, sec. 2.4.3 and 2.4.5.

This non-destructive method uses an inert and very light gas (He), able to easily diffuse through the sample, in order to measure its apparent volume i.e. excluding all open porosity, even the very small one. The sample is inserted into a chamber of known volume, calculated by a previous calibration using a metallic ball of known mass. Different chamber dimensions are available (1 cm^3, 3.5 cm^3) with as many calibration balls. The instrument calculates the volume occupied by the specimen from the pressure variation of the inert gas between inlet and outlet. Therefore, giving to the instrument the sample mass, the density is consequently calculated by the pycnometer. This value is an average of the number of measurements (*run*) that the user can decide and it is given together with the standard deviation.

2.2.7 *Instron for compression and bending tests*

During this thesis work, two machines for mechanical testing were used:

- Instron 1121 UTM (Instron Danvers, MA, USA) at University of Padua for compression tests only;
- Instron 4204 UTM (Instron Corporation, Canton, USA) at Friedrich-Alexander-Universität Erlangen-Nürnberg for both compression and bending tests.

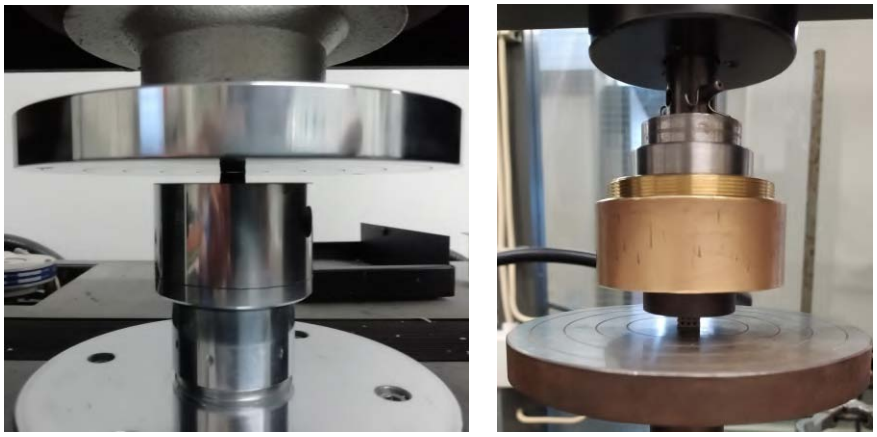

(a) *Instron 1121 UTM (Instron Danvers, MA, USA)*

(b) *Instron 4204 UTM (Instron Corporation, Canton, USA).*

Figure 2.12: Instron setup for compression test.

Both machines work with imposed displacement while the load is applied by a moving crosshead that travels in a vertical direction. Different setups can be used depending on the type of test to perform: compression test, tensile test, three point bending test and four point bending test. During this work, only compression test and four point bending test were performed. The two different setups for compression test are shown in fig. 2.12. Instron 1121 UTM consists on two steel plates: the lowest one is fixed while the top plate can move in vertical direction. Instron 4204 UTM is very similar, except for having an adaptive top plate thanks to its small mechanical backlash.

As regards the bending tests, the lower part, called *support span*, consist in two fixed supports that can be positioned at two different distances: 20 or 40 mm. The upper part, called *load span* is composed by a head equipped with two pushing bars. Two different heads are available, one with a load span of 10 mm and the other one with a load span of 20 mm.

Figure 2.13: Instron 4204 UTM setup for bending test (support span=20 mm, load span=10 mm).

The load in Newton (N) is measured by a load cell and the force is displayed and plotted in real time as a function of time on the dedicated software connected to the machine.

2.2.8 *Furnaces*

Two tubular furnaces for pyrolysis in inert atmosphere were used to perform all the heat treatment. Both of them are programmable via segments, allowing the desired temperature profile to be entered.

CARBOLITE CTF 12 (Hope, UK) was used at University of Padua. This furnace can work with nitrogen atmosphere up to 1000°C.

GLO40 (Gero GmbH, Neuhausen, Germany) was used at Friedrich-Alexander-Universität Erlangen-Nürnberg. This furnace can work with both nitrogen and argon up to 1300°C.

2.3 EXPERIMENTAL PROCEDURE

This section means to present and explain the experimental procedure that led to scaffolds manufacturing. Firstly, geometry designing will be briefly explained. Then, the pre-ceramic ink preparation process will be illustrated, followed by the performed drying and thermal treatment to obtain the final ceramic.

2.3.1 *Geometry*

Every 3D printing process starts with the design of the desired geometry. During this thesis work, previous geometries have been used, implementing only small resizing where necessary. Macroporous ceramic scaffolds with theoretical density between 50 and 65% were printed using the two already presented 3D printers, 2.2.3. Direct ink writing (or robocasting) is an additive manufacturing process which consists on the deposition of a single long filament that, by following a precise and previously designed path, will form the final scaffold layer by layer. Therefore, the *"rule of thumb"* when designing using this technology is that the component must be obtained from a single continuous filament.

Whereas the newly printed layer will inevitably tend to slightly collapse, it is good practice that the distance between two successive layers is equal to 0.8 d_0, where d_0 is the nozzle diameter. This will also allow a better joint between layers. However, this rule is not fixed, but it is strictly related to ink behaviour and rheology.

In this thesis, the adopted geometries are very simple, consisting of a crossed lattice where two successive layers are arranged respectively at 0° and 90°. This geometry is relatively simple for both designing and printing and allows a reliable and effective comparison between scaffolds having a different cross-section such as circular, square, hollow and co-extruded. Furthermore, it would be very easy to change the porosity of the scaffold by changing the spacing between two close filaments.

2.3.1.1 *Geometry design for DIW*

As already shown, DELTA WASP 20x40 TURBO 2 was used as printer for direct ink writing manufacturing during the experimental period at the University of Padua, 2.2.3.1. Here, a conical plastic nozzle with a diameter, d_0, of 0.016 inches (0.4064 mm), blue in fig. 2.6 (b), was used to extrude the pre-ceramic ink. Geometries must be defined in a machine-readable format, in particular using the machine code *g-code* that can be easily written using the on-line software NC-Viewer [78]. The used *g-code* for a 0°-90°, 14-layer scaffold with dimension of 10x10x5 mm^3 is shown in fig. 2.14. The spacing between two fila-

ments is equal to nozzle diameter d_0 while the distance between two successive layers is equal to 0.8 d_0.

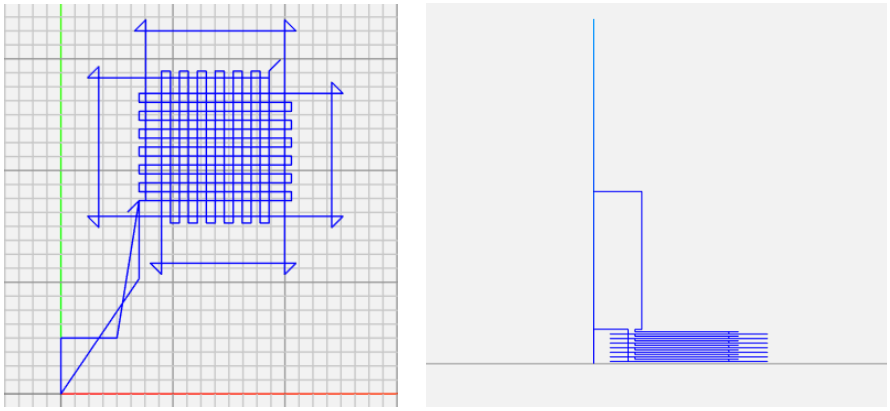

(a) *Top view.* (b) *Side view.*

Figure 2.14: NC-Viewer images of scaffolds geometry.

2.3.1.2 *Geometry design for robocasting*

Scaffold design for the robocaster system, 2.2.3.2, is very similar to the previous one, 2.3.1.1, and the design process is specular. However there are some differences:

- different nozzle diameters and shapes were used during the experimental work at Friedrich-Alexander-Universität Erlangen-Nürnberg. In particular, circular cross-section steel nozzles with a diameter 0.012 inches (0.3 mm), 0.02 inches (0.5 mm) and 0.059 (1.5 mm) and square cross-section steel nozzle with a side of 0.059 (1.5 mm) were adopted, as shown in fig. 2.8. Therefore, it is important to consider these diameter by designing a suitable geometry;
- the 1.5 mm side square nozzle has been treated in the same way as the 1.5 mm diameter circular nozzle as regards geometry design;
- the adopted geometries were previously elaborated using the custom designed CNC software PyCaster and exported to *g-code* format, readable by the machine.

The printed geometries respect the same standards as the scaffolds in Padua, i.e. the distance between two close filaments is equal to the nozzle diameter, two successive layers are arranged respectively at 0° and 90° while the increase in height between two deposited layers is equal to 0.8 d_0 (where d_0 is the nozzle diameter).

2.3.2 *Preparation of the pre-ceramic ink*

The preparation of pre-ceramic ink is a crucial part of scaffold manufacturing using DIW (or robocasting). Four main different pre-ceramic pastes were prepared using the previously presented materials, 2.1, mixed with isopropanol (IPA). The aim is to obtain a final scaffold with about 65-70%wt of calcite ($CaCO_3$), i.e. the bioactive phase 1.3.2, dispersed in a matrix derived from pre-ceramic polymer decomposition. The following step is to add carbon fibers into the ceramic matrix.

Table 2.4: Compositions of the main four pre-ceramic inks.

Name	Pre-ceramic polymer	†$CaCO_3$	†IPA	†Carbon fiber
Ink-1	Silres MK®	1.94	0.47	
Ink-2	Silres MK®	1.94	0.51	0.28
Ink-3	Silres H44®	1.63	0.35	
Ink-4	Silres H44®	1.63	0.38	0.23

†*than the amount of pre-ceramic polymer*

Taking into account the different ceramic yield under inert atmosphere between Silres MK® and Silres H44®, 84%wt and 70%wt respectively (2.1.1), the prepared pre-ceramic inks can be classified with reference to the quantity of pre-ceramic polymer, table 2.4: the numbers in table express the value of the weight ratio between the corresponding pre-ceramic polymer (*"pre-ceramic polymer"* column) and the material considered.

However, variations of ink-1 and ink-2 have been tested. These two compositions, shown in table 2.5, have been named ink-1* and ink-2*.

In particular, ink-1* differs from ink-1 by the addition of fumed silica, 2.1.2, adopted to adjust the rheological behavior. As increasing the amount of fumed silica, it is necessary to decrease the amount of pre-ceramic polymer i.e to increase the $CaCO_3$/Silres MK® ratio, equal to 2.17 in tab. 2.5, in order to keep constant the weight percent of $CaCO_3$ in the final pyrolyzed scaffold. Then, the final matrix composition will be composed of a mixture of fumed silica and the phase resulting from Silres MK® decomposition. Therefore, despite this operation is in contrast with the target of obtaining as much pyrolytic carbon as possible from pre-ceramic polymer decomposition (1.1), it was a necessary compromise when printing with nozzle diameter (or side) of 1.5 mm.

Ink-2*, on the other hand, differs from ink-2 by the half amount of carbon fibers.

Table 2.5: Compositions of the main four pre-ceramic inks.

Name	Pre-ceramic polymer	†$CaCO_3$	†IPA	†Carbon fiber	†Fumed silica
Ink-1*	Silres MK®	2.17	0.62		0.09
Ink-2*	Silres MK®	1.94	0.51	0.14	

†*than the amount of pre-ceramic polymer*

Before explaining the ink preparation processes, it is necessary to make some considerations about the used solvent, isopropanol. This chemical compound is a very common, cheap, widely available and moderately volatile solvent with a strong odor. In particular, its volatility has both advantages and disadvantages. On the one hand, this allows the solvent to slightly evaporate as soon as filament exits the nozzle, allowing better shape retention [66]. On the other hand, isopropanol will slowly evaporate also during ink preparation and printing. Consequently, the final viscosity of the ink, which is strictly connected to the quantity of solvent, is closely related to the duration of the ink preparation process, to the process itself (mixing speed, mixing mode, etc.) and to the environment (temperature and humidity). Furthermore, isopropanol will tend to evaporate also inside the syringe, increasing the viscosity of the paste as the print proceeds, making its storage problematic and its use preferable within a relatively short window of time after preparing the ink.
For all these reasons, it is very difficult to obtain exactly the same ink even if the amount of isopropanol and the preparation process are exactly the same. Therefore, the reader is requested to keep in mind that the quantities of isopropanol in tables 2.4 and 2.5 are indicative and may slightly vary depending on printing and preparation conditions.

In conclusion, a certain sensitivity and manual skills are required from the operator in charge of preparing the ink.

The procedure for preparing the different pre-ceramic inks using the quantities in tab. 2.4 and 2.5 will be illustrated below.

2.3.2.1 *Ink-1 and ink-3*

Ink-1 and ink-3 are only made by pre-ceramic polymer, (Silres MK® or Silres H44®), and $CaCO_3$ mixed in isopropanol, tab. 2.4.

Pre-ceramic polymer and calcite are firstly weighed using plastic laboratory trays. After that, isopropanol is poured and weighed into a cup suitable for the Thinky Mixer, 2.2.1. Then, the pre-ceramic polymer is dissolved by mixing with isopropanol. During this step, pre-ceramic polymer and IPA can be mixed together by hand or by inserting the closed cup into the mixer at 1200 rounds/min for 30 seconds.

When the pre-ceramic polymer is completely dissolved, calcite can be mixed together and, after a first phase of manual mixing, the cup is closed to avoid isopropanol evaporation and inserted into the Thinky Mixer at 1200 rounds/min for 3 min. At this point, it is necessary to check if the viscosity is suitable for printing, a step that requires some experience and previous printing attempts. If the ink appears too liquid, it is possible to mix again without covering the cup, taking into account that about 0.2-0.3 g of isopropanol will evaporate for every minute at 1200 rounds/min.

After mixing, the ink can be inserted into the syringe where the degassing at 2000 rounds/min for 6 minutes is performed.

2.3.2.2 *Ink-1**

As already written, ink-1* is very similar to ink-1, except for the addition of fumed silica. Consequently, also the preparation is very similar. The only difference is that before adding $CaCO_3$, fumed silica is added and mixed with isopropanol and the pre-ceramic polymer using the Thinky Mixer for 1 min at 1200 rounds/min.

Then, considering that this preparation was used at Friedrich-Alexander-Universität Erlangen-Nürnberg when printing with 1.5 mm nozzles, it has proved appropriate to add another degassing step, 2000 rounds/min for 5 min, directly in the cup before inserting the pre-ceramic ink into the syringe.

2.3.2.3 *Ink-2, ink-2* and ink-4*

The preparation of ink-2, ink-2* and ink-4 is also very similar to those of the previous pastes. The only difference is the addition of carbon fibers to the pre-ceramic polymer and isopropanol mixture before calcite. Therefore, carbon fibers and pre-ceramic polymer are mixed together in isopropanol using the Thinky Mixer for 1 min at 1200 rounds/min.

It can happen that carbon fibers form some agglomerations. In this case, it is sufficient to insert the cup into an ultrasonic bath for 1 min to avoid this unwanted phenomenon.

2.3.3 *Printing*

After explaining the various ink preparations, it is time to go deeper into the printing process. Considering that two different printers have been used during this thesis work, this section will be divided into two parts, 2.3.3.1 and 2.3.3.2.

2.3.3.1 *Direct ink writing printing process*

Direct ink writing (DIW) was performed during the period spent at the University of Padua using the already explained printers in fig. 2.6, 2.2.3.1. Only 0.016 inches (0.4064 mm) nozzle was used for this purpose.

The syringe, filled with the ink, is positioned into the machine as shown in fig. 2.6 (a) and connected to compressed air by the blue adapter in fig. 2.6 (b). The printing substrate, consisting on a transparent plastic sheet, is covered with a thin layer of common sunflower oil to avoid sticking and helping to remove the printing scaffold. Then, it is positioned at the base of the machine.

Then, the printer is turned on and the calibration can take place by establishing the *"zero point"*: the syringe is moved in vertical direction (Z direction) until it touches the substrate, taking care not to damage the nozzle by going down too much. Then it is necessary to go up a little bit, usually 0.3-0.4 mm when printing with a 0.016 inches (0.4064 mm) nozzle. This distance is not well defined and has to be found through a trial and error approach [74].

Finally, using the printer display, the operator selects the desired geometry through the appropriate *g-code* file. At this point, it is possible to modify the ink flow changing the pressure by acting on the valve connected to a pressure gauge and/or to change the printing speed thanks to the display. Playing with these two parameters, material flow can be adapted to the prepared ink and environmental conditions. In particular, the possibility to change the speed while printing, not available with the robocaster (2.2.3.2), is a very useful feature: in fact, although the pressure can be changed at will, operating with relatively high pressures, in order to follow the set speed, can cause filament instability phenomena, fig. 2.15 (b). A good printing pressure, dictated by experience, is around 2-3 bar.

2.3.3.2 *Robocasting printing process*

Robocasting, 2.2.3.2, was performed during the period spent at Friedrich-Alexander-Universität Erlangen-Nürnberg. In particular, the prepared inks, 2.3.2, have been extruded using different nozzle shapes and diameters, as shown in tab. 2.6.

As illustrated, four main different shapes of filament were extruded in the form of scaffolds:

- full circular cross-section i.e. full cylindrical filaments;
- hollow circular cross-section i.e. hollow cylindrical filaments;

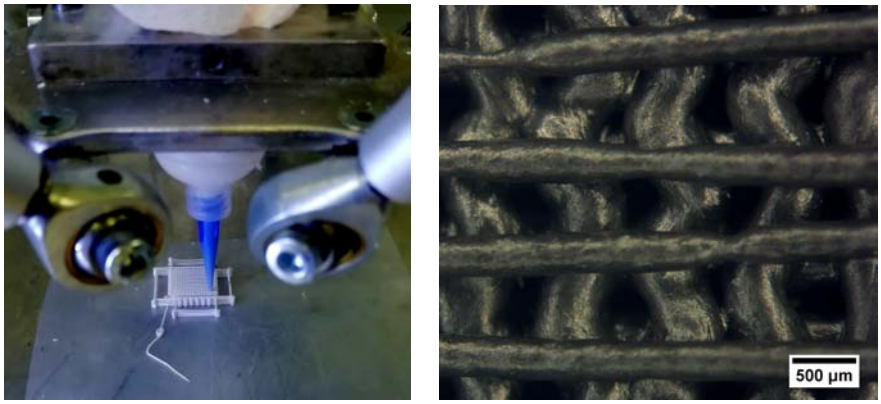

(a) *DIW printer in action (0.4064 mm nozzle).*

(b) *Filament instability due to high pressures (ink-4, 2.3.2.3).*

Figure 2.15: DIW printing process and issues.

- full square cross-section i.e. full square filaments;
- co-extruded filaments consisting of two different pastes, one forming a full circular cross-section in the middle part (*core*) and the other one disposed in the circular crown around it (*shell*).

Table 2.6: List of different nozzle geometries and printed filaments performed using the robocasting machine.

Printed filament	Nozzle cross-section and dimension	Ink
Full cylindrical	circular d_0=0.3 mm	ink-1, ink-3
	circular d_0=0.5 mm	ink-1, ink-1*, ink-2*
	circular d_0=1.5 mm	ink-1*, ink-2*
Hollow cylindrical	circular d_0=1.5 mm with d_m=0.75 mm	Ink-1*
Full square	square l_0=1.5 mm	ink-1*, ink-2*
Co-extruded	circular with d_{shell}=1.5 mm and d_{core}=0.75 mm	shell=ink-1*, core=ink-2*
		shell=ink-2*, core=ink-2*

where d_0= circular nozzle diameter, d_m= mandrel diameter, l_0= side length of the square nozzle, d_{shell}= external diameter for co-extrusion, d_{core}= core feeding channel diameter.

All the preliminary pre-printing operations are very similar to all these cases. After degassing, the syringe is mounted into a proper adapter arm to connect it with the robocaster. This component differs

between conventional single paste extrusion and co-extrusion. For single paste extrusion, two different adaptive arm setups, in fig. 2.16 of chapter 3 (sec. 3.1), have been tested: the first one, fig.2.16 (a), was supplied by the company, while the second one, fig.2.16 (b), was manufactured especially for the used inks by the mechanical workshop belonging to the hosting institute.

Regarding co-extrusion, the setup, already shown in fig. 2.9, is very close to the one in fig. 2.16 (a), but with the possibility to add a second syringe on one side, fig. 2.17 (b).

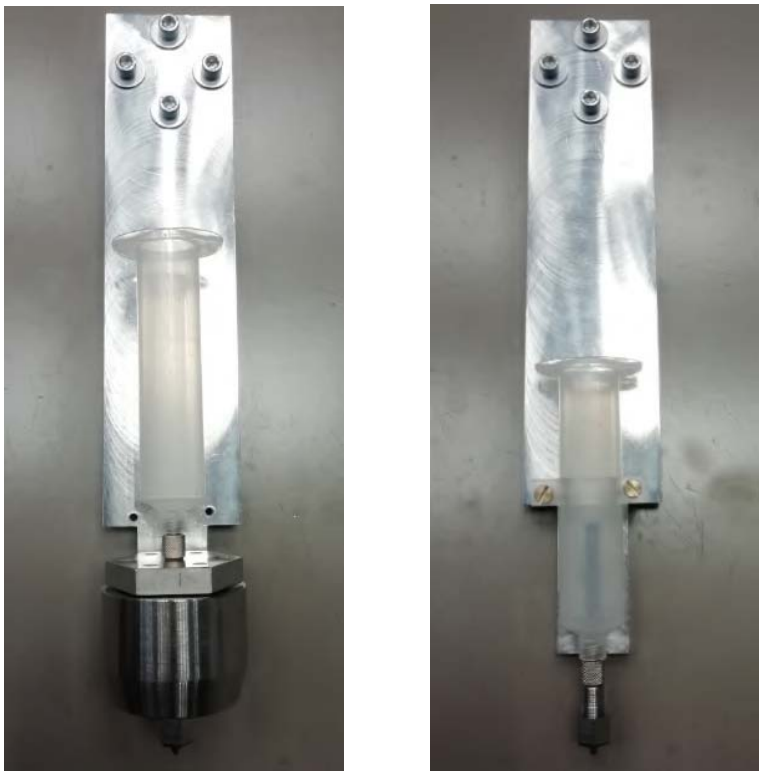

(a) *Setup supplied by the company.* (b) *Custom setup.*

Figure 2.16: Different adapter arm setups for single paste robocasting.

After turning on the machine and mounting the syringe to the proper adapter arm, it is possible to connect the apparatus with the robocaster and the pressure channel(s). The printing substrate, typically an alumina plate, is now positioned into the fabrication chamber. Then, after starting the dedicated software using a computer connected to the machine, the calibration can take place. After that, the zero point i.e. the initial distance between the nozzle and the substrate in mm has to be defined together with the printing speed in mm/s. The zero point depends on the current nozzle and has to be found by trial and error approach. The final step is to select the desired geometry and

start printing. The pressure acting on the syringe is controlled by a valve connected to a pressure gauge. Pressures of about 3-4 bar have proven to be suitable for obtaining a good scaffold, able to maintain the shape during the drying step, fig. 2.3.4. As already written, 2.2.3.2, the machine does not allow to open the doors or change the speed during the printing phase: this is the main disadvantage of the machine.

When printing co-extruded filaments, the shell material will fill the metal casing, in fig. 2.9, before the extrusion can happen.

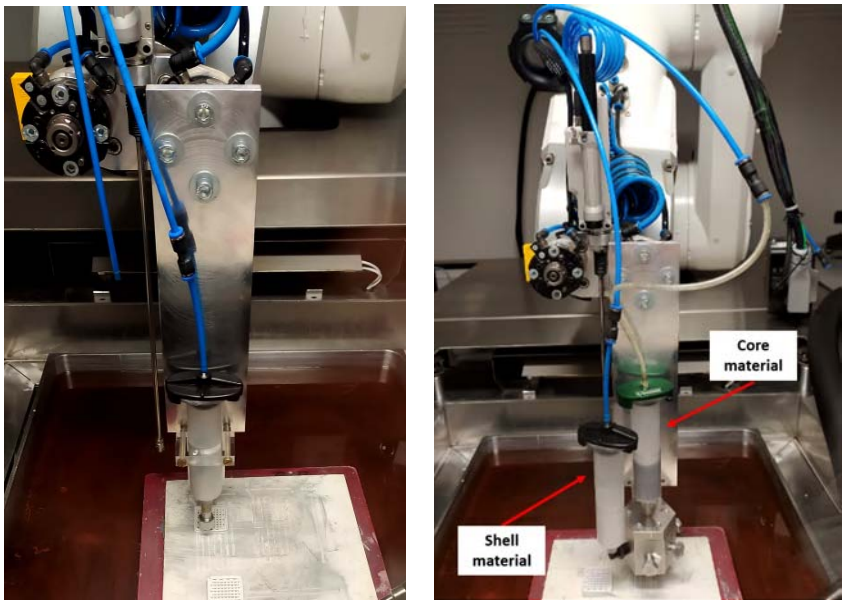

(a) *Single ink robocasting.* (b) *Co-extrusion.*

Figure 2.17: Robocaster in action.

One variation was made during printing hollow filaments i.e. it was also tried the extrusion using a substrate immersed in vegetal sunflower oil.

2.3.4 *Drying and thermal treatment*

The next step, after printing, is drying in air at room temperature where most of the solvent (isopropanol) evaporates. The drying time is not fixed and it strongly depends on the environmental conditions (temperature, humidity) and the ink. In fact, scaffolds printed with a larger nozzle, i.e. 1.5 mm, will require more time for drying because it is necessary to allow sufficient time to isopropanol in the central part of the filament to pass through the material and then evaporate. Obviously, if the filament is very thin, the thickness that isopropanol must go through is less, requiring a shorter drying time. For thin

filament scaffolds, 24 h at room temperature is enough, while for thicker filament scaffolds it is necessary to wait for at least 48 h.

Hollow filament scaffolds printed in sunflower oil are a separate matter: firstly, they were left into the oil bath overnight for a preliminary drying and then, they were removed from the oil bath and left over a paper tissue to take out the excess oil and dry for at least 24 h.

After drying, all the scaffolds are weighed and measured using a digital caliper.

The following critical step is pyrolysis under inert atmosphere (nitrogen). The specimens are placed on a refractory support, fig. 2.18 (a) and then inserted into the furnace, 2.2.8. Although this passage may seem trivial, it is important to place the scaffolds in the very central part of the furnace to ensure homogeneous and complete pyrolysis. In fig. 2.18, is shown the case of incomplete pyrolysis of the scaffolds placed on the sides (far from the middle of the furnace).

After closing the furnace, a first vacuum is made thanks to a special vacuum pump and the chamber is filled with nitrogen. To ensure that no air is present, this process is repeated two or three times. Now, it is possible to program the desired temperature profile for pyrolysis. The heat treatment is the same for all the different preparations in tab. 2.4, and it is shown in fig. 2.19. In particular, it is divided into five main steps:

- heating with a 0.5°/min linear ramp from room temperature to 350°C;
- dwelling time of 1h at 350°C i.e. cross-linking step;

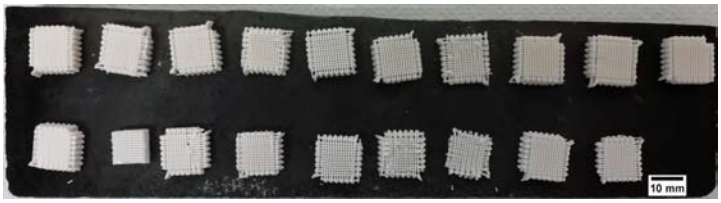

(a) *Before pyrolysis.*

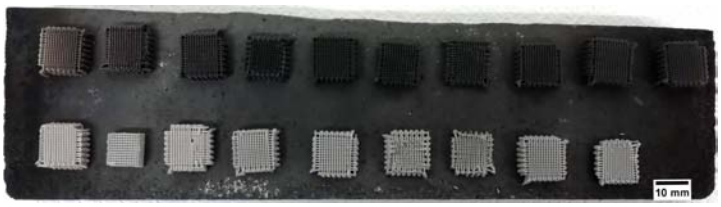

(b) *After pyrolysis (incomplete pyrolysis).*

Figure 2.18: Scaffolds before and after pyrolysis (first row=ink-1, second row=ink-3).

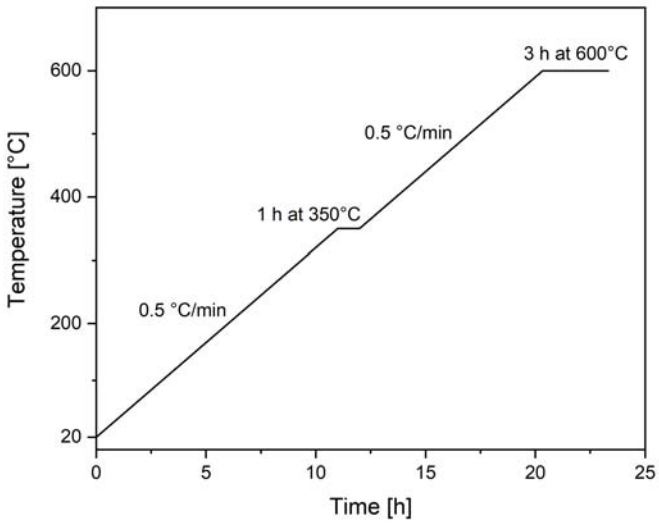

Figure 2.19: Representation of the temperature profile for the pyrolysis treatment.

- heating with a 0.5°/min linear ramp from 350°C to 600°C;
- dwelling time of 3h at 600°C i.e. ceramization;
- natural cooling inside the furnace.

As already explained, the target is to avoid $CaCO_3$ decomposition that starts at around 650-700°C. For thin filament scaffolds, a final dwelling time of 1h at 600°C (ceramization) is sufficient[43]. However, considering that for thicker filament it could not be enough, it was decided to dwell every scaffold for 3h at 600°C.

These temperatures were set thanks to thermogravimetric analysis (or thermal gravimetric analysis, TGA) and in agreement with previous works carried out by Elsayed *et al.*[43] and Fiocco *et al.*[40]. This measurement was performed for ink-1 and ink-3 (tab. 2.4) using an heating rate of 5°C/min from room temperature to 1000°C, fig. 2.20. Ceramization in nitrogen atmosphere at 600°C allows calcite to not decompose.

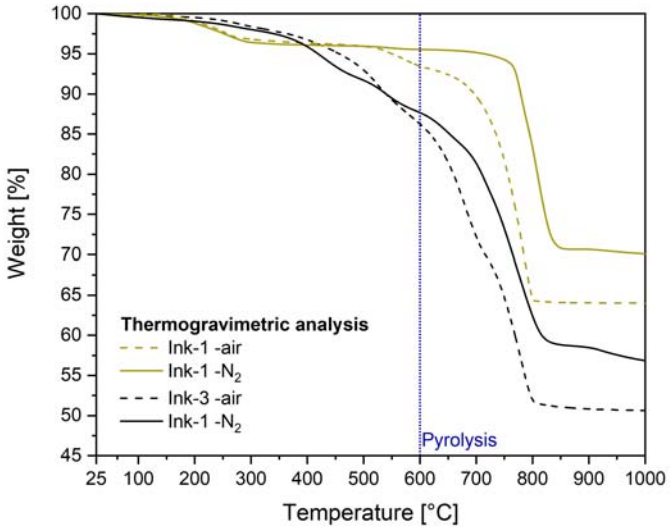

Figure 2.20: Thermogravimetric analysis of ink-1 and ink-2 (tab. 2.4).

2.4 CHARACTERIZATION

In the previous sections, the material, 2.1, the equipment, 2.2, and the experimental procedures performed during this thesis work (2.3) were explained. In the following pages, it will be illustrated how the instrumentation was used in order to characterize the printed scaffolds.

The rheology of the different pastes was firstly measured using the rheometer, 2.2.2. The printed scaffolds were observed through optical microscopy, 2.2.4.1, before and after pyrolysis, and also through SEM and EDS, 2.2.4.2, after pyrolysis. After measuring the linear shrinkage, the structural integrity was studied by establishing apparent (or skeletal) and true density through pycnometer measurements, 2.2.6, while the geometrical (or bulk) density was estimated with a digital caliper. These allowed calculating the open and closed porosity of printed scaffolds.

Then, the mechanical performances were measured by compression test on scaffold specimens and by bending test on single filaments using the Instron universal testing machine, 2.2.7.

Scaffold powders were then collected to assess the crystalline composition through XRD analysis in order to check that no decomposition of calcite occurred.

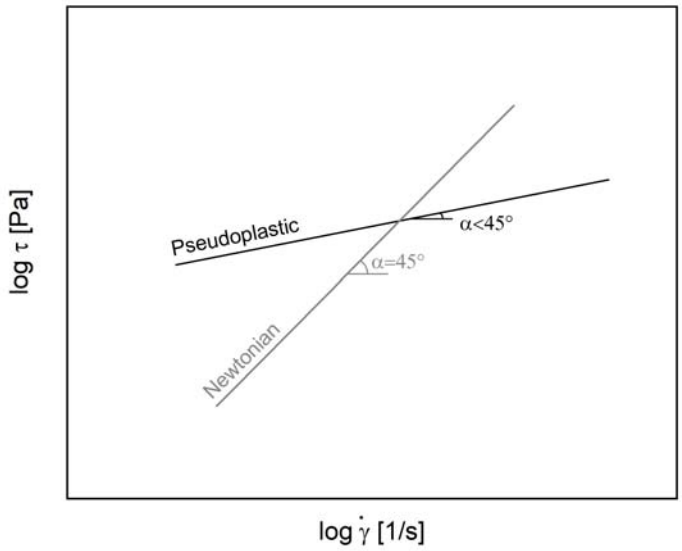

Figure 2.21: Difference between a shear pseudoplastic (shear thinning) and a newtonian behavior (oversimplified scheme).

2.4.1 *Rheology measurements*

The rheological behavior of the inks was measured by MCR 302 viscometer (Anton Paar Germany GmbH, Ostfildern, Germany), 2.2.2, at 20°C in a confined space.

The rheometer is turned on at least 1 h before starting the measurement. Then, the plate-plate measuring system consisting of an upper profiled plate and a lower sandblasted plate is positioned. After initialization, the temperature was set equal to 20°C and the gap height between the upper and lower plate was adjusted to 1 mm. Then, the ink is positioned upon the lower plate. The measurement chamber containing the plate-plate system was filled with isopropanol and then closed. This will allow to carry out the experiment in an IPA saturated atmosphere without drying the ink.

To determine the shear rate dependent viscosity, $\eta(\dot{\gamma})$, the shear rate, $\dot{\gamma}$ was varied in a range between 1 s^{-1} and 200 s^{-1}.

Plotting the shear stress, τ, against the shear rate, $\eta(\dot{\gamma})$, it is possible to obtain curves similar to those in fig. 2.21. In general, in fact, a liquid behaves following a power law equation that correlates shear stress and shear rate:

$$\tau = K\,\dot{\gamma}^{n} + \tau_0 \tag{2.2}$$

where:

- n is called *flow behavior index* [dimensionless];
- K is called *flow consistency index* [Pa s^n];
- τ_0 is the yield stress, if present [Pa].

In particular, n is equal to 1 for a Newtonian fluid leading to a linear correlation between shear stress and shear rate. On the other hand, $0<n<1$ for a pseudoplastic (or shear thinning) fluid and $n>1$ for a dilatant fluid (or shear thickening), giving a non-linear correlation between shear stress and shear rate. Eq. 2.2 can be linearized by switching to the logarithmic scale. Therefore, considering for simplicity a liquid without a yield point τ_0, eq. 2.2 will become:

$$\log \tau = n \, log\dot{\gamma} + logK \tag{2.3}$$

It is now clear to see that n is nothing more than the slope of this straight line on a logarithmic scale. For a Newtonian fluid, n is equal to 1, leading to an α angle, in fig. 2.21 equal to 45°. If the liquid has a shear thinning behavior, i.e. $0<n<1$, its straight line on a logarithmic scale will define an $\alpha<45°$, fig. 2.21. If the fluid is shear thickening, $\alpha>45°$. Therefore, the *flow behavior index* can also be found knowing α:

$$n = \tan \alpha \tag{2.4}$$

The yield stress, τ_0, the storage modulus, G', and the loss modulus, G'', were measured by amplitude test under controlled IPA atmosphere. This is divided into three step:

- first step: 16 measurement points with gamma amplitude of 100% at 1 Hz at 20°C (measurement time of 15 s);
- second step: the ink is left to rest waiting 1 h at 20°C;
- third step: 81 measurement points ramping the strain logarithmically from 0.001% to 100% at 1 Hz frequency at 20°C.

2.4.2 *Percentage linear shrinkage*

Comparing the length of a dried printed filament before and after pyrolysis, it is possible to evaluate a quantity called *linear shrinkage*. This number, usually expressed in percentage, allows quantifying the geometry difference between a component before and after a certain heat treatment. In particular, *percentage linear shrinkage* is the decrease in one dimension, expressed as a percentage of the original starting dimension. Typically, a low linear shrinkage is desired because it indicates that the geometry will not undergo evident variations after the

heat treatment.

Percentage linear shrinkage is defined as follow:

$$\Delta L = \left(\frac{l_0 - l_f}{l_0} \right) \times 100 \tag{2.5}$$

where:

- l_0 is the initial length of the filament after drying [mm];
- l_f is the final length of the filament after pyrolysis in [mm];

The aforementioned lengths, $l_0$and l_f, were manually measured using a digital caliper.

2.4.3 *Apparent (or skeletal) density*

Given a printed scaffold, apparent or skeletal density is defined as the density of the structure without taking into account any open porosity, but only of the material itself and eventually closed porosity.

The term *open porosity* refers to the volume occupied by totally interconnected voids, i.e. when the solid phase is distributed along the edges of empty polyhedric structures (*cells*) [79]. In the case of *closed porosity*, the solid phase is distributed also along the faces.

The apparent (or skeletal) density, ρ_a, is calculated using pycnometer measurements, 2.2.6. The operator is required to enter the mass of the sample of which the helium pycnometer will calculate the apparent volume including any closed porosity, V_a. The output, apparent (or skeletal) density, is calculated using the following equation:

$$\rho_a = \frac{m}{V_a} \tag{2.6}$$

with

$$V_a = V_{solid} + V_{closed} \tag{2.7}$$

where:

- ρ_a is the apparent (or skeletal) density [g/cm^3];
- m is the sample mass [g];
- V_a is the apparent (or skeletal) volume excluding any open porosity i.e. the volume of the solid including eventual closed porosity [cm^3];
- V_{solid} (or V_t, true volume) is the volume occupied by the solid, excluding any eventual closed porosity [cm^3];
- V_{closed} is the volume of the closed porosity [cm^3].

2.4.4 *Geometrical (or bulk) density*

Geometrical (or bulk) density is evaluated approximating the volume of the sample to a parallelepiped by measuring the height, width and thickness of the sample using a digital caliper. This approximation operation is described by fig. 2.22: fig. 2.22 (a) shows the scaffold with its real geometry while the black box in fig. 2.22 (b) represent the parallelepiped approximation. Therefore, the volume in 2.22 (a) represents the so-called apparent (or skeletal) volume, V_a, while the black box in fig. 2.22 (b) represents the so-called geometrical (or bulk) volume, V_g.

After weighing and measuring the sample it is therefore possible to calculate the geometric density, ρ_g, using the following equation:

$$\rho_g = \frac{m}{V_g} \tag{2.8}$$

with

$$V_g = V_{open} + V_{solid} + V_{closed} = V_{open} + V_a \tag{2.9}$$

where:

- ρ_g is the geometrical (or bulk) density [g/cm^3];
- m is the sample mass [g];
- V_g is the geometrical (or bulk) volume i.e. including both open and closed porosity [cm^3];
- V_{open} is the volume of the open porosity [cm^3];
- V_{solid} (or V_t, true volume) is the volume occupied by the solid, excluding any eventual closed porosity [cm^3];
- V_{closed} is the volume of the closed porosity [cm^3].

2.4.5 *True density*

True density is the real density of the solid part, excluding both open and closed porosity. In order to evaluate this quantity using the helium pycnometer, 2.2.6, it is necessary to eliminate any closed porosity (open porosity is already not considered by the instrument). This is obtained by finely grinding one or more identical specimens to "open" the porosities that were previously closed.

The powder is then weighed and inserted into the pycnometer which will calculate its volume of solid. True density can, therefore, be calculated with the following equation:

$$\rho_t = \frac{m_{powder}}{V_{solid}} \tag{2.10}$$

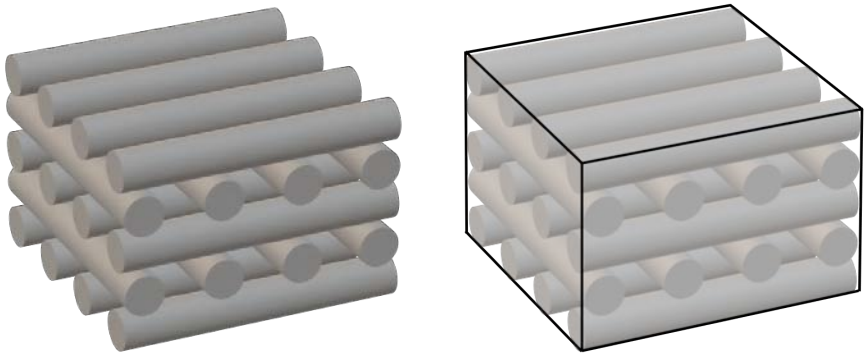

(a) *Apparent (or skeletal) volume volume.*

(b) *Parallelepiped approximation volume (geometrical or bulk volume).*

Figure 2.22: Volume approximation to a parallelepiped for geometrical density measurement.

where:

- ρ_t is the true density [g/cm^3];
- m_{powder} is the mass of the inserted powder [g];
- V_{solid} (or V_t, true volume) is the true volume (volume of the powder) i.e. volume of the solid part excluding any open or closed porosity [cm^3].

2.4.6 *Porosity*

Using the quantities in the previous sections (2.4.3, 2.4.4, 2.4.5), it is possible to evaluate the porosity of the 3D printed scaffolds. As briefly explained in sec. 2.4.3 there are two different types of porosity: open or interconnected porosity and closed porosity.

Open porosity, P_{open}, is defined as the ratio between the volume of open pores, V_{open} and the geometrical (or bulk) volume, V_g:

$$P_{open}[\%] = \left(\frac{V_{open}}{V_g}\right) \times 100 \tag{2.11}$$

and considering that, from eq. 2.9

$$V_{open} = V_g - V_a$$

eq. 2.11 can be ri-elaborated leading to eq. 2.12.

$$P_{open}[\%] = \left(\frac{V_g - V_a}{V_g}\right) \times 100 = \left(1 - \frac{V_a}{V_g}\right) \times 100 \tag{2.12}$$

Then, volumes V_a and V_g in eq. 2.12 can be replaced by their corresponding mass to density ratio (respectively eq. 2.6 and 2.8), leading to the final eq. 2.13 for porosity evaluation.

$$P_{open}[\%] = \left(1 - \frac{m\,\rho_g}{\rho_a\,m}\right) \times 100 = \left(1 - \frac{\rho_g}{\rho_a}\right) \times 100 \tag{2.13}$$

Closed porosity, P_{closed}, is defined as the ratio between the volume of closed pores, V_{closed}, and the geometrical (or bulk) volume, V_g:

$$P_{closed}[\%] = \left(\frac{V_{closed}}{V_g}\right) \times 100 \tag{2.14}$$

The closed porosity is obtainable by firstly defining a new quantity called *total porosity*, P_{tot}, which includes both open and closed porosity, and calculable by the following equation (eq. 2.15).

$$P_{tot}[\%] = \left(\frac{V_{tot}}{V_g}\right) \times 100 \tag{2.15}$$

where V_{tot} is the total volume of the pores including both open and closed porosity. Now, considering that the total amount of pores can be written as

$$V_{tot} = V_{open} + V_{closed}$$

with

$$V_{open} = V_g - V_a \qquad \text{and} \qquad V_{closed} = V_a - V_{solid}$$

where V_a is the apparent (or skeletal) volume and V_{solid} is the true volume of the solid part (2.4.5). The total volume of the pores, V_{tot}, can then be reformulated as

$$V_{tot} = V_g - V_{solid} \tag{2.16}$$

Consequently, combining 2.16 and 2.15, the following equation, 2.17, can be obtained.

$$P_{tot}[\%] = \left(1 - \frac{V_{solid}}{V_g}\right) \times 100 \tag{2.17}$$

Therefore, volumes V_g and V_{solid} in eq. 2.17 can be replaced by their corresponding mass to density ratio (respectively eq. 2.6 and 2.10) leading to:

$$P_{tot}[\%] = \left(1 - \frac{\rho_g}{\rho_t}\right) \times 100 \tag{2.18}$$

Finally, percentage closed porosity, P_{closed}, can be calculated by subtracting from the total porosity, P_{tot}, the open porosity, P_{open}.

$$P_{closed}[\%] = P_{tot}[\%] - P_{open}[\%] \tag{2.19}$$

As can be seen by comparing equations 2.13 and 2.18, when the values of apparent (or skeletal) density, ρ_a, coincides with the value of true density, ρ_t, the sample does not present any closed porosity and P_{tot} is equal to P_{open} i.e. only open porosity is present.

2.4.7 *Mechanical tests*

The weak point of any ceramic materials is their brittleness that makes them difficult to use in structural applications due to the poor reliability of mechanical tests data. This is especially true for tensile behavior, that is why the uniaxial tensile test is often not reliable leading to very scattered results. In addition, uniaxial tensile tests of ceramics, commonly used and reliable for metallic and plastic materials, have practical problems of preparation (alignment) and fixing of the specimen. Indeed, the formation of a small crack while fixing the specimen to the testing machine is sufficient to distort the result of the mechanical test.

For all these reasons, typically, ceramic materials are used in structural applications where they are subjected to compression or bending loads, avoiding purely uniaxial tensile loads. Furthermore, compression loads correspond to the actual load (bodyweight) to which the studied scaffolds are subjected once grafted into the human bone.

Consequently, uniaxial compression tests on the printed scaffolds (2.3.3.1 and 2.3.3.2) and bending tests on single filaments were carried out using the already presented machines, 2.2.7.

These tests are described in the following pages.

2.4.8 *Compression test*

Compression tests were carried out using both the Instron universal testing machines, 2.2.7, during the periods spent at the University of Padua and Friedrich-Alexander-Universität Erlangen-Nürnberg.

Samples printed at the University of Padua are firstly cut into smaller 9x9x5 mm^3 scaffolds removing all the edges and exposing the actual scaffold, fig. 2.23, while each scaffold printed at Friedrich-Alexander-Universität Erlangen-Nürnberg is cut into four 9x9x5 mm^3 samples after removing the edges, fig. 2.23 (b).

Sample faces are then smoothed using an 18 µm abrasive paper to make them flat and parallel.

Then the samples are weighed using a digital balance and all the dimensions are measured using a digital caliper to asses density and porosity measurements before breaking them.

The specimens are then positioned into the Instron universal testing machine. Two thin sheets of rubber were placed on the top and bottom of the specimen. These rubber pads were used to ensure a uniform distribution of the applied load onto the sample and avoid any stress intensification phenomenon due to a badly polished or not perfectly

flat specimen [80–85].

Both Instron, 2.2.7, work at imposed displacement that was set equal to 0.5 mm/min for all the tested specimens. A 5000 N load cell was used for all compression tests.

After starting the test, it will be possible to see the real-time load against time curve measured by the machine. The failure stress can finally be calculated using the eq. 2.20.

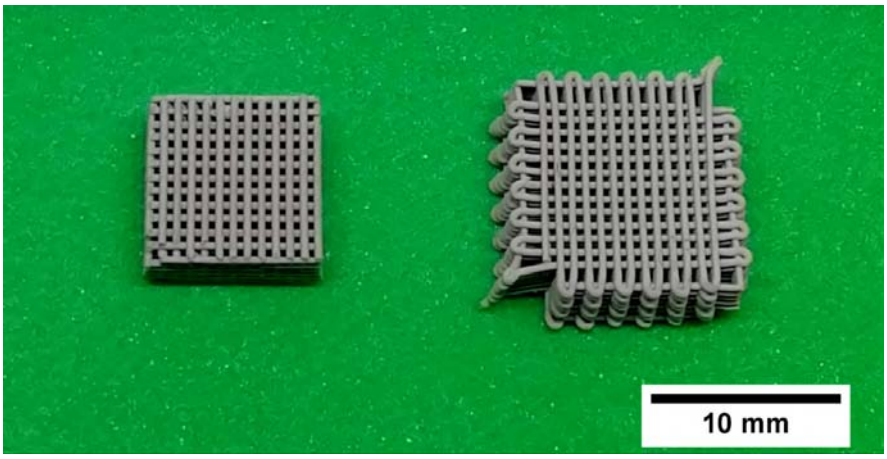

(a) *Sample after (left) and before (right) removing the edges. Printed at University of Padua using ink-1 (tab. 2.4) and 0.016 inches (0.4064 mm nozzle).*

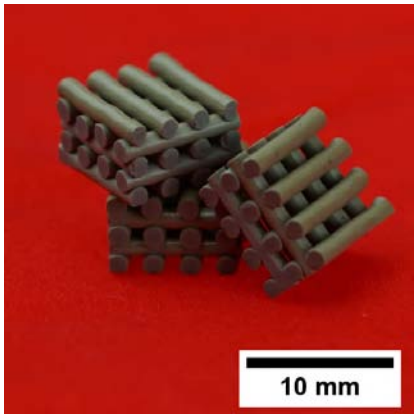

(b) *Three of the four samples obtained from the scaffold in fig. (c) after removing the edges and cutting. Printed at University of Friedrich-Alexander-Universität Erlangen-Nürnberg using ink-1* (tab. 2.5) and 1.5 mm circular cross-section nozzle.*

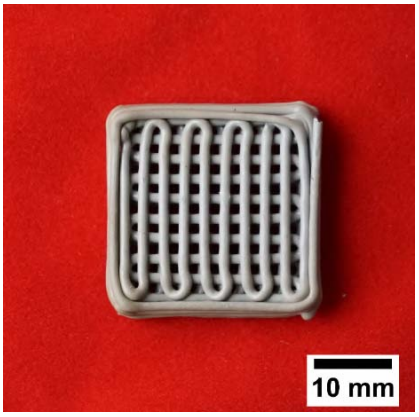

(c) *Sample before removing the edges and cutting. Printed at University of Friedrich-Alexander-Universität Erlangen-Nürnberg using ink-1* (tab. 2.5) and 1.5 mm circular cross-section nozzle.*

Figure 2.23: 9x9x5 mm^3 samples for compression tests.

$$\sigma_{comp,f} = \frac{F_{failure}}{A} \tag{2.20}$$

where:

- $\sigma_{comp,f}$ is the compressive stress at the failure point [MPa];
- $F_{failure}$ is the compressive load at the failure point [N];
- A is the resistant area [mm²].

In this thesis work, the term *"failure point"* means the first clearly distinguishable peak visible in the load-time (or stress-strain) curve, even if the scaffold is still able to bear additional loads. Finally, the term *"resistant area"*, A, is referred to the area of the specimen faces where the load acts i.e. by approximating them to squares even if their area is different from the real contact area.

From the load-time curve, it is possible to derive the stress-strain curve. The stress is calculated with eq. 2.20 while, knowing the time, t, the crosshead speed, v, and the initial height of the specimen, h_0 it is possible to calculate the strain, ϵ, using the following equation:

$$\epsilon(t) = \frac{h(t) - h_0}{h_0} = \frac{v\ (t - t_0)}{h_0} \tag{2.21}$$

where:

- $\epsilon(t)$ is the time dependent strain [dimensionless];
- h_0 is the initial height of the specimen [mm];
- $h(t)$ is the time dependent height of the specimen [mm];
- v is the crosshead speed [mm/s];
- t is the time at which the strain is calculated [s];
- t_0 is the time when the samples start to be compressed [s]. This time is zero if the compressive test starts exactly when the Instron top plate is in contact with the specimen.

2.4.9 *Filament bending test*

The bending strength of ceramic materials is usually measured by four-point bending. The specimen is placed on two supports, defining a distance called *support span*, while the load is applied through two bars whose distance is named *load span*. All the material between the two load bars is subjected to the maximum bending moment, M_{max}, as shown in fig. 2.24.

This setup is preferable to a three-point bending test, in which the load is applied through one single bar and only the material just below it is subjected to the maximum bending moment. In fact, the failure will take place in correspondence with present defects: during a four-point bending test, the area subjected to the maximum bending moment is higher and it is more probable to find defects. Consequently, compared to a three-point test, the statistical dispersion and the bending strength will be lower.

The filament is positioned on the supports as shown in fig. 2.13. The load is applied by the two loading bars which travel vertically with a crosshead speed equal to 0.5 mm/min. A 500 N load cell was used for all the filament bending tests. The maximum bending moment between the two load bars is equal to:

$$M_{max} = \frac{F\ (S - L)}{4} \tag{2.22}$$

where M_{max} is the maximum bending moment [N mm], F is the applied load [N] and S is the support span distance [mm].

Combining eq. 2.22 with Navier's equation, considering a square cross-section, it is possible to obtain:

$$\sigma_{flex,f} = \frac{M_{max}\ y_{max}}{J} = \frac{3}{2}\frac{F_{failure}(S - L)}{B\ W^2} \tag{2.23}$$

where, for a square cross-section filament:

- $\sigma_{flex,f}$ is the flexural stress at the failure point [MPa];
- M_{max} is the maximum bending moment [N mm];
- y_{max} is the maximum distance from neutral axis, equal to $W/2$ [mm];
- J is the moment of inertia of the square cross-section, equal to $(B\ W^3)/12$ [mm^4];
- $F_{failure}$ is the bending load at the failure point [N];
- W and B are the thickness and width of the square beam respectively [mm];
- L is the load span distance [mm];
- S is the support span distance [mm].

For a circular cross-section filament it is sufficient to update the moment of inertia obtaining the following equation:

$$\sigma_{flex,f} = \frac{8}{\pi}\frac{F_{failure}\ (S - L)}{D^3} \tag{2.24}$$

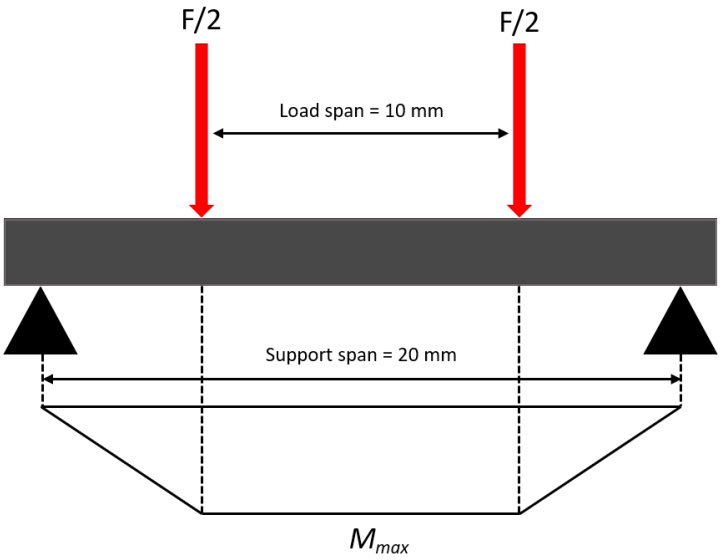

Figure 2.24: Four point bending test scheme and bending moment graph.

where D is the filament diameter [mm].

All the bending test were performed with the setup in fig. 2.24, where S=20 mm and L=10 mm.

2.4.10 *XRD analysis*

XRD measurements, sec. 2.2.5, were performed in order to asses the crystalline phase composition of the printed scaffold. The material is ground very finely using a manual mortar. Then, the obtained powder is transferred to a special adapter trying to obtain a surface as flat and regular as possible. Then, as cited in 2.2.5, the potential difference and the current intensity were set respectively equal to 40 kV and 40 mA. The 2θ angle was varied between 10° to 70°, with a 0.05° step size every 2 seconds. Crystalline phase identification was performed using Match!, a software package (Crystal Impact GbR, Bonn, Germany) supported by ICDD PDF-2 Powder Diffraction File (International Center for Diffraction Data, Newtown Square, PA, USA) as the reference database.

3

RESULTS AND DISCUSSION

After presenting the materials (2.1) and instruments (2.2) used, the experimental procedure (2.3) and the characterization methods (2.4), this chapter means to show and discuss the results obtained during this thesis work.

The chapter will explain the strategies used explaining their reasons. Firstly, issues related to the printing process, inks preparation and choice will be discussed. Then, the characterization of the printed scaffolds from a microstructural (integrity, phases) and macrostructural (porosity) point of view will be presented followed by their mechanical properties (compressive and flexural strength).

3.1 INK PROPERTIES AND PRINTING PROCESS ISSUES

As already reported, 2.3.3, the printing process was divided into two part:

- Printing using the DIW printer, 2.3.3.1, equipped with a 0.016 inches (0.4064 mm) nozzle at the University of Padua;
- Printing using the robocasting machine, 2.3.3.2, equipped with the different nozzle geometries in tab. 2.6 at Friedrich-Alexander-Universität Erlangen-Nürnberg.

The current section means to explain the issues linked to the printing process with a special focus on inks behaviour.

Firstly, it is necessary to explain why the compositions of the inks are those of tab. 2.4 and 2.5. Then, a discussion, based on printing attempts and rheological measurements, will explain the reasons for preferring one ink over another for each specific situation.

3.1.1 *Reasons for ink compositions*

As already written, 1.1, the aim of this thesis work is to fabricate bifunctional scaffolds, capable of both stimulate new tissue growth and kill tumor cells by exploiting the photothermal effect of the carbon present in the structure, 1.4.

The first function, i.e. biocompatibility and bioactivity, is due to the presence of $CaCO_3$. This is the reason why all the prepared inks,

tab. 2.4 and 2.5, contain about 65-70%wt of calcium carbonate after pyrolysis.

The second function, that we can define therapeutic, is assigned to the pre-ceramic polymer and carbon fibers, where present. Therefore, the pre-ceramic polymer performs two functions: supplying carbon to exploit its photothermal effect and acting as a matrix for calcite. However, pyrolysis in air would cause the disappearance of the carbon present in the silicone through the production of CO_2 by reaction with oxygen leading to a pure silica matrix, SiO_2. This is the reason why the pyrolysis is carried out under an inert atmosphere i.e. nitrogen. In that way, the final ceramics will be composed by a silica-carbon nanocomposite, embedding unreacted calcite particles [40, 43].

In particular, Silres MK® after pyrolysis lead to a ceramic with atomic proportions 31.6%Si – 48.1%O – 20.2%C i.e. $Si_3O_{4.6}C_{1.92}$ that means 2.3 SiO_2, 0.7 SiC and 1.22 C.
On the other hand, Silres H44® resin, corresponds to 18.7%Si – 28.7%O – 52.6%C after pyrolysis i.e. $Si_3O_{4.6}C_{8.45}$ that means 2.3 SiO_2, 0.7 SiC and 7.75 C [86].

Therefore, in both cases, the final matrix should be composed of SiOC, where Si is partially bonded to oxygen and carbon, with the presence of a "free" carbon phase. However, recent works by Fiocco *et al.* [42] and Elsayed *et al.* show no traces of Si-C bond, i.e. all the carbon deriving from the pre-ceramic polymer decomposition is present as a separate (nano-sized) phase, enhancing silica formation. The amount of this pyrolytic carbon phase is higher using Silres H44®, which should then exhibit a greater photothermal effect than Silres MK®.

Consequently, considering to keep the percentage of calcite high, the formulations in table 2.4 and ink-2*, tab. 2.5, are preferable because all the non-calcite phase is derived from decomposition products of the pre-ceramic polymer, including pyrolytic carbon clusters and carbon fibers (if present), which can be exploited as photothermal agents.

Therefore, if fumed silica is added to the mixture, in order to maintain an elevated weight percent of $CaCO_3$, it is necessary to slightly decrease the quantity of pre-ceramic polymer: this is the case of ink-1* where the quantities of Silres MK® and fumed silica were balanced to obtain a final ceramic matrix consisting on 10% of SiO_2 from fumed silica and on 90% from silicone resin decomposition products ($Si_3O_{4.6}C_{1.92}$). If the amount of fumed silica added is very high, as well as reducing the photothermal potential, it will reduce the amount of resin that can embed the calcite particles, thus reducing scaffold integrity. Its quantity in ink-1*, tab. 2.5, was considered a good trade-off

between printability and final composition.

The compositions of the inks after pyrolysis are shown in tab. 3.1. Finally, although it is preferable to print using the formulations in table 2.4 and ink-2*, tab. 2.5, in some cases, it is necessary to add fumed silica to modify the rheology of the ink, sec. 1.2.4. Therefore, the discussion of rheology and the cases when its modification is required will be the main topic of the next pages.

Table 3.1: Composition of the inks after pyrolysis.

Name	$CaCO_3$ [%wt]	[a] $Si_3O_{4.6}C_{1.92}$ [%wt]	[b] $Si_3O_{4.6}C_{8.45}$ [%wt]	[c] C [%wt]	[d] SiO_2 [%wt]
Ink-1	70	30			
Ink-2	70		30		
Ink-3	65	25		10	
Ink-4	65		25	10	
Ink-1*	70	27			3
Ink-2*	67	28		5	

[a] from Silres MK® [b] from Silres H44® [c] from carbon fibers [d] from fumed silica.

3.1.2 *Rheology considerations and printing issues*

As already explained, during this thesis work, the printing step was performed in two different moments and places.

Firstly, at the University of Padua, direct ink writing of the inks in tab. 2.4 was performed using the the DELTA WASP 20x40 TURBO 2 printer, 2.2.3.1. The first part of this section is then dedicated to that, 3.1.2.1.

After demonstrating the printability and optimizing the process with inks in tab. 2.4, the work was continued at the Friedrich-Alexander-Universität Erlangen-Nürnberg using the robocaster, 2.2.3.2. The aim, in this case, is to compare different filament cross-sections, tab. 2.6. Therefore, it was decided to focus on only one pre-ceramic polymer, in particular Silres MK®. Despite Silres H44® is typically easier to print and has a higher carbon yield than Silres MK®, the latter was chosen for two main reasons: it was available in larger quantities and it is a better known pre-ceramic polymer. Furthermore, the comparison between different filament cross-sections should be independent of the pre-ceramic resin but it should depend only on the geometry.

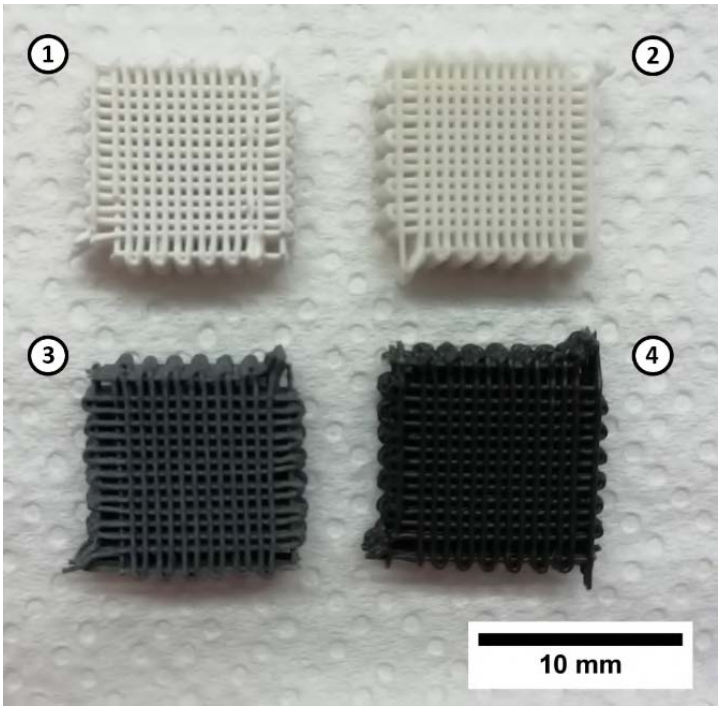

Figure 3.1: Scaffolds printed at University of Padua using a conical 0.016 inches (0.4064 mm) nozzle. Top left ①: ink-1. Top right ②: ink-2. Bottom left ③: ink-3. Bottom right ④: ink-4.

Therefore, this section will address issues an rheology consideration regarding printing using 0.3 mm and 0.5 mm circular cross-section nozzles, 3.1.2.2, 1.5 mm circular and square cross-section nozzles, 3.1.2.3, hollow filaments scaffolds, 3.1.2.4, coextruded filaments scaffolds, 3.1.2.5.

3.1.2.1 *Printing with 0.016 inches (0.4064 mm) nozzle*

As explained, 3.1.1, formulations in table 2.4 and ink-2*, tab. 2.5, are preferable. That is the reason why only the inks in tab. 2.4 were used during the time spent within the laboratories at the University of Padua using the DELTA WASP 20x40 TURBO 2 printer, 2.2.3.1. Some printed scaffolds (one per typology) are visible in fig. 3.1.

Fig. 3.2 shows optical microscopy (2.2.4.1) images of the same scaffolds with higher magnification. As it is possible to see, the printing quality is very high, with only a few slight filament distortions. All the scaffolds were printed using pressure between 2-3 bar, adjusting the print speed manually when necessary.
In particular, fig. 3.2 (c) and (d) show scaffolds which will contain 10%wt of carbon fibers after pyrolysis i.e. obtained by printing with ink-2 and ink-4 (3.1). These inks are more difficult to print than ink-1 and ink-2: the addition of a large quantity of carbon fibers can create filament irregularities, due to the fact that during the extrusion it

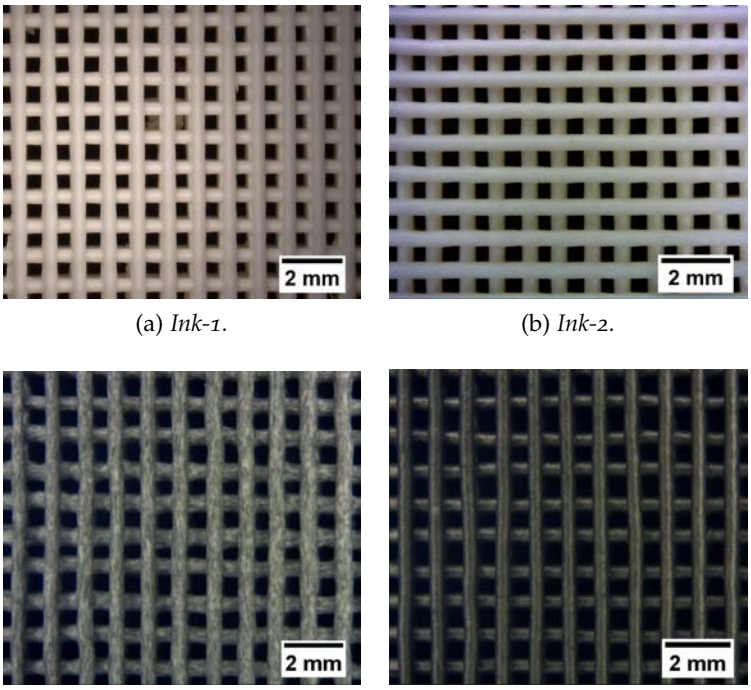

(a) *Ink-1.* (b) *Ink-2.*

(c) *Ink-3.* (d) *Ink-4.*

Figure 3.2: Optical microscopy images (2.2.4.1) of scaffolds printed at University of Padua using a conical 0.016 inches (0.4064 mm) nozzle.

can happen that groups of fibers agglomerate forming packets that locally modify the rheology of the ink. This effect gradually increases with a higher amount of fibers and/or extruding with smaller nozzle diameters. This also leads to a narrow printing pressure window. In fact when printing using ink-1 or ink-3 the pressure can be changed between 2-3 bar without evident filament instability phenomena. Contrariwise, using ink-2 or ink-4, pressure changes can suddenly cause instability and filament zigzagging as shown in fig. 2.15 (b) of the previous chapter (chapter 2, sec. 2.3.3.1). Therefore, the possibility to change the speed instead of the pressure is absolutely helpful.

Furthermore, after pyrolysis and at the moment of performing compression tests (3.3), it was noticed that the scaffolds printed with ink-2 encountered joint problems between the various layers, i.e. an easy detachment of some of them during handling. This could be caused by three consequences of using a high amount of carbon fibers:

- the Silres MK® resin is not able to properly embed both calcite and all the fibers, leaving partially uncovered some of them, especially those close to the nozzle wall;
- as visible in fig. 3.3, as the ink is pushed through a thin nozzle, shear stresses able to rotate the carbon fibers and orient them along the printing direction are generated at the nozzle tip [87].

This alignment, visible in fig. 3.2 (c), is proportional to shear stress inside the nozzle. It means that close to the nozzle wall, where the shear stress is maximum, 3.3 (b), the fibers are more oriented along the extrusion direction. The greater degree of orientation along the most external circular crown leads to an increase in the probability of exposing fibers externally, leaving them partially uncovered;

- filaments containing carbon fibers are stiffer than filament without fibers.

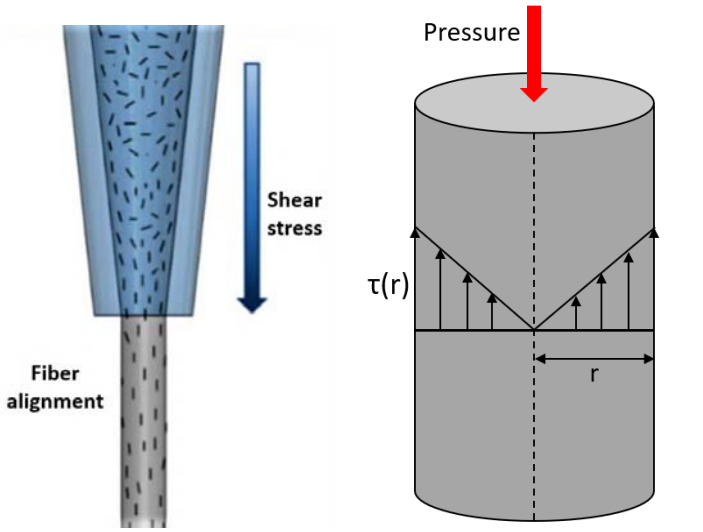

(a) *Nozzle tip [87].*

(b) *Shear stress distribution inside the nozzle.*

Figure 3.3: Fibers alignment during extrusion.

Consequently, by combining the first two aspects (embedding and alignment), fibers extruded in the outermost part (wall) of the nozzle, could be only partially covered by the resin and when two layers are overlapped, there is a high probability to have a fiber-fiber contact in random points within the joint area, instead of fiber-resin or resin-resin. Then, considering that the fiber-fiber contact will not generate any adhesion or "welding", the joint between two filaments can result compromised or weakened. Obviously, increasing the amount of carbon fibers in the ink, the probability to have a fiber-fiber contact in the joint area is higher. Furthermore, the improved filament stiffness (third aspect) can prevent the different layers from properly lying on each other, not allowing their small interpenetration, necessary for a good joint.

For these reasons, it was decided to halve the quantity of carbon fibers in the future preparations (at the Friedrich-Alexander-

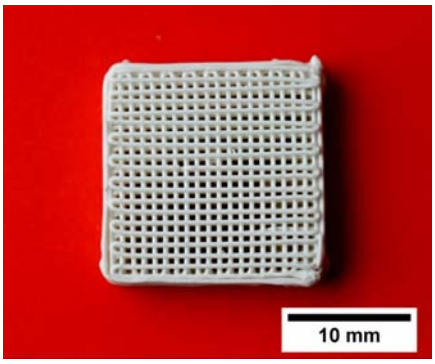

(a) *Ink-1 green scaffold printed with a 0.3 mm nozzle.*

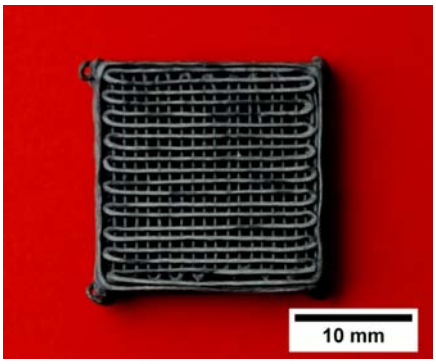

(b) *Ink-2* green scaffold printed with a 0.5 mm nozzle.*

Figure 3.4: Scaffolds printed with ink-1 and ink-2* after drying.

Universität Erlangen-Nürnberg), preparing ink-2* instead of ink-2.

This problem is less evident using ink-4, suggesting that the embedding properties of Silres H44® are better that Silres MK®. Another possibility, it could be that the ink-4 requires a greater quantity of pre-ceramic polymer during the preparation, because of the lower ceramic yield of Silres H44® after pyrolysis. This higher quantity of resin could improve fiber embedding during printing, maintaining a beneficial effect even after pyrolysis.

3.1.2.2 *Printing with 0.3 mm and 0.5 mm nozzles*

During the period spent at the Friedrich-Alexander-Universität Erlangen-Nürnberg, the robocaster, 2.2.3.2, has been firstly used to extrude thin filaments.

Ink-1 and ink-2*, tab. 2.6, were extruded using nozzles with a diameter of 0.3 mm and 0.5 mm, fig. 2.8 (a). The printed scaffolds, shown in fig. 3.4, are absolutely appreciable, with perfectly spaced and regular filaments. The ink-1 demonstrated to be suitable for printing with both nozzles mentioned, i.e. 0.3 and 0.5 mm nozzles, while ink-2 results to be printable only with 0.5 nozzle or higher: this is due to the fact that a 0.3 mm diameter nozzle is too close to the length of the fibers which is about 100 µm. Consequently, especially if the fibers are not well dispersed into the ink, it is enough a small fibers agglomeration to clog the nozzle tip and then making the printing impossible.

The result, shown in fig. 3.4, was obtained changing the robocaster arm setup provided by the machine manufacturer, fig. 2.16 (a), with a custom setup, fig. 2.16 (b), that was built within the university workshop especially for these inks.

In fact, the setup provided by the company requires very high pressures for printing, close to the 6 bar safety limit, sec. 2.2.3.2. This is related to an excessive length of the feeding channel inside the metal casing, fig. 2.16 (a), that the ink must go through to reach the nozzle tip. Consequently, assuming a laminar flow of the ink inside a perfectly smooth channel, the pressure drops are intimately connected to the length of the duct (linear correlation).

$$\Delta p = p_{in} - p_{out} = 32\frac{v\ L\ \eta}{D^2} \tag{3.1}$$

where:

- Δp is the pressure drop;
- p_{in} and p_{out} are the inlet and outlet pressure;
- v is the velocity of the paste inside the channel;
- L is the cylindrical feeding channel length;
- η is the ink viscosity;
- D is the cylindrical feeding channel diameter.

This equation, 3.1, also know as Hagen-Poiseulle relation is valid for a Newtonian fluid: it would be more appropriate to use the Rabinowitsch's equation which takes into account the pseudoplastic behaviour of the fluid. However, eq. 3.1 is adequate to illustrate the problem.

Therefore, an excessive channel length can cause elevated pressure drops between the inlet and the outlet. For this reason, the setup was replaced with a custom one that halves the feeding channel length, 2.16 (b), allowing the printing with lower pressures.

3.1.2.3 *Printing with 1.5 mm nozzles*

Scaffolds printing with nozzle diameter (or side) equal to 1.5 mm was performed in order to extrude different filament cross-sections, using the inks in tab. 2.5. At first, ink-1 has been adopted giving poor results: the scaffolds exhibited shape retention problems, collapsing slowly over time, even if the amount of isopropanol is reduced to produce a more viscous ink. In light of this, the rheology of the ink was measured, 2.2.2, leading to the flow curve in light grey of fig. 3.5 and fig. 3.8.

As it is possible to see, ink-1 rheology measurement shows a low pseudoplastic behavior of the paste with a viscosity, η, that remains almost constant while varying the shear rate, $\dot{\gamma}$, fig. 3.5 and 3.8, showing a viscosity of about 450 Pa·s at very low shear rates. It was confirmed

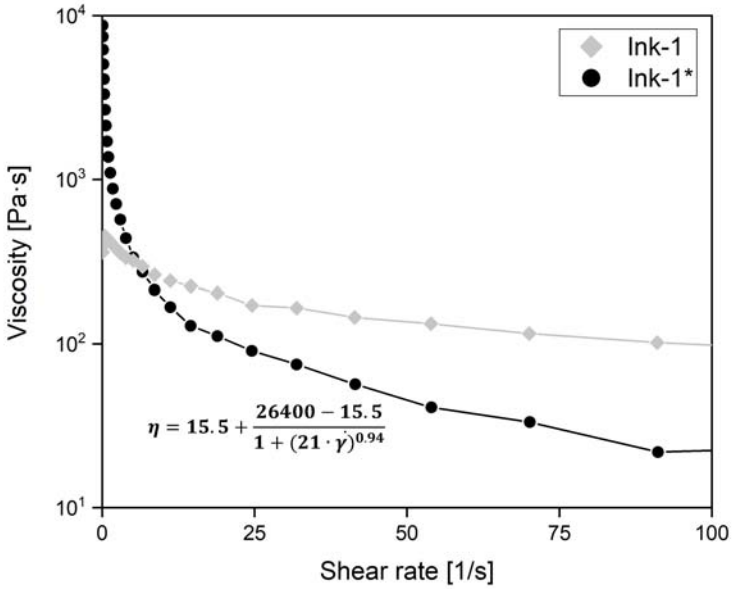

Figure 3.5: Rheology behaviours of ink-1 and ink-1*. The equation in the graph describe the Cross model fit of ink-1*.

by the calculation of the *flow behavior index*, n, by using the procedure explained in section 2.4.1, that is equal to 0.76. Furthermore, it was also tried an ink with a lower amount of isopropanol (IPA) which shows a viscosity of about 2600 Pa·s at very low shear rates, fig. 3.8 in dark grey. However, this ink requires high printing pressures close to the 6 bar limit without any evident benefits with respect to ink-1.

This shape retention problem is related to the diameter of the printed filament i.e. to the different drying behavior between a thin and a thick filament. As explained in sec. 2.3.4, when printing with 0.5 mm, or lower, nozzle diameter the just extruded filament will undergo instantaneous, albeit partial, drying, capable of allowing the material to maintain its shape despite a weakly pseudoplastic behavior. Moreover, the filament lightness will not generate loads as high as to cause the structure to collapse. On the other hand, when printing with a 1.5 mm nozzle diameter (or side), the drying right after printing is not enough to allow an adequate shape retainment. Moreover, the high weight of the filament will slowly lead to structure collapse over time.

Consequently, the composition of ink-1 has been modified by adding fumed silica which, acting as illustrated in chapter 2, sec. 1.2.4, allows to increase the pseudoplastic character of the mixture (i.e. to reduce n) and introduce a yield point. This new ink, named ink-1*, is represented in fig. 3.5 and 3.8 with a black curve. As it is possible to see, it is sufficient a small amount of fumed silica, tab. 2.5, to clearly

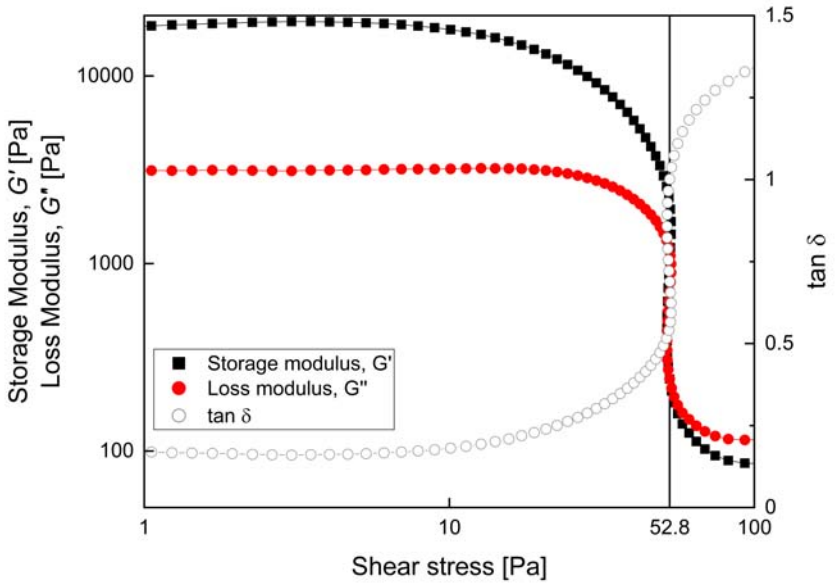

Figure 3.6: Storage and loss modulus of ink-1* showing a yield point of 52.8 Pa.

increase the low shear rates viscosity, which is equal to about 8700 Pa·s. Moreover, the ink shows a yield point of 52.8 Pa, calculated through amplitude measurements, 2.4.1. The value of n is equal to 0.14. This ink allows the extrusion of the different filaments in tab. 2.6 as shown in fig. 3.7 for a circular and square cross-section.

These two cross-sections were also printed using ink-2*. The rheology of this ink (ink-2*), fig. 3.8 in red, shows a weakly pseudoplastic behaviour up to shear rate of about 10 s^{-1}, similar to ink-1. Then the viscosity rapidly decreases because of fibers alignment within the paste. Although viscosity at very low shear rates is comparable to that of ink-1, the scaffold has proved capable of maintaining the shape, accompanied by a slight yielding. This can be attributed to the improved stiffness of the filament thanks to carbon fibers that help shape retainment. Therefore, it was decided to keep ink-2* without adding fumed silica to avoid previously explained embedding problems: adding fumed silica means also to decrease the Silres MK® to carbon fibers ratio in order to maintain high the final weight percent of calcite (3.1.1).

In conclusion, the maintenance of shape proved to be dependent on three factors:

- drying behaviour of the filament: it is strongly correlated with filament thickness. If the drying is fast, i.e. thin filaments (d<0.5 mm), the structure is able to maintain the shape thanks to two factors: increase in viscosity at the nozzle tip thanks to the fast

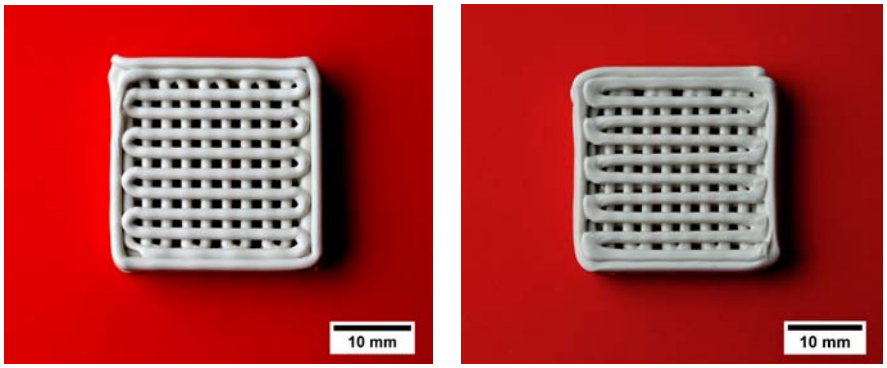

(a) *Circular cross-section.* (b) *Square cross-section.*

Figure 3.7: Circular and square cross-sections scaffolds printed with ink-1* after drying.

drying and lightness of the filament. An example is ink-1 with a nozzle diameter of 0.3-0.5 mm;

- shear thinning (or pseudoplastic) behavior: it helps shape retainment by introducing a yield point and increasing the viscosity at very low shear rates, fig. 3.6. An example is ink-1*;
- filament stiffness: the addition of fibers that align during extrusion allows the scaffold to maintain the shape even with nozzle diameters of 1.5 mm. An example is ink-2*.

The yield point in fig. 3.6 corresponds to the shear stress in which the loss modulus, G'', becomes higher than the storage modulus, G'.

3.1.2.4 *Printing of hollow filaments*

The printing of hollow filaments without using any sacrificial materials represents the most challenging part of this work. In fact, a widely used approach is the co-extrusion, in which the core material can be eliminated by successive heat treatments. For example, Fu *et al.* [75] used a carbon-based gel as core material that is oxidized and evaporate after firing in air above 1000°C, leaving ceramic filaments with a hollow cross-section. However, this approach is not possible in this specific case for two reasons. Firstly, the temperature of 1000°C would cause the decomposition and the successive reaction of calcite. Then, carbon gel decomposition would require treatment in air that would lead to the transformation of the pre-ceramic polymer into a pure SiO_2 matrix (without carbon), undermining the photothermal effect.

Therefore, the approach is to print directly hollow filaments. The nozzle used to perform the printing is shown in fig. 3.9. It consists of a circular cross-section nozzle with a diameter of 1.5 mm combined

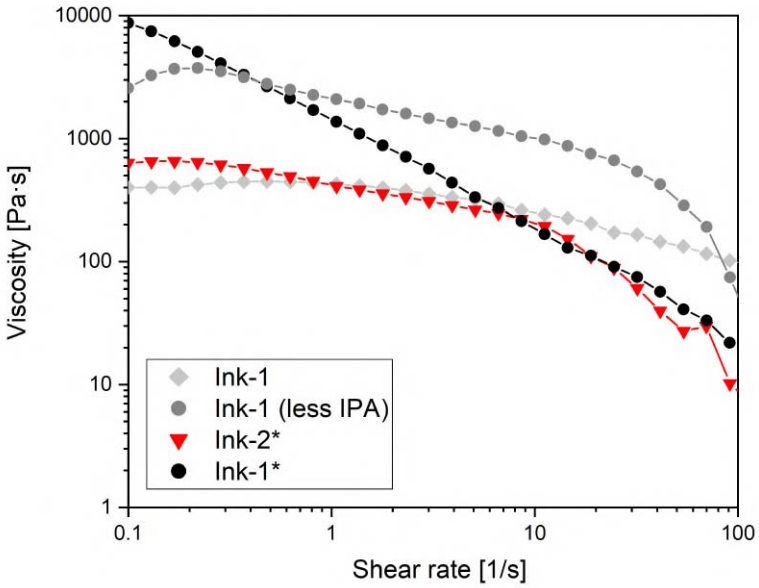

Figure 3.8: Flow curves of ink-1, ink-1* and ink-2*

with a 0.75 mm mandrel i.e. the theoretical filament wall thickness is 0.375 mm. The manufacture of hollow scaffolds presents a series of requests that must be met respecting very close tolerances.

RHEOLOGY is crucial for obtaining self-supporting filaments. First of all, it is necessary a strong pseudoplastic behaviour: the ink has to pass through the small channels of the mandrel, i.e. a liquid paste is required when pressure is applied. This is also the reason why it was impossible to use this setup for printing hollow structures using ink-2*: the presence of the fibers does not allow the paste to pass through the thin channel of the mandrel.
Then, high viscosity at low shear rates is fundamental, because even a very small structure collapse, acceptable for full cross-section filaments, can clog the hole, i.e. the filament must maintain its shape immediately after printing until pyrolysis. In summary, strong shear thinning (or pseudoplastic) behaviour is required.

FILAMENT STABILITY is another very important feature that strongly depends on the ink and on the printing pressure. In fact, the filament walls in two opposite points of the cross-section must be perfectly parallel one to the other. Otherwise, the hole will clog. Therefore, the printing pressure has to be carefully controlled in order to avoid filament instability phenomena, leading to filament zig-zagging, fig. 2.15 (b), at high pressures.

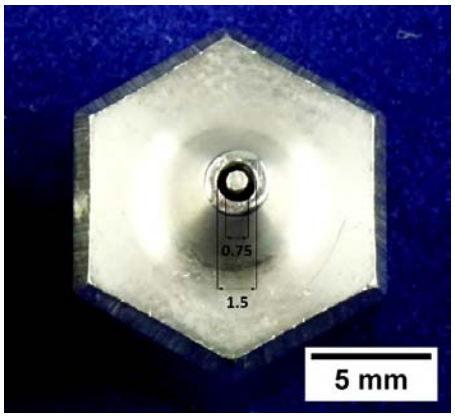

Figure 3.9: Nozzle for hollow filaments printing.

PRINTING SPEED must be in perfect harmony with the printing pressure. In fact, the nozzle forward speed has to be as close as possible to the pressure-dependent flow rate. If the ink flow rate is lower than the printing speed, the filament will stretch causing the approaching of two opposite walls of the filament. On the other hand, if the ink flow rate is higher than the printing speed, the ink will accumulate at the nozzle tip, occluding the hole. Unfortunately, as already mentioned, the robocaster, 2.2.3.2, does not allow to adjust the speed during printing, a function that would have been useful in this situation.

In addition to these three considerations, it must be kept in mind that it is impossible to know if the newly printed scaffold is *hollow* or not, but it is necessary to wait after pyrolysis and cutting. Therefore, hollow filament printing optimization could be a very time-consuming process.

After many attempts in air, printing was also performed in sunflower oil bath. This approach exhibits two main advantages:

- oil infiltration into the filament: the infiltration into the filament of an incompressible liquid can help to avoid the occlusion of the hole, favoring the support of the structure;
- density of the oil: the filament will be "lighter" when immersed into sunflower oil, i.e. structure collapse due to its own weight is reduced.

However, the last point can be misleading: if the density of the oil is too high, the filaments of two successive layers will not interpenetrate at all, preventing their welding. In the worst case, the filament will float in the oil, not even allowing printing.

3.1.2.5 *Co-extrusion*

Co-extrusion is the printing process where two inks are used simultaneously. The adopted setup is visible in chapter 2, fig. 2.17 (b). It consists of a metal cage with two ink inlets: one on the metal cage side for the *shell* material and one on its top for the *core* material.
In fact, when printing co-extruded filaments, it is important to consider that the shell material must fill the metal cage before extrusion can take place. The metal cage geometry leads to high pressure losses, both concentrated (feeding channel convergence, divergence, turns) and distributed (channel length, eq. 3.1) as regards the shell ink. That requires high inlet pressure in order to overcome this pressure loss. A first trivial solution could be to increase the shell pressure, but it must be kept in mind that the maximum operating pressure is about 6 bar, 2.2.3.2. Consequently, it is necessary to decrease a bit the viscosity of the shell ink by adding slightly more isopropanol. This expedient allows printing while maintaining safety pressures lower than 6 bar. However, adding too much IPA would lead to excessively liquid inks, unable to maintain its shape and which would slowly collapse over time. It is, therefore, necessary to find a trade-off between operating pressure and viscosity of the liquid, thus it will be optimal to print using a sufficiently high pressure but which do not exceed 6 bar.

By balancing the two pressures involved, different cross-sections can be obtained i.e. with different proportions between core and shell material. Also in this case, it is impossible to check if the scaffolds present a proper cross-section during printing and it will be necessary to wait after their pyrolysis and cutting.

After printing, the co-extruded scaffolds are aesthetically the same as the scaffolds printed using the shell ink only.

3.2 RESULTS AFTER PYROLYSIS

After printing, the scaffolds are left to dry following the procedure explained in chapter 2, sec. 2.3.4. Subsequently, they are inserted into the tubular oven, sec. 2.2.8, for pyrolysis in an inert atmosphere (N_2) following the temperature profile in fig. 2.19. Then, after natural cooling inside the furnace, the samples are taken out of the oven.

The following step is the cutting of the edges as shown in fig. 2.23: the scaffolds printed at the University of Padua are simply stripped of the supports, while scaffolds printed with a 1.5 mm nozzle at the Friedrich-Alexander-Universität Erlangen-Nürnberg are also cut into four parts using a diamond wire machine.

The scaffolds are then characterized following the procedures in chapter 2, sec. 2.4.

This section means to discuss the quality of the printed scaffolds through microscopy observations (both optical microscopy and SEM), 2.2.4, XRD measurements, 2.4.10, and linear shrinkage measurements, 2.4.2.

Physical (density and porosity) and mechanical properties (compression and bending tests) are left to the following section, 3.3.

3.2.1 *Structural integrity of the printed scaffolds*

Immediately after pyrolysis, the scaffolds are observed under an optical microscope and SEM in order to assess their consistency.

3.2.1.1 *0.016 inches (0.4064 mm) nozzle*

The scaffolds printed at the University of Padua are shown after pyrolysis in fig. 3.10. The sample before cutting the edges is shown on the left side of each image, while the sample without edges on the right.

The quality of the specimens appears not compromised by the heat treatment. However, a more thorough observation under a microscope is necessary, in particular, to detect any superficial microcracks. As it is possible to see in fig. 3.10 and 3.11, scaffolds containing Silres H44®, i.e. ink-3 and ink-4 (tab. 2.4) exhibit a darker colour due to the greater amount of carbon present.

The top layers, shown in fig. 3.11, demonstrate the high quality of the final scaffold: the filaments seems not deformed and perfectly spaced, leading to a constant and regular porosity.

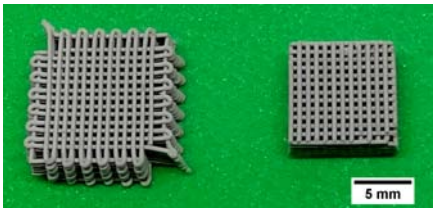

(a) *Ink-1.*

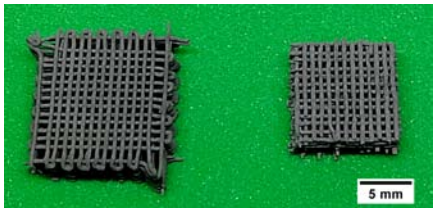

(b) *Ink-2.*

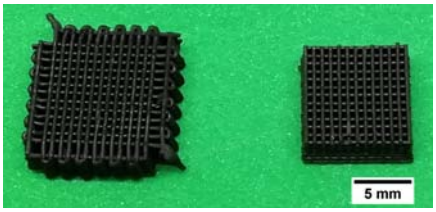

(c) *Ink-3.*

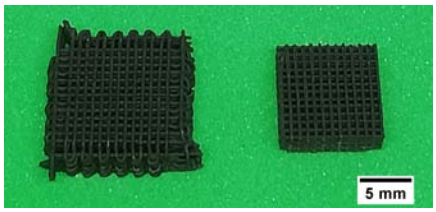

(d) *Ink-4.*

Figure 3.10: Scaffolds printed with 0.016 inches (0.4064 mm) nozzle after pyrolysis: before (left) and after (after) cutting the edges.

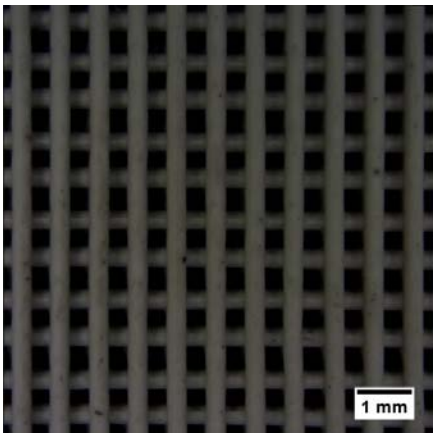

(a) *Ink-1.*

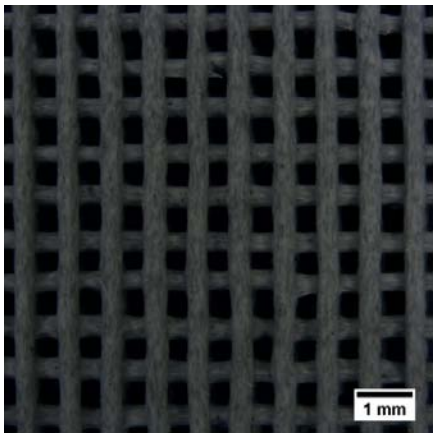

(b) *Ink-2.*

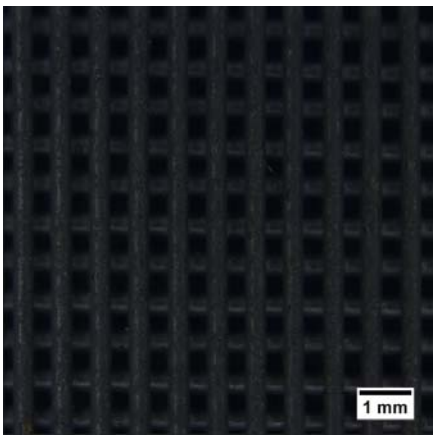

(c) *Ink-3.*

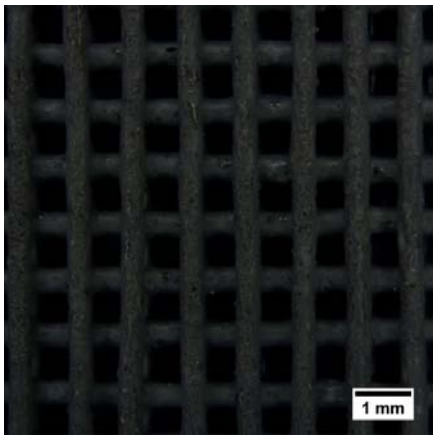

(d) *Ink-4.*

Figure 3.11: SEM images of scaffolds printed with a 0.016 inches (0.4064 mm) nozzle after pyrolysis.

The samples are then broken to expose the fracture surface that is observed with scanning electron microscopy, fig. 3.12.
Scaffolds printed using ink-1 and ink-3, fig 3.12 (a) and (b), show interesting features:

- there is a good interpenetration between the layers without any collapsing phenomena e.g. bending of the free spanning filaments. Furthermore, this interpenetration does not compromise the filament shapes, leaving them straight and with constant thickness. Therefore, the used combination of rheology and printing parameters are adequate to print this lattice structure;
- no delamination is found: the welding between different layers gives continuity to the lattice. Indeed, the joint areas cannot be distinguished from the others, thus, from a mechanical point of view, the lattice is not formed by single overlapping filaments but by a single body;
- the filament cross-sections are circular with constant diameters. Therefore the pyrolysis does not deform the geometry or cause material flow and collapsing;
- the high filler content (about 70%wt of calcite) allows a low shrinkage, i.e. the main cause of cracks.

Resuming these four points, the ink composition together with printing parameters lead to scaffolds which present a very good joint between the different layers.

Scaffolds extruded using ink-2 and ink-4 are then shown in fig. 3.12 (c)-(f). Some considerations can be made:

- scaffolds printed with ink-2 do not show good filaments interpenetration as the small contact area between two successive layers demonstrate, fig. 3.12 (c). As already explained in sec. 3.1.2, the reason can be the high amount of carbon fibers that, leading to stiffer filaments, may compromise good welding between layers. Furthermore, the amount of resin may not be enough for a proper embedding of both fibers and calcite particles. This effect, as explained (3.1.2.1), is more evident in the external part of the filament, i.e. where the welding takes place;
- scaffolds printed with ink-4 are more homogeneous than the former (ink-2), fig. 3.12 (e): their higher amount of pre-ceramic polymer, needed because of the lower ceramic yield, improves fibers and calcite particles embedding, sec. 3.1.2;
- both scaffolds present a very low quantity of micro-cracks, that are concentrated in the welding area. Ink-4 scaffolds seem to be more affected by cracks. The reason is the higher shrinkage

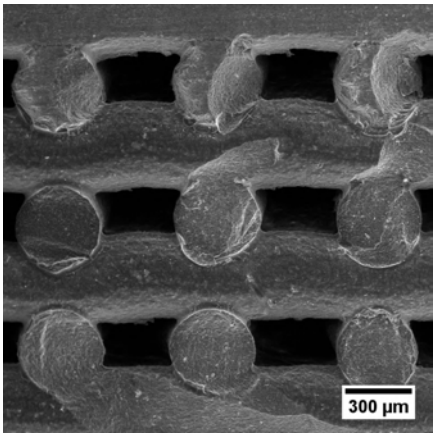

(a) *Ink-1.*

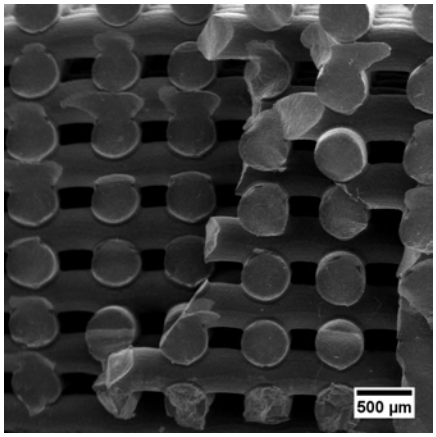

(b) *Ink-3.*

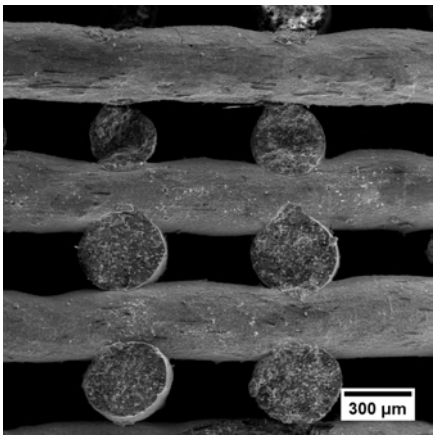

(c) *Ink-2.*

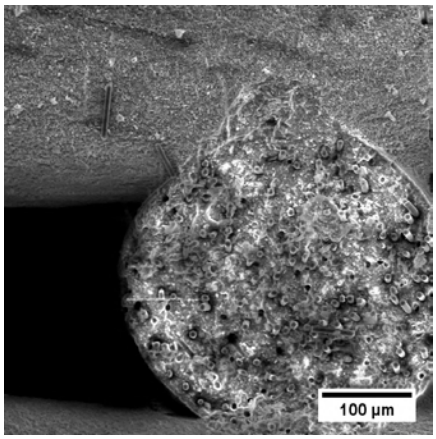

(d) *Ink-2.*

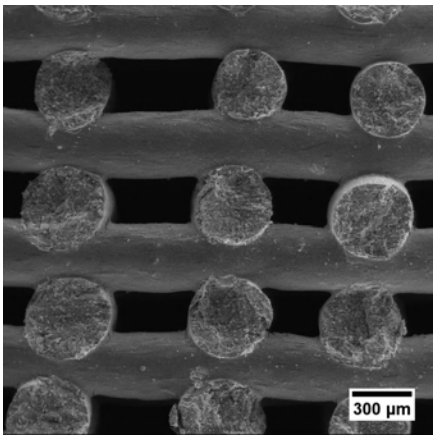

(e) *Ink-4.*

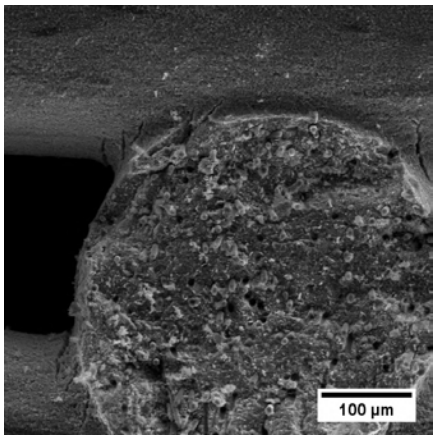

(f) *Ink-4.*

Figure 3.12: SEM images of scaffolds printed with a 0.016 inches (0.4064 mm) nozzle after pyrolysis.

with respect to ink-2 scaffolds, due to the lower ceramic yield of Silres H44® than Silres MK®. However, these cracks are very small (less than 50 µm).

Therefore, when adding carbon fibers, the lower ceramic yield of Silres H44® has two different effects: from one side, it allows a better embedding of the fillers (carbon fibers and calcite) and, from the other side, the higher shrinkage leads to microcracks in the most critical areas.

Concluding, an appreciable quality of the final scaffolds was obtained for all the four inks used during the time spent at the University of Padua. The lattices present very regular and consistent structures, ascertained by SEM observations.

The discussion of the microstructure and fiber-matrix interaction is left to a dedicate section, 3.2.2.

3.2.1.2 *1.5 mm nozzles*

The scaffolds printed at the Friedrich-Alexander-Universität Erlangen-Nürnberg consist of different filament cross-sections in order to compare their mechanical properties, tab. 2.6.

As already shown in chapter 2, sec. 2.4.8, every printed lattice is stripped of the edges and then cut into four smaller scaffolds as visible in fig. 2.23 (b) and (c).
Scaffold faces are then smoothed using 18 µm abrasive paper. All the different cross-sections are then captured using the Keyence VHX-6000 microscope (fig. 2.10) and are visible in fig. 3.13.

The first picture, fig. 3.13 (a), demonstrates the high printing quality of scaffolds printed with circular cross-sections filaments. These are absolutely regular in their shape and the good welding between successive layers is accompanied by an adequate degree of interpenetration.

The second picture, fig. 3.13 (b), depicts a square cross-section scaffold. The direct ink writing of very sharp corners is very difficult to achieve and requires a very solid paste coming out from the nozzle. Instead, fig. 3.13 (b) shows a cross-section that is slightly wider at its mid-height, an effect more evident for lower layers, i.e. that undergo more the load caused by the weight of the structure. However, the difference compared to a circular cross-section is appreciable: the welding areas, i.e. the contact area between two different layers, are visibly more extended. Furthermore, sharp corners are not desirable because, especially if the welding between the layers is not good, they

can lead to stress intensification phenomena compromising the mechanical properties of the specimen.

The third picture, fig. 3.13 (c), shows hollow filament scaffolds printed in an oil bath. The difficulty in their printing is demonstrated by the final scaffold: the filaments are not perfectly hollow and the size of the holes is not 0.75 mm i.e. it is not equal to the size of the mandrel. The cracks visible in the middle filament are probably caused by the face smoothing process. However, the joint area shows a good degree of interpenetration and the different cross-section is absolutely evident with respect to circular, fig. 3.13 (a), and square, fig. 3.13 (b), cross-sections. Consequently, these lattices are still valuable in view of a comparison of the mechanical properties. Concluding, the darker colour visible on the filament parts that are exposed during pyrolysis is due to sunflower oil: some organic residues can settle on the surface during the heat treatment.

Going on, fig. 3.13 (d) shows a scaffold printed with ink-2*, i.e. with 5%wt of carbon fibers. It is immediately visible how the lower amount of fibers with respect to ink-2, fig. 3.12 (c), seems to allow a better filament interpenetration and then welding. However, the lattice has a slight flattening of the first layers, i.e. the ones most subject to scaffold weight, where the filament cross-sections appear more ellipsoidal than rounded. Remembering that ink-2* does not contain fumed silica, the higher collapse in comparison with ink-2 scaffolds can be caused by two reasons:

- the lower quantity of fibers reduces the filaments stiffening action due to their introduction, i.e. filament collapse is easier;
- scaffolds printed with ink-2* differ from those printed with ink-2 from the filament diameters: the former are extruded through a 1.5 mm nozzle while the latter with a 0.016 inches (0.4064 mm) one. Consequently, for what explained in sec. 3.1.2.3, the drying behaviour is different, requiring more time with 1.5 mm diameter sections. Therefore, scaffolds with thicker filaments are more susceptible to drying-linked collapsing.

One co-extruded scaffold, presenting ink-1* in the external (or shell) part and ink-2* in the middle (or core) part, is then shown in fig. 3.13 (e). As it is visible, the scaffolds present cracks ascribable to the different shrinkage between the two inks: the core material presents a lower shrinkage than the shell material, leading to residual tensile stresses on the latter that cause its cracking, 3.2.4.

Finally, fig. 3.13 (f), shows a co-extruded scaffold where the core material is ink-1* while the shell material is ink-2*. In this case, the

printing quality is lower than the other kind of co-extruded scaffold i.e. the core material is not well distributed in the very central part. This can be linked to two classes of phenomena:

- operative: the inner feeding channel is not well-positioned in the middle but slightly decentralized;
- rheological: ink-2* is more unstable (sensitive to pressure variations) than ink-1* because of the fibers. Consequently, its passage in the outermost channel, which is thinner, can cause filament distortion, higher than in the previous case where ink-2* is the inner material.

No cracks are visible on the external surface, but, following the same considerations made before, it will be probable to find cracks within the core material.

3.2.2 *Microstructural characterization*

After evaluating the macrostructure of the printed scaffolds, it is advisable to observe their microstructure, in particular for scaffolds containing carbon fibers. Considering that Silres MK®-based and Silres H44®-based scaffolds have hardly distinguishable microstructures, Silres MK®-based is taken as example in this section because of the higher number of specimens produced.

Fig. 3.14 (a) shows the fracture surface of a scaffold printed with ink-1*. The structure is in accordance with those found by Elsayed *et al.* [43], consisting of a "spongy" structure where calcite is well distributed and bonded with the polymer-derived matrix.

Fig. 3.14 (b) focuses on a carbon cluster with a size of about 2.3 µm. SEM-EDS observation allows the detection of carbon by estimating an atomic composition consisting of 77.89% C, 14.93% O, 3.41% Si and 3.77% Ca. Of course, also some material underneath or to the side of the carbon domain is detected due to its small size. That is the reason why also low quantities of Ca, O and Si are present. However, it must be specified that it is rare to find these carbon domains during SEM observations. According to Elsayed *et al.* [43] their dimensions are within the nanometer range. Therefore, it is not excluded that the carbon phase found may be due to some accidental impurity.

In fact, the pyrolysis of silicones, characterized by a Si-O backbone, carried out in inert atmosphere gives the formation of amorphous $Si_xO_yC_z$ as shown in fig. 1.3 and mentioned in sec. 3.1.1, in which Si should be simultaneously bonded to C and O. However, the particular atmosphere and the presence of fillers prevent the formation of the Si-C bond, leading to “free” C domains, the content of which may vary

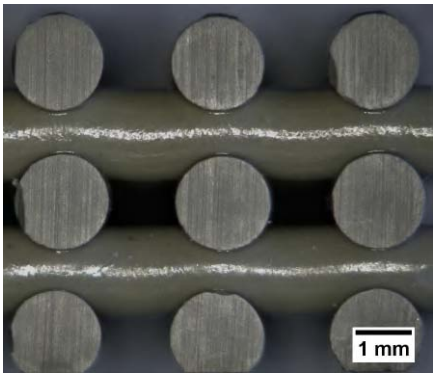

(a) *Ink-1*, circular cross-section.*

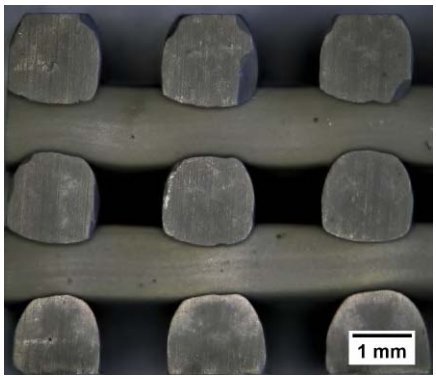

(b) *Ink-1*, square cross-section.*

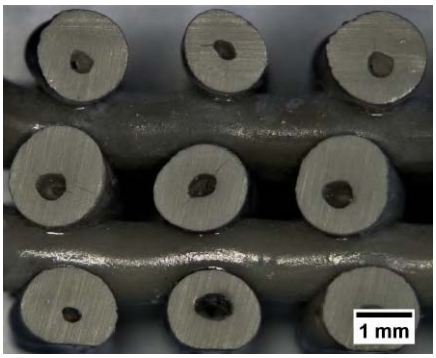

(c) *Ink-1*, hollow cross-section (printed in oil bath).*

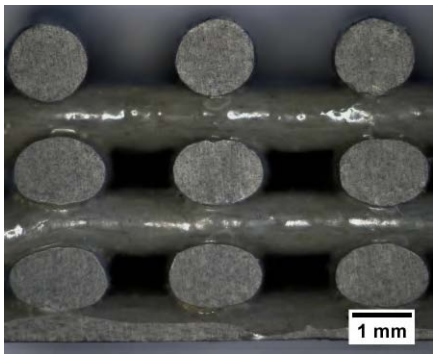

(d) *Ink-2*, circular cross-section.*

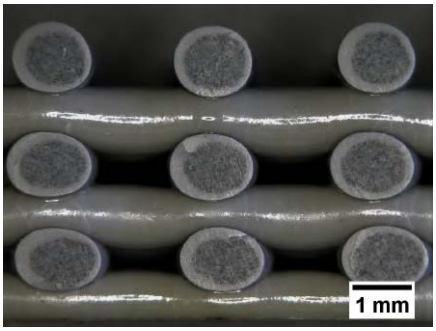

(e) *Ink-2* (core) and ink-1* (shell), co-extrusion.*

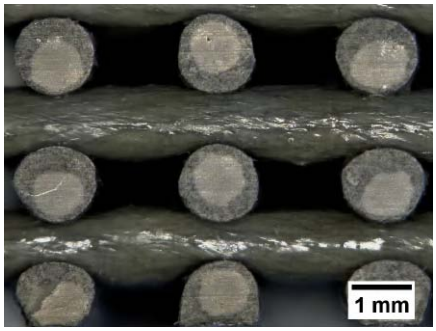

(f) *Ink-1* (core) and ink-2* (shell), co-extrusion.*

Figure 3.13: Different scaffold cross-sections printed at Friedrich-Alexander-Universität Erlangen-Nürnberg.

by changes of the organic substituents to silicon: an increase in volatile groups (e.g. phenyl groups) concentration leads to higher C content, thus Silres H44®, a methyl-phenyl polysiloxane, will give more carbon that Silres MK®, a methyl silicone (ch. 2, sec. 2.1.1). The separation of "free" C is also responsible for the black colour.

It is then interesting to look at scaffolds containing carbon fibers. The main issue of adding carbon fibers is the different shrinkage behaviour

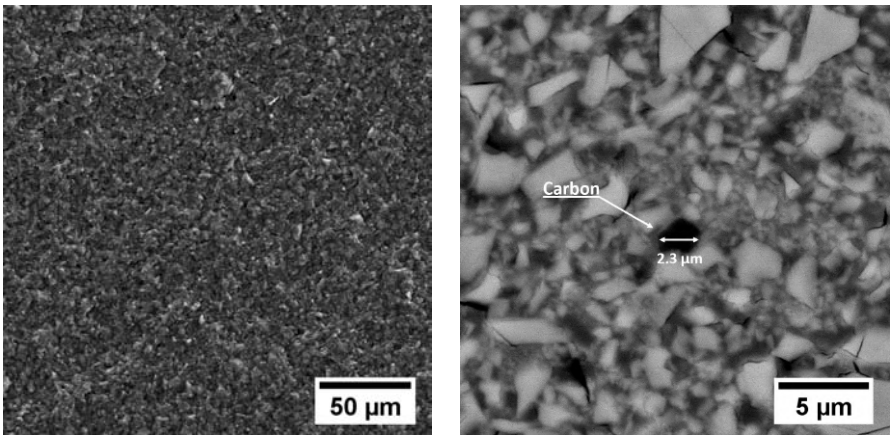

(a) *Fracture surface.* (b) *Polished surface.*

Figure 3.14: Microstructure of Silres MK®-based scaffold.

of carbon fibers and matrix: the pre-ceramic polymer undergoes a high volume contraction during the polymer-to-ceramic transformation, 1.2, while carbon fibers are subjected to negligible variations due to their very low coefficient of thermal expansion. Therefore, considering that the new ceramic matrix (brittle) is unable to absorb the deformation energy, it will release the stresses through the formation of cracks starting at the interface between the matrix and the fibers, where the constraint is maximum.
As already shown, fig. 3.12 (c-f), scaffolds printed with a 0.016 inches (0.4064 mm) nozzle present negligible surface cracks caused by the differential shrinkage between fibers and matrix. However, the presence of cracks in the core part of the filament can not be excluded. Conversely, scaffolds printed using 1.5 mm nozzle present evident shrinkage cracks, fig. 3.15. The reason could be the dimension of the nozzle (and then filament diameter): more mass will shrink leading to an increased probability of cracks i.e. the absolute shrinkage is higher compared to a thin filament. Furthermore, pure silica phases are detected within the joint area that can be caused by an inadequate mixing of the ink. The joint area also presents one discontinuity (pore) which, however, may be related to excessive polishing during sample preparation.

Other interesting observations can be made about the matrix-fiber interface. Firstly, a good composite should have two characteristics:

- weak fiber-matrix interface: it is necessary in order to obtain the *pull-out effect*, i.e. an extending crack does not pass through the fiber but around it, increasing the propagation path and consequently relaxing more energy;
- weak matrix: it is strictly connected to the previous point. In fact, in order to have the pull-out effect, it necessary that the crack

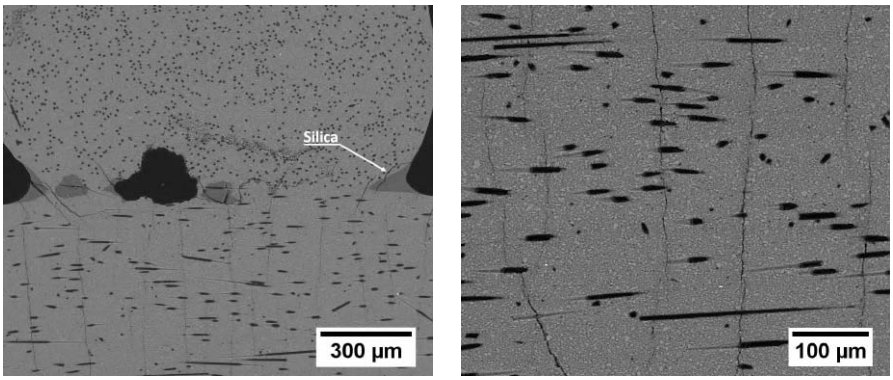

(a) *Joint area.* (b) *Differential shrinkage cracks.*

Figure 3.15: SEM images of ink-2* scaffold printed with a 1.5 mm nozzle.

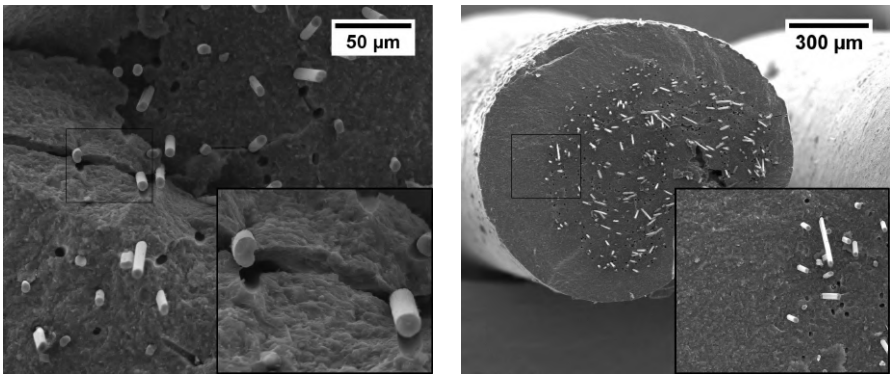

(a) *Crack propagation within the composite.* (b) *Interface between core and shell material.*

Figure 3.16: SEM images of scaffolds containing carbon fibers.

occurs within the matrix and not in the fiber, i.e. the matrix must fail before the reinforcement.

Fig. 3.16 (a) clearly shows that these two features are achieved. The crack deflects when it encounters a fiber along its path by passing around it. Furthermore, the prints left in the matrix and the protrusion from the fracture surface of the fibers demonstrate the pull-out effect: fibers have to be uprooted from the matrix in order to break the filament. This will lead to an increase in toughness.

Fig. 3.16 (b) shows an example of co-extruded filament with a focus on the interface between the core and the shell material. This area demonstrates a perfect continuity between the two zones which are only distinguishable by the presence, or not, of carbon fibers. The same continuity between core and shell was found by inverting their inks position.

3.2.3 *XRD measurements*

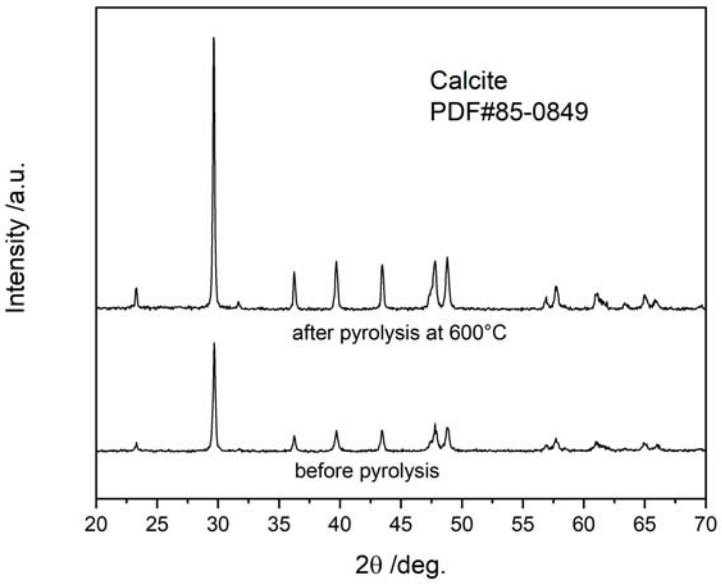

Figure 3.17: Example of XRD pattern.

All the different typologies of printed scaffolds were analyzed through XRD measurements, 2.4.10, in order to assess their crystalline phase composition.

All the different measurements reveal the same final pattern visible in fig. 3.17, in perfect agreement to those obtained in a previous work by Elsayed *et al.* [43]. The pattern reveals the presence of only one crystalline phase ($CaCO_3$, PDF#85-0849) both before and after pyrolysis.

This pattern allows to make some considerations:

- calcite is effectively the only crystalline phase both before and after pyrolysis, i.e. $CaCO_3$ does not occur to any phase transformation in inert atmosphere when pyrolysed at 600°C. Therefore, the goal of reaching a final scaffold that keeps the bioactive phase intact has been successfully achieved;
- there is no detection of any crystalline SiO_2 or SiC, i.e. the ceramic matrix is composed by amorphous or partially crystalline silica that can be written as SiO_x, where x is higher than 2. Crystalline SiO_2 or SiC can not be totally excluded, but in that case, their quantity is negligible, not allowing detection by XRD;
- no trace of graphitic carbon, fig. 2.2, is found. This is caused by the low amount of carbon fibers present, ranging between

5-10%wt, which prevents their detection. Furthermore, low Z (atomic number) elements, like carbon, are difficult to quantify by XRD.

3.2.4 *Linear shrinkage*

Scaffolds printed with ink-3 (i.e. Silres H44®, tab. 2.4) were printed only in the form of lattices. Measuring the decreasing in their dimensions, shrinkage is equal to about 5%.

Linear shrinkage is then calculated more precisely for Silres MK®-based scaffolds by measuring the lengths of single filaments before and after pyrolysis. The percentage linear shrinkage was calculated only for filaments printed using 1.5 mm diameter (or side) nozzle in tab. 2.6, i.e. the filaments used during the bending tests, 3.3.2. The results are shown in tab. 3.2.

The very low value of linear shrinkage is related to the very high amount of filler, i.e. calcite. Filaments without carbon fibers show a shrinkage of 3.7%, while filaments containing carbon fibers have a shrinkage approximately equal to zero. Co-extruded filaments are in between.

Furthermore, Silres H44®-based scaffolds show a higher shrinkage than those based on Silres MK®. The reason is the lower ceramic yield of Silres H44® that will lose more mass during pyrolysis if compared with Silres MK® (chapter 2, sec. 2.1.1).

All the dimensions were calculated using a digital caliper.

Table 3.2: Linear shrinkage of Silres MK®-based filaments.

Ink	Linear shrinkage [%]	Note
Ink-1*	3.7 ± 0.8	average between full circular, full square and hollow cross-sections
Ink-2*	0.2 ± 0.2	circular cross-section
core=Ink-2* shell=Ink-1*	1.6 ± 1.5	circular cross-section, filaments slightly bent after pyrolysis
core=Ink-1* shell=Ink-2*	0.4 ± 0.7	circular cross-section

3.3 POROSITY AND MECHANICAL PROPERTIES

The last and fundamental step is the evaluation of the mechanical performance of the printed scaffolds.

The first part of this section will show the compressive strength of the printed scaffolds, while the second part the bending behaviour of single filaments.

As regards porous materials such as lattice structures, compressive strengths should be always coupled with the porosity of the specimen.

3.3.1 *Compression tests and porosity*

The printed scaffolds are finally tested in compression by using the Instron, 2.2.7. As already explained, 2.4.8, the compression test often represents the most reliable mechanical test for ceramics. In addition, considering the specific application of the printed scaffolds, compression loads, generated by body weight, corresponds real state of stresses of the implant.

Compressive tests were performed in two different moments: during the period spent at the University of Padua and then at the Friedrich-Alexander-Universität Erlangen-Nürnberg.

3.3.1.1 *Scaffolds tested at the University of Padua*

Firstly, scaffolds printed with 0.016 inches (0.4064 mm) nozzle were tested using the Instron 1121 UTM (Instron Danvers, MA, USA), 2.2.7. Before the compression tests, specimens are stripped of the edges, exposing the actual scaffold as shown in fig. 2.23 (a) and fig. 3.10. After weighing, Their faces are then flattened and the geometrical (or bulk) density of the lattices is measured using equation 2.8. Then, the apparent (or skeletal) density is measured by helium pycnometer,

Table 3.3: Physical properties of scaffold printed at the University of Padua.

Scaffold	Bulk density [g/cm^3]	Apparent density [g/cm^3]	Porosity [%]
Ink-1	0.91 ± 0.05	2.20 ± 0.01	59 ± 2
Ink-2	0.81 ± 0.06	2.11 ± 0.01	62 ± 3
Ink-3	1.01 ± 0.06	2.37 ± 0.01	57 ± 2
Ink-4	0.78 ± 0.03	2.22 ± 0.01	65 ± 1

2.2.6, allowing the evaluation of the open porosity by using eq. 2.13. Since the pycnometer measurements carried out at the University of Padua have given inconsistent and therefore untruthful results, the apparent density of ink-1* and ink-2* samples calculated at Friedrich-Alexander-Universität Erlangen-Nürnberg (sec. 3.3.1.2, tab.3.4) was used also for ink-1 and ink-2 samples, even if in the case of ink-2* the amount of fibers was 5%wt instead of 10%wt.

Density measurements, and therefore porosity, and compression tests were performed on samples with dimensions of 9x9x5 mm^3. Five specimens for each ink were tested.

Geometrical (or bulk) density, apparent (skeletal) density and open porosity are shown in tab. 3.3. Open porosity is also visible in fig. 3.18 (a). After the compression tests, the samples are finely ground in order to measure their true density, 2.4.5. However, considering that the calculated true density was equal to the apparent density, it is not present in tab. 3.3. Therefore, no closed porosity is detected.

Silres MK®-based scaffolds, i.e. ink-1 and ink-2, show a lower density than those based on Silres H44®, i.e. ink-3 and ink-4. Moreover, scaffolds without carbon fibers, ink-1 and ink-3, present similar porosities accompanied by a very small standard deviation. The porosity values are in agreement with those found by Elsayed *et. al* [43], confirming the high quality and reliability of printing.

Furthermore, the addition of carbon fibers, ink-2 and ink-4, reduces both the geometrical and apparent density. However, the geometrical densities decrease more than apparent densities, leading to a higher porosity. This is a consequence of carbon fibers presence and alignment during printing: carbon fibers make the structure stiffer along fiber direction, reducing the shrinkage, but, in the direction perpendicular to the fibers, the matrix is able to shrink, therefore the diameter of the struts decreases. Consequently, the total size of the scaffold varies only slightly, while the diameter of the filaments changes more evidently. Therefore, the decrease in apparent (or skeletal) volume is not balanced by a decrease in geometrical (or bulk) volume. The result is an increase in the measured porosity. Furthermore, the joint areas represent a sort of constraining that oppose to the radial shrinkage of the filament. This can contribute to the cracks visible within the joint areas in fig. 3.12 (d) and (f).

Then, the scaffolds are positioned in the Instron as shown in fig. 2.12 (a). The results of the compression tests are visible in fig. 3.18 (b). The numbers displayed are the mean values.

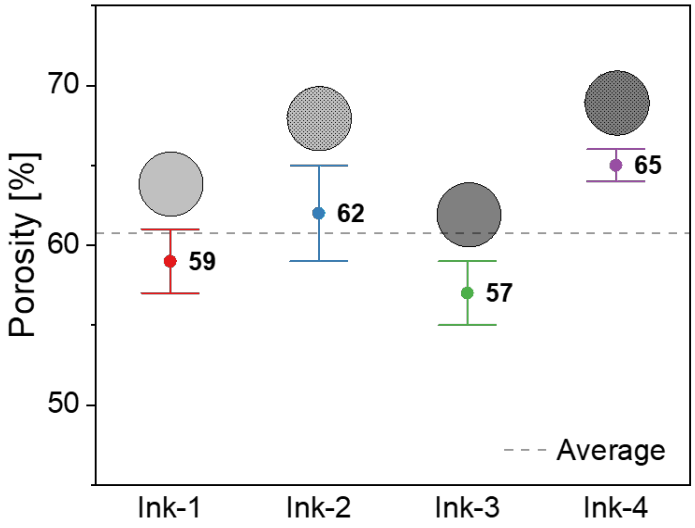

(a) *Porosity.*

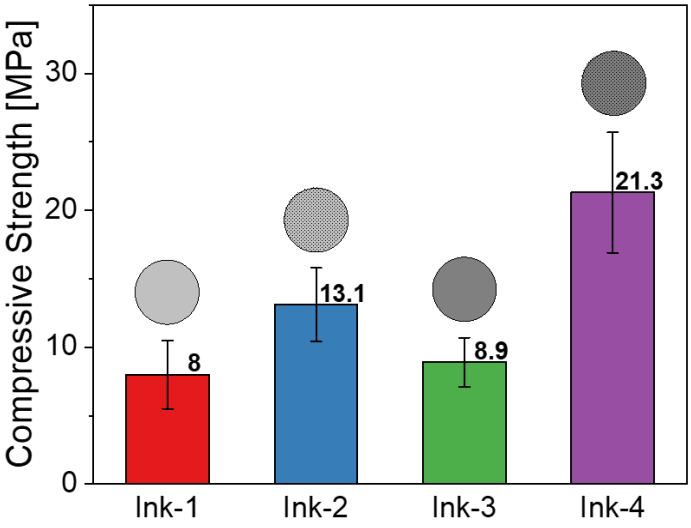

(b) *Compressive strength.*

Figure 3.18: Porosity and compressive strength. Scaffolds printed using 0.016 inches (0.4064 mm) nozzle.

Silres MK® and Silres H44® based scaffolds without fibers exhibit similar compressive strengths: the mean values are 8 MPa and 8.9 MPa, respectively. On the contrary, despite both ink-2 and ink-4 have a higher compressive strength, Silres H44®-based scaffolds receive a much more evident benefit from the addition of fibers. This difference is connected to what has been said previously in sec. 3.1.2.1 and 3.2.1.1, i.e. the good welding between different layers is partially compromised by the amount of the fibers and this effect is more evident for ink-2 rather than ink-4. This delamination phenomena of ink-2 scaffolds is certainly to be avoided but allows the evaluation of the influence that good welding between layers has on the mechanical properties: if the joint is weak, the material will not behave as a unique body. The introduction of inevitable shear stresses during compression, caused by small morphology inhomogeneity, can break the joint between the layers. Of course, this effect is all the more evident the weaker the joint, i.e. ink-2 scaffolds are more susceptible to this phenomenon. The consequence is that the stresses are not effectively transmitted from one layer to the others, causing their mutual sliding and the premature failure of the specimen.

Finally, the values are in agreement with the compressive strength of trabecular bone (2–12 MPa) [18, 19]. This is confirmed by the Ashby plot using the software CES EduPack 2018 in fig. 3.19. The used version does not include trabecular of cancellous bone properties, but only those of cortical bone. Considering that the porosity of trabecular bones usually ranges between 50-90% [20], trabecular bone properties are modelled as open-cell foams using the function "synthesizer", present in the software, starting from the properties of cortical bone (colour "aqua" in fig. 3.19). It should be noted that an approximation has thus been introduced since the spongy bone can also have a closed-cell structure. In fact, its cellular structure can be made up by an interconnected network of "rod" or "plates". A network of rods will lead to an open-cell structure, while a network of plates to a higher density closed-cell structure [21]: at lowest densities, the cells are open, i.e. a network of rods, and, as the density increases, the rods will progressively spread and flatten becoming plates, leading to a closed-cell structure. This transition happens at porosity of 80% [21]. However, the software CES EduPacK sets the lowest porosity limits for closed-cell to 70%. Considering the aim of this Ashby plot, i.e. qualitative comparison, open-cell models is considered appropriate. Five porosities (from 50% to 90% with a step-size of 10%) are then shown in fig. 3.19 (colour "teal"). Furthermore, scaffolds in tab. 3.3 are added to the chart by using the function "tools>add record". The selection line for the mass optimization in compression corresponds to a line with slope 1 in logarithmic scale. Fig. 3.19 clearly show that the produced scaffolds have properties very similar to those of natural

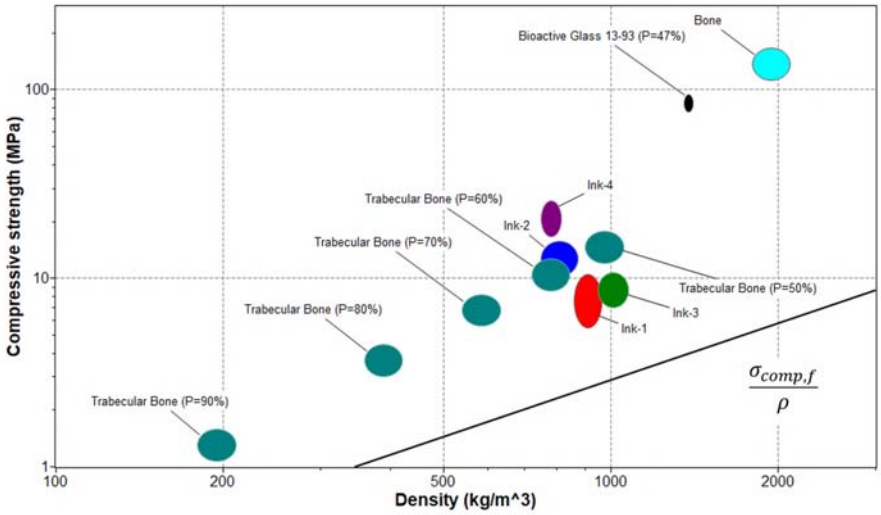

Figure 3.19: Ashby plot of compressive strength against density (scaffolds printed at the University of Padua).

bone. Furthermore, they are not far from bioactive glass 13-93 [88] ("black" in fig. 3.19) which is one of the most studied and popular materials for scaffolds produced by direct ink writing.

3.3.1.2 *Scaffolds tested at the Friedrich-Alexander-Universität Erlangen-Nürnberg*

Six main different scaffolds were printed during the time spent at the Friedrich-Alexander-Universität Erlangen-Nürnberg. The goal is to compare the compressive strength of scaffolds having different cross-sections both in terms of shape and material (with or without fibers). The printed scaffolds are freed from the edges and cut into four parts using a diamond wire cutter, 2.23 (b) and (c). Their faces are then smoothed and made parallel using an 18 µm abrasive paper.

The different scaffolds are named as follows:

- C: full circular cross-section, ink-1*;
- S: full square cross-section, ink-1*;
- H: hollow cross-section, ink-1*;
- CF: full circular cross-section, ink-2*;
- CO-1: co-extrusion, shell=ink-1*, core=ink-2*;
- CO-2: co-extrusion, shell=ink-2*, core=ink-1*.

Density measurements, and therefore porosity, and compression tests were performed on samples with dimensions of 9x9x5 mm^3 as previously explained. Ten specimens for each type were tested.

Table 3.4: Physical properties of scaffolds printed at the Friedrich-Alexander-Universität Erlangen-Nürnberg.

Scaffold	Bulk density [g/cm³]	Apparent density [g/cm³]	Porosity [%]
C	1.09 ± 0.08	2.20 ± 0.01	51 ± 4
S	1.24 ± 0.07	2.20 ± 0.01	44 ± 3
†H	1.04 ± 0.08	2.17 ± 0.01	52 ± 4
CF	1.03 ± 0.04	2.11 ± 0.01	53 ± 2
CO-1	1.04 ± 0.04	2.14 ± 0.01	50 ± 2
CO-2	1.00 ± 0.06	2.13 ± 0.01	53 ± 3

†*the true density is equal to* 2.20 ± 0.01 *g/cm³*.

Geometrical and apparent densities and the open porosities are shown in tab. 3.4. Also in this case, the true densities (i.e. density of the powder), were equal the respective apparent density, except for the hollow scaffolds (H). In this case, the true density, equal to 2.20 ± 0.01 is different from the apparent density. Using equation 2.19, closed porosity is about 1%. However, in the light of SEM images, it is possible to say that this porosity is actually due to interruptions of the cavities. Furthermore, the porosity of H-samples is not very different from the other samples, demonstrating the non-optimal quality of the printed scaffolds: even if the scaffolds are hollow, fig. 3.13 (c), the filaments are thicker than the other scaffolds while the hollows are thin, reducing the overall porosity.
Only two scaffolds were almost completely hollow, showing a porosity of 59%. These were not tested in compression.
On the other hand, S-samples (square cross-section) are characterized by a higher geometrical density, i.e. a lower open porosity: this was expected, because while the printing geometry (i.e. the nozzle path) is the same for all the scaffolds in tab. 3.4, the square cross-section has a side of 1.5 mm, leading to a theoretical square cross-section area of 2.25 mm². On the contrary, the 1.5 mm diameter nozzle will extrude filaments with a 1.77 mm² cross-section.

Following what already written in chapter 2, sec. 2.4.8, the scaffolds are tested using the Instron 4204 UTM (Instron Corporation, Canton, USA), 2.2.7. The specimens are positioned as shown in fig. 2.12 (b) and the results, accompanied by porosity, are shown in fig. 3.20.

Scaffolds printed with square cross-section shows an average increase in compressive strength of about 2 MPa compared to lattices with a full circular cross-section. This is due to a greater contact area between two successive layers, which allows a more effective and

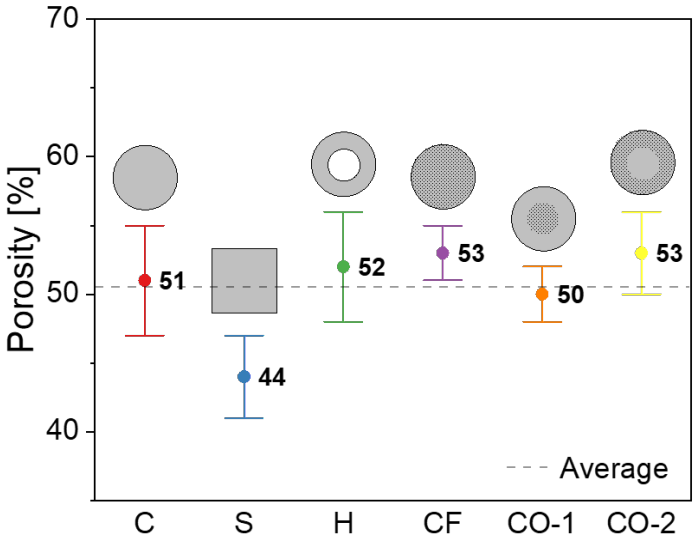

(a) *Porosity.*

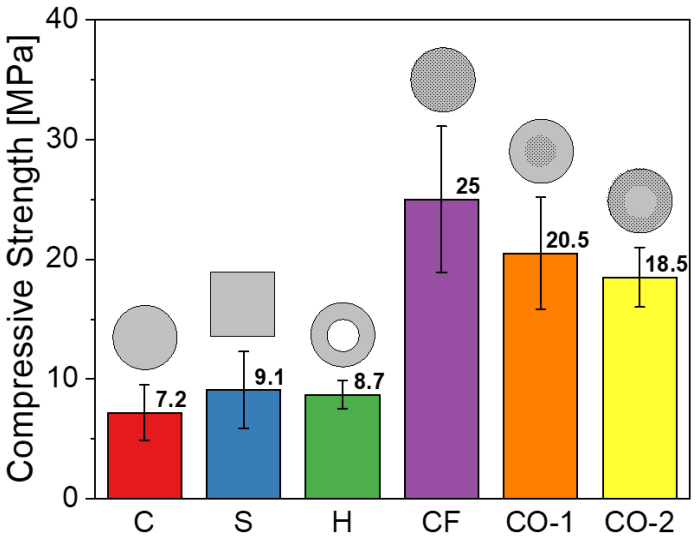

(b) *Compressive strength.*

Figure 3.20: Porosity and compressive strength. C: full circular cross-section, ink-1*. S: full square cross-section, ink-1*. H: hollow cross-section, ink-1*. CF: full circular cross-section, ink-2*. CO-1: co-extrusion, shell=ink-1*, core=ink-2*. CO-2: co-extrusion, shell=ink-2*, core=ink-1*.

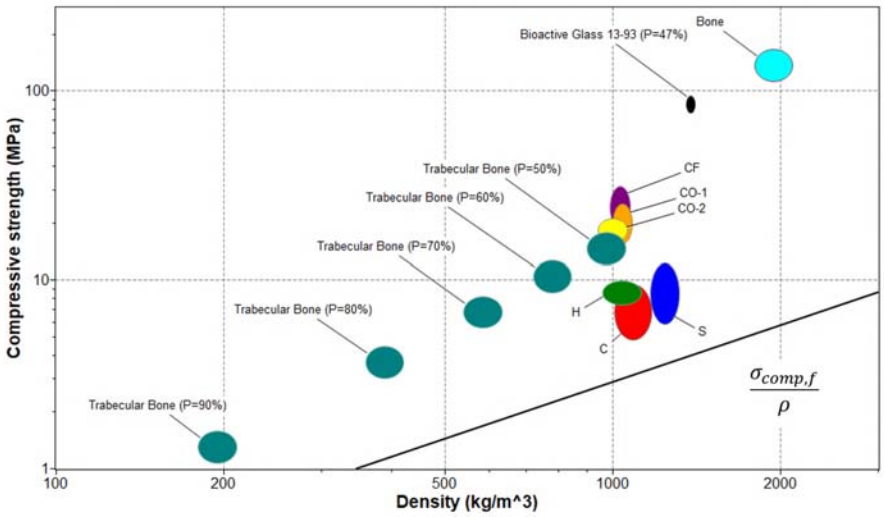

Figure 3.21: Ashby plot of compressive strength against density (scaffolds printed at the Friedrich-Alexander-Universität Erlangen-Nürnberg).

distributed transfer of tensions: if the filament is circular, the flow of tensions must pass through a lower area, generating stress intensification points at the joints. However, when talking about ceramic materials, it must always be considered that a greater quantity of material, and therefore of volume affected by the compression, corresponds to a greater probability of finding critical cracks, which could lead to a lower compressive strengths and greater result uncertainties. Therefore, the increase in compressive strength is both enhanced, thanks to the better flow of stresses, and reduced, due to the higher volume.

This concept, introduced by Weibull in 1951, can also explain why hollow scaffolds (H), consisting of less material, have better compressive strength and a lower standard deviation than circular cross-section scaffolds. Anyway, the compressive strengths are in good agreement with those found in Padua.

CF-specimens, containing 5%wt of carbon fibers, demonstrated better compressive strength than those printed in Padua using ink-2 (i.e. 10%wt of carbon fibers): this can be attributed to the better joint between the layers achieved by reducing the amount of fibers (see 3.1.2.1) and also to the lower porosity. In fact, the compressive strength to density ratio of ink-2 scaffolds is similar to that of CF-scaffolds. Furthermore, the presence of carbon fibers reduces the volume-effect introduced by Weibull, evident for brittle materials, because even if the probability of crack increases with thicker filaments, the presence of the fibers and their pull-out guarantees the continuity of the body.

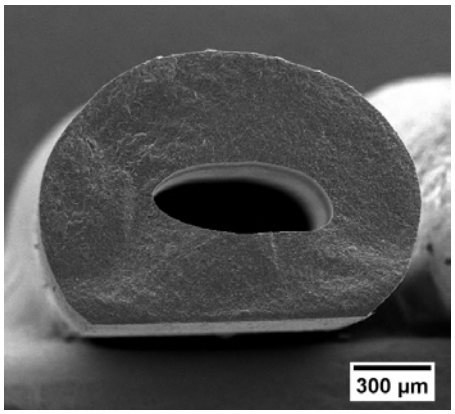

Figure 3.22: SEM image of a hollow filament used during bending tests.

Another result is that CO-1 samples exhibit higher compressive strength than CO-2 samples. This is still ascribable to the better joint achievable when the contact is between filaments that do not contain fibers. However this joint is very brittle.

Following the same considerations made in the previous section, 3.3.1.1, the results are plotted against density, fig. 3.21. Also in this case, the printed scaffolds show characteristics similar to those of natural bone and not far from bioactive glass 13-93.

3.3.2 *Filaments bending tests*

Bending test of single filaments composing the scaffolds was the last mechanical test performed.

The six different cross-sections in fig. 3.13 were printed in the form of single filaments. After drying and pyrolysis, the bars are loaded in the Instron Instron 4204 UTM (Instron Corporation, Canton, USA) using the proper setup visible in fig. 2.13. Then, the tests are performed following the procedure and the setup explained in chapter 2, sec. 2.4.9.

One advantage of bending tests is that the manufacture of single hollow filaments is absolutely easy if compared to a complete scaffold. In addition, they are also easily printable in the air. One example of hollow filament used during this test is shown in fig. 3.22. Therefore, considering that filaments are directly deposited on the substrate during printing, their base, fig. 3.22, will result slightly flattened. For this reason, the moment of inertia of filaments that were evidently flattened was assessed as an average between that of a perfect circle and a perfect rectangle.

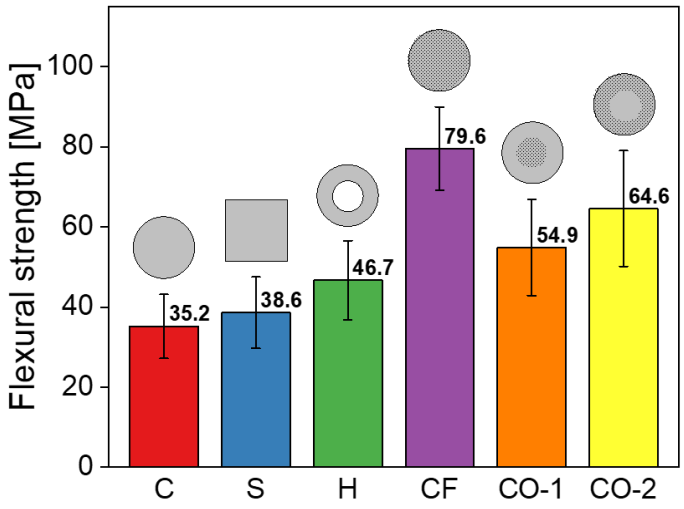

Figure 3.23: Flexural strength of filaments printed at the Friedrich-Alexander-Universität Erlangen-Nürnberg.

Then, considering the difficulty of estimating the size and continuity of the hole, hollow filaments were treated as full circular cross-sections for the calculation of $\sigma_{flex,f}$, eq. 2.24. The results of the bending tests are shown in fig. 3.23 where the different filaments are named in the same way as in the previous section.

The filaments show appreciable flexural strengths, higher than those found by Franchin *et al.* [87].

The flexural strength values of C and S samples are similar despite the higher volume of a square cross-section filament. Therefore, in the specific case, the increase in moment of inertia of a square cross-section influences the bending strength more than its increase in volume.

It is then interesting to confirm what found during compression tests: H filaments exhibit higher flexural strength than their "cousins" (C and S). This is connected to the lower volume and the consequent lower probability of finding critical cracks. Therefore, the bending behaviour of C, S and H scaffolds confirms the results of compression tests in the previous section, 3.3.1.2.

The bending test demonstrates again the importance of having a good joint between two successive layers. Indeed, CO-2 filaments require about 10 MPa more than CO-1 to reach the failure stress. The explanation is trivial: considering that the stress distribution along the thickness during bending follows the Navier's equation, the maximum stress (both tensile and compressive) acts in the points which are more distant from the neutral axis of the bar, i.e. "butterfly" distribution of stresses. Consequently, the distribution the most resistant material in the most external areas, where the stress is maximum, is a winning

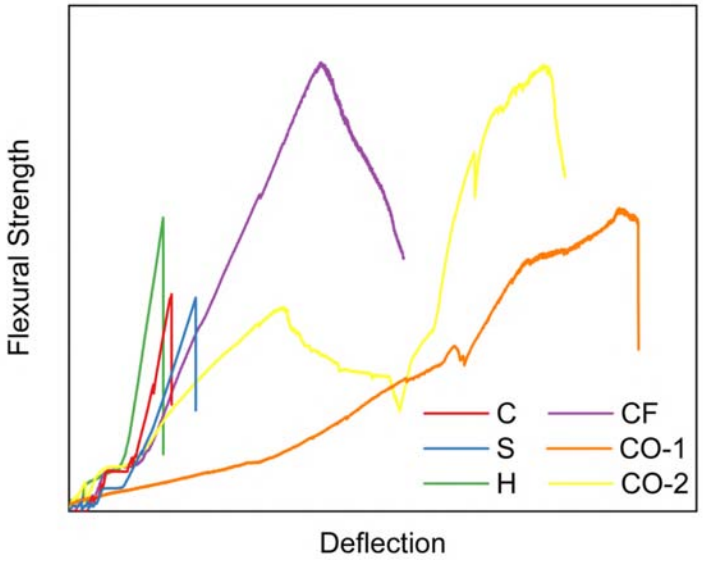

Figure 3.24: Qualitative curves from bending tests.

strategy. However, as shown in fig. 3.20, CO-1, in which the welding between layers is good, reveals better compressive strength than CO-2. This confirms the influence and importance of having good joints, able to guarantee the structural continuity of the scaffold.

The relatively high standard deviation of the measured values is due to irregularities of the filaments, such as surface roughness, distortion, and variations in the cross-section, inevitable during the printing processes. These are influenced by many different variables, i.e. environment condition, pressures, speed, etc., that make difficult a perfect dimensional homogeneity.

Some qualitative curves are then visible in fig. 3.24. The test is stopped when there is an evident and abrupt decrease in stress, i.e. of the acting load. C, S and H filaments show the same behaviour, typical of brittle materials. Filaments containing carbon fibers, i.e. CF, CO-1 and CO-2, show different behaviour with a marked increase in toughness. Furthermore, when the test is over, those filaments do not result broken into two parts but they are still able to sustain some load. In particular, CO-2 filaments show a very particular behaviour with a first peak that is probably caused by the failure of the core brittle part (ink-1*), while the second one corresponds to the true failure. Similarly, CO-1 filaments show a first (smaller) peak caused by the failure of the shell brittle material.

3.4 GEOMETRY CONSIDERATIONS FOR TISSUE GROWTH

Starting from the considerations in chapter 1 sec. 1.3.4, it is possible to make a brief and basic discussion on the geometry. Even if there is currently only limited evidence available as to what kind of curvature is best for tissue, it has been consistently observed that the rate of tissue generation is proportional to the curvature of the surface and the type of curvature, i.e. tissue growth prefers concave surfaces instead of convex or flat surfaces [51, 55]. In particular, the formation of new tissue starts at the corners of the polygonal channels, i.e. where the local curvature is higher, while cells on the faces are initially resting. On the other hand, if the channel is round, the tissue grows uniformly, fig. 1.10. A process of rounding, that creates a central circular opening regardless of the original shape, can be observed.

Therefore, an increase in tissue ingrowth can be firstly made creating concave surfaces. Consequently, hollow structures will be interesting: the holes will introduce a concavity similar to the pore in fig. 1.10 (iv). On the other hand, scaffolds with square cross-section filaments will lead the porosity in fig. 3.13 (b), similar to that in fig. 1.10 (ii) that will reasonably represent the tissue formation on it.

Furthermore, if we consider an implant with defined dimensions and porosity, smaller filament cross-sections, i.e. smaller nozzle diameters, should lead to lattices with better tissue growth potential. This statement is based on two observation:

- local curvature: filament with smaller diameter corresponds to a higher local curvature resulting in higher levels of stress concentration and thus tissue regeneration stimulus, 1.3.4;
- number of joints: the joint area leads to a change in curvature and to the formation of concave areas that promotes tissue formation

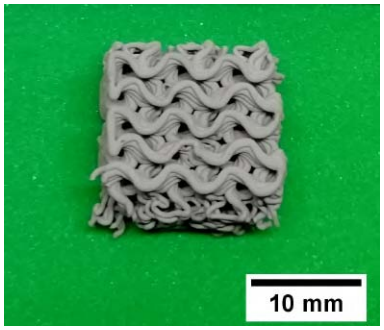

(a) *Gyroid structure printed at the University of Padua.*

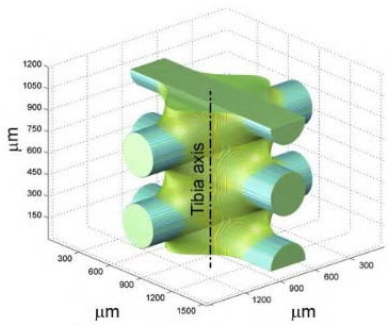

(b) *Curvature-driven tissue growth simulation in the joint area [89].*

Figure 3.25: Gyroid structure and curvature-driven tissue growth simulation.

[89], fig. 3.25 (b). Consequently, if the final porosity is the same, the smaller is the filament diameter, the higher is the number of joint areas in the lattice. Therefore there are more points that can give high tissue regeneration stimulus.

Therefore, the introduction of concave form and the increase of joint area points could improve the response of the material.

It will be then interesting to test more complex structure such as gyroid, that introduces constant change in curvature, increasing the quantity of concave areas. These complicated structures are usually produced by indirect additive manufacturing techniques, such as stereolithography (SLA) or digital light processing (DLP) which allows more freedom in terms of geometry precision and detail. However, gyroid structures were successfully printed using ink-1 at the University of Padua during this thesis work, fig. 3.25 (a).

4

CONCLUSIONS AND FUTURE DEVELOPMENTS

In order to complete this dissertation, the work done is briefly resumed highlighting the results and objectives obtained. Furthermore, some considerations about future developments and perspectives are proposed.

4.1 CONCLUSIONS

Direct ink writing (DIW) and robocasting were successfully adopted for the manufacturing of ceramic composite scaffolds for bone tissue engineering. The process started from a mixture of pre-ceramic polymers and calcite, eventually added with fumed silica. Furthermore, carbon fibers were successfully inserted into the mixture in order to increase the mechanical and photothermal properties of the samples.

During the time spent at the University of Padua, four different inks were extruded in the form of lattices consisting of full cylindrical filaments with a diameter of 0.016 inches (0.4064 mm), without the help of fumed silica or any other additive to adjust the rheology. Furthermore, the passage from one pre-ceramic polymer to another did not compromise the quality of the final lattice, demonstrating the possibility of using Silres H44® instead of Silres MK®. These scaffolds were characterized, showing good mechanical strengths in agreement with previous works [40, 43] and comparable to that of natural bone and bioactive glass 13-93, fig. 3.19. The structures were also observed by SEM to assess their integrity.

During the time spent at the Friedrich-Alexander-Universität Erlangen-Nürnberg, different cross-sections with a diameter (or side) of 1.5 mm were extruded, showing the great versatility of the prepared inks that were characterized through rheological measurements. Therefore, fully circular, square, hollow and co-extruded filament cross-sections were extruded in the form of both single filaments and lattices. These scaffolds were characterized, showing good mechanical properties in agreement to that of natural bone and bioactive glass 13-93, fig. 3.21.

Both the experience showed the improvement obtained by adding fibers, showing evidence of a pull-out effect.

In conclusion, it is possible to assert that direct ink writing (and robocasting) technique is suitable for the prepared ink, leading to consistent and geometrically precise scaffolds.

4.2 FUTURE DEVELOPMENTS

In the beginning, the project was even more ambitious: to design and prepare a bifunctional scaffold in order not only to repair large bone defects but also to kill tumor cells.

This can be achieved by exploiting the photothermal effect of carbon present within the scaffold in the form of both pyrolytic carbon, deriving from the decomposition of the pre-ceramic polymers, and carbon fibers, if present. This last feature, that can be called "therapeutical", is the common thread of all the work which explains and influences the choices made during the months of research. However, the well-known events connected to the 2020 coronavirus pandemic (COVID-19) in Europe did not allow to finish the proposed work.

Therefore, the first, immediate and obvious future development will be to assess the photothermal properties of the printed scaffolds, in order to rank them. Previous works presented in ch. 1, sec. 1.4.2 clearly show the photothermal capacity of the "free" carbon derived from the pyrolysis of the pre-ceramic polymer. Silres H44® will give a ceramic with a higher amount of "free" carbon, ch. 3 sec. 3.1.1, than Silres MK®, thus also its photothermal effect should be higher. Furthermore, previous works also showed the photothermal potential of carbon fibers. It will be then interesting to compare scaffolds with and without carbon fibers. Hereafter, it will be also interesting to evaluate co-extruded scaffolds that should exhibit a photothermal effect close to those of normal scaffold with carbon fibers.

The second future development, that is currently in progress within the laboratories of the University of Padua, consists on biocompatibility and bioactivity *in vitro* tests in order to evaluate the effect of carbon fibers. In the case in which the carbon fibers considerably reduce the biocompatibility properties of the scaffolds, co-extruded filament lattices with carbon fibers only in the core part will become precious: the photothermal effect should be outstanding, exposing, at the same time, only calcite to the biological environment.

Another development, that is actually in progress at the University of Trento, is the pyrolysis under CO_2 atmosphere. This should prevent the decomposition of calcite until 900°C: it will be interesting to see if the amount of "free" carbon increases leading to a higher photothermal effect.

Despite the quality of the printed structures, hollow filaments can then be improved, for example by trying the extrusion in different liquid media or, in order to prevent warping due to inhomogeneous drying, performing the freeze-drying of the lattice.

Finally, the great versatility of extruded inks can be further explored by trying different and increasingly complicated structures.

BIBLIOGRAPHY

[1] Karen J.L. Burg, Scott Porter, and James F. Kellam. "Biomaterial developments for bone tissue engineering." In: *Biomaterials* 21.23 (2000), pp. 2347–2359.

[2] Paolo Colombo, Gabriela Mera, Ralf Riedel, and Gian Domenico Soraru. "Polymer-derived ceramics: 40 years of research and innovation in advanced ceramics." In: *Journal of the American Ceramic Society* 93.7 (2010), pp. 1805–1837.

[3] Peter Greil. "Active-filler-controlled pyrolysis of preceramic polymers." In: *Journal of the American Ceramic Society* 78.4 (1995), pp. 835–848.

[4] Giulio Parcianello. "Advanced ceramics from preceramic polymers and fillers." PhD thesis. 1848 via 8 Febbraio, Padova, Italy: Università degli Studi di Padova, 2012.

[5] Peter Greil. "Polymer derived engineering ceramics." In: *Advanced engineering materials* 2.6 (2000), pp. 339–348.

[6] T. Isoda, H. Kaya, H. Nishii, O. Funayama, T. Suzuki, and Y. Tashiro. "Perhydropolysilazane precursors to silicon nitride ceramics." In: *Journal of Inorganic and Organometallic Polymers* 2.1 (1992), pp. 151–160.

[7] FI Hurwitz, P Heimann, SC Farmer, and DM Hembree. "Characterization of the pyrolytic conversion of polysilsesquioxanes to silicon oxycarbides." In: *Journal of materials science* 28.24 (1993), pp. 6622–6630.

[8] Daniel Suttor, Hans-Joachim Kleebe, and Gunter Ziegler. "Formation of mullite from filled siloxanes." In: *Journal of the American Ceramic Society* 80.10 (1997), pp. 2541–2548.

[9] David Franklyn Williams. *The Williams dictionary of biomaterials*. Liverpool University Press, 1999.

[10] Wilson June et al. *An introduction to bioceramics*. Vol. 1. World scientific, 1993.

[11] Michael Scheffler and Paolo Colombo. *Cellular ceramics: structure, manufacturing, properties and applications*. John Wiley & Sons, 2006.

[12] Larry L Hench. "Bioceramics: from concept to clinic." In: *Journal of the american ceramic society* 74.7 (1991), pp. 1487–1510.

[13] Jeffrey O Hollinger, Shelley Winn, and Jeffrey Bonadio. "Options for tissue engineering to address challenges of the aging skeleton." In: *Tissue Engineering* 6.4 (2000), pp. 341–350.

[14] Arun K Nair, Alfonso Gautieri, Shu-Wei Chang, and Markus J Buehler. "Molecular mechanics of mineralized collagen fibrils in bone." In: *Nature communications* 4 (2013), p. 1724.

[15] JR Jones and LL Hench. "Biomedical materials for new millennium: perspective on the future." In: *Materials Science and technology* 17.8 (2001), pp. 891–900.

[16] Robert S Langer and Joseph P Vacanti. "Tissue engineering: the challenges ahead." In: *Scientific American* 280.4 (1999), pp. 86–89.

[17] Peter Fratzl, Klaus Misof, Ivo Zizak, Gert Rapp, Heinz Amenitsch, and Sigrid Bernstorff. "Fibrillar structure and mechanical properties of collagen." In: *Journal of structural biology* 122.1-2 (1998), pp. 119–122.

[18] Qiang Fu, Mohamed N Rahaman, B Sonny Bal, and Roger F Brown. "Preparation and in vitro evaluation of bioactive glass (13–93) scaffolds with oriented microstructures for repair and regeneration of load-bearing bones." In: *Journal of Biomedical Materials Research Part A: An Official Journal of The Society for Biomaterials, The Japanese Society for Biomaterials, and The Australian Society for Biomaterials and the Korean Society for Biomaterials* 93.4 (2010), pp. 1380–1390.

[19] Lutz-Christian Gerhardt and Aldo R Boccaccini. "Bioactive glass and glass-ceramic scaffolds for bone tissue engineering." In: *Materials* 3.7 (2010), pp. 3867–3910.

[20] Vassilis Karageorgiou and David Kaplan. "Porosity of 3D biomaterial scaffolds and osteogenesis." In: *Biomaterials* 26.27 (2005), pp. 5474–5491.

[21] Lorna J Gibson and Michael F Ashby. *Cellular solids: structure and properties*. Cambridge university press, 1999.

[22] Robert Lanza, Robert Langer, and Joseph P Vacanti. *Principles of tissue engineering*. Academic press, 2011.

[23] Pq Ducheyne and Q Qiu. "Bioactive ceramics: the effect of surface reactivity on bone formation and bone cell function." In: *Biomaterials* 20.23-24 (1999), pp. 2287–2303.

[24] Huipin Yuan, Zongjian Yang, Joost D de Bruijn, Klaas de Groot, and Xingdong Zhang. "Material-dependent bone induction by calcium phosphate ceramics: a 2.5-year study in dog." In: *Biomaterials* 22.19 (2001), pp. 2617–2623.

[25] Maddalena Mastrogiacomo, Silvia Scaglione, Roberta Martinetti, Laura Dolcini, Francesco Beltrame, Ranieri Cancedda, and Rodolfo Quarto. "Role of scaffold internal structure on in vivo bone formation in macroporous calcium phosphate bioceramics." In: *Biomaterials* 27.17 (2006), pp. 3230–3237.

[26] P Sepulveda, AH Bressiani, JC Bressiani, L Meseguer, and B König Jr. "In vivo evaluation of hydroxyapatite foams." In: *Journal of Biomedical Materials Research: An Official Journal of The Society for Biomaterials, The Japanese Society for Biomaterials, and The Australian Society for Biomaterials and the Korean Society for Biomaterials* 62.4 (2002), pp. 587–592.

[27] William De Long, Thomas Einhorn, Kenneth Koval, Michael McKee, Wade Smith, Roy Sanders, and Tracy Watson. "Bone grafts and bone graft substitutes in orthopaedic trauma surgery." In: *The Journal of Bone & Joint Surgery* 89.3 (2007), pp. 649–658.

[28] Alexander Hoppe, Nusret S Güldal, and Aldo R Boccaccini. "A review of the biological response to ionic dissolution products from bioactive glasses and glass-ceramics." In: *Biomaterials* 32.11 (2011), pp. 2757–2774.

[29] Ioannis D Xynos, Alasdair J Edgar, Lee DK Buttery, Larry L Hench, and Julia M Polak. "Gene-expression profiling of human osteoblasts following treatment with the ionic products of Bioglass® 45S5 dissolution." In: *Journal of Biomedical Materials Research: An Official Journal of The Society for Biomaterials, The Japanese Society for Biomaterials, and The Australian Society for Biomaterials and the Korean Society for Biomaterials* 55.2 (2001), pp. 151–157.

[30] F Monchau, Ph Hivart, B Genestie, F Chai, M Descamps, and HF Hildebrand. "Calcite as a bone substitute. Comparison with hydroxyapatite and tricalcium phosphate with regard to the osteoblastic activity." In: *Materials Science and Engineering: C* 33.1 (2013), pp. 490–498.

[31] G Guillemin, J-L Patat, J Fournie, and M Chetail. "The use of coral as a bone graft substitute." In: *Journal of biomedical materials research* 21.5 (1987), pp. 557–567.

[32] G Guillemin, A Meunier, P Dallant, P Christel, J-C Pouliquen, and L Sedel. "Comparison of coral resorption and bone apposition with two natural corals of different porosities." In: *Journal of biomedical materials research* 23.7 (1989), pp. 765–779.

[33] Hajime Ohgushi, Motoaki Okumura, Takafumi Yoshikawa, Keisuke Inboue, Norio Senpuku, Susumu Tamai, and Edwin C Shors. "Bone formation processin porous calcium carbonate and hydroxyapatite." In: *Journal of biomedical materials research* 26.7 (1992), pp. 885–895.

[34] AF Lemos and JMF Ferreira. "Porous bioactive calcium carbonate implants processed by starch consolidation." In: *Materials Science and Engineering: C* 11.1 (2000), pp. 35–40.

[35] *CERAMGLASS*. Università degli Studi di Padova. URL: https://research.dii.unipd.it/ceramglass/.

[36] Enrico Bernardo, Paolo Colombo, Emil Dainese, Giovanni Lucchetta, and Paolo F Bariani. "Novel 3D wollastonite-based scaffolds from preceramic polymers containing micro-and nano-sized reactive particles." In: *Advanced Engineering Materials* 14.4 (2012), pp. 269–274.

[37] L Fiocco, H Elsayed, JKMF Daguano, VO Soares, and E Bernardo. "Silicone resins mixed with active oxide fillers and Ca–Mg Silicate glass as alternative/integrative precursors for wollastonite–diopside glass-ceramic foams." In: *Journal of Non-Crystalline Solids* 416 (2015), pp. 44–49.

[38] Laura Fiocco, Hamada Elsayed, Letizia Ferroni, Chiara Gardin, Barbara Zavan, and Enrico Bernardo. "Bioactive wollastonite-diopside foams from preceramic polymers and reactive oxide fillers." In: *Materials* 8.5 (2015), pp. 2480–2494.

[39] L Fiocco, B Michielsen, and E Bernardo. "Silica-bonded apatite scaffolds from calcite-filled preceramic polymers." In: *Journal of the European Ceramic Society* 36.13 (2016), pp. 3211–3218.

[40] L Fiocco, H Elsayed, D Badocco, P Pastore, D Bellucci, V Cannillo, R Detsch, AR Boccaccini, and E Bernardo. "Direct ink writing of silica-bonded calcite scaffolds from preceramic polymers and fillers." In: *Biofabrication* 9.2 (2017), p. 025012.

[41] Hamada Elsayed, Paolo Colombo, and Enrico Bernardo. "Direct ink writing of wollastonite-diopside glass-ceramic scaffolds from a silicone resin and engineered fillers." In: *Journal of the European Ceramic Society* 37.13 (2017), pp. 4187–4195.

[42] Laura Fiocco, Stefano Agnoli, Danilo Pedron, Michele Secco, Sergio Tamburini, Letizia Ferroni, Chiara Gardin, Barbara Zavan, and Enrico Bernardo. "Wollastonite-diopside-carbon composite foams from a silicone resin and inorganic fillers." In: *Ceramics International* 44.1 (2018), pp. 931–937.

[43] Hamada Elsayed, Francesco Carraro, Stefano Agnoli, Devis Bellucci, Valeria Cannillo, Letizia Ferroni, Chiara Gardin, Barbara Zavan, and Enrico Bernardo. "Direct ink writing of silica-carbon-calcite composite scaffolds from a silicone resin and fillers." In: *Journal of the European Ceramic Society* 38.15 (2018), pp. 5200–5207.

[44] Wanyin Zhai, Hongxu Lu, Chengtie Wu, Lei Chen, Xiaoting Lin, Kawazoe Naoki, Guoping Chen, and Jiang Chang. "Stimulatory effects of the ionic products from Ca–Mg–Si bioceramics on both osteogenesis and angiogenesis in vitro." In: *Acta biomaterialia* 9.8 (2013), pp. 8004–8014.

[45] PN De Aza, F Guitian, and S De Aza. "Bioactivity of wollastonite ceramics: in vitro evaluation." In: *Scripta metallurgica et materialia* 31.8 (1994), pp. 1001–1005.

[46] Piedad N De Aza, Zofia B Luklinska, and Michel Anseau. "Bioactivity of diopside ceramic in human parotid saliva." In: *Journal of Biomedical Materials Research Part B: Applied Biomaterials: An Official Journal of The Society for Biomaterials, The Japanese Society for Biomaterials, and The Australian Society for Biomaterials and the Korean Society for Biomaterials* 73.1 (2005), pp. 54–60.

[47] Naoto Saito, Kaoru Aoki, Yuki Usui, Masayuki Shimizu, Kazuo Hara, Nobuyo Narita, Nobuhide Ogihara, Koichi Nakamura, Norio Ishigaki, Hiroyuki Kato, et al. "Application of carbon fibers to biomaterials: a new era of nano-level control of carbon fibers after 30-years of development." In: *Chemical Society Reviews* 40.7 (2011), pp. 3824–3834.

[48] Richard Petersen. "Carbon fiber biocompatibility for implants." In: *Fibers* 4.1 (2016), p. 1.

[49] Kathy L Elias, Rachel L Price, and Thomas J Webster. "Enhanced functions of osteoblasts on nanometer diameter carbon fibers." In: *Biomaterials* 23.15 (2002), pp. 3279–3287.

[50] Janice L McKenzie, Michael C Waid, Riyi Shi, and Thomas J Webster. "Decreased functions of astrocytes on carbon nanofiber materials." In: *Biomaterials* 25.7-8 (2004), pp. 1309–1317.

[51] Amir A Zadpoor. "Bone tissue regeneration: the role of scaffold geometry." In: *Biomaterials science* 3.2 (2015), pp. 231–245.

[52] Saber Amin Yavari, Johan van der Stok, Yoke Chin Chai, Ruben Wauthle, Zeinab Tahmasebi Birgani, Pamela Habibovic, Michiel Mulier, Jan Schrooten, Harrie Weinans, and Amir Abbas Zadpoor. "Bone regeneration performance of surface-treated porous titanium." In: *Biomaterials* 35.24 (2014), pp. 6172–6181.

[53] Gagandeep Kaur, Chao Wang, Jian Sun, and Qian Wang. "The synergistic effects of multivalent ligand display and nanotopography on osteogenic differentiation of rat bone marrow stem cells." In: *Biomaterials* 31.22 (2010), pp. 5813–5824.

[54] Megan S Lord, Morten Foss, and Flemming Besenbacher. "Influence of nanoscale surface topography on protein adsorption and cellular response." In: *Nano Today* 5.1 (2010), pp. 66–78.

[55] Monika Rumpler, Alexander Woesz, John WC Dunlop, Joost T Van Dongen, and Peter Fratzl. "The effect of geometry on three-dimensional tissue growth." In: *Journal of the Royal Society Interface* 5.27 (2008), pp. 1173–1180.

[56] Masahide Terazima, Noboru Hirota, Silvia E Braslavsky, Andreas Mandelis, Stephen E Bialkowski, Gerald J Diebold, RJD Miller, Danièle Fournier, Richard A Palmer, and Andy Tam. "Quantities, terminology, and symbols in photothermal and related spectroscopies (IUPAC Recommendations 2004)." In: *Pure and applied chemistry* 76.6 (2004), pp. 1083–1118.

[57] HMCM Herath, JA Epaarachchi, MM Islam, W Al-Azzawi, J Leng, and F Zhang. "Structural performance and photothermal recovery of carbon fibre reinforced shape memory polymer." In: *Composites Science and Technology* 167 (2018), pp. 206–214.

[58] Jonathan Fang and Yu-Chie Chen. "Nanomaterials for photohyperthermia: a review." In: *Current pharmaceutical design* 19.37 (2013), pp. 6622–6634.

[59] Peter Wust, B Hildebrandt, G Sreenivasa, B Rau, J Gellermann, H Riess, R Felix, and PM Schlag. "Hyperthermia in combined treatment of cancer." In: *The lancet oncology* 3.8 (2002), pp. 487–497.

[60] Dennis EJGJ Dolmans, Dai Fukumura, and Rakesh K Jain. "Photodynamic therapy for cancer." In: *Nature reviews cancer* 3.5 (2003), pp. 380–387.

[61] Amandine Pinto and Marc Pocard. "Photodynamic therapy and photothermal therapy for the treatment of peritoneal metastasis: a systematic review." In: *Pleura and peritoneum* 3.4 (2018).

[62] Feifan Zhou, Xing Da, Zhongmin Ou, Baoyan Wu, Daniel E Resasco, and Wei R Chen. "Cancer photothermal therapy in the near-infrared region by using single-walled carbon nanotubes." In: *Journal of biomedical optics* 14.2 (2009), p. 021009.

[63] Hongshi Ma, Chuan Jiang, Dong Zhai, Yongxiang Luo, Yu Chen, Fang Lv, Zhengfang Yi, Yuan Deng, Jinwu Wang, Jiang Chang, et al. "A bifunctional biomaterial with photothermal effect for tumor therapy and bone regeneration." In: *Advanced Functional Materials* 26.8 (2016), pp. 1197–1208.

[64] Shengyang Fu, Haoran Hu, Jiajie Chen, Yufang Zhu, and Shichang Zhao. "Silicone resin derived larnite/C scaffolds via 3D printing for potential tumor therapy and bone regeneration." In: *Chemical Engineering Journal* 382 (2020), p. 122928.

[65] Tanglong Zhu, Min Zhu, and Yufang Zhu. "Fabrication of forsterite scaffolds with photothermal-induced antibacterial activity by 3D printing and polymer-derived ceramics strategy." In: *Ceramics International* (2020).

[66] Andrea Zocca, Paolo Colombo, Cynthia M Gomes, and Jens Günster. "Additive manufacturing of ceramics: issues, potentialities, and opportunities." In: *Journal of the American Ceramic Society* 98.7 (2015), pp. 1983–2001.

[67] ASTM Standard. "F2792. 2012." In: *Standard Terminology for Additive Manufacturing Technologies, ASTM, West Conshohocken, PA* (2012).

[68] Nahum Travitzky, Alexander Bonet, Benjamin Dermeik, Tobias Fey, Ina Filbert-Demut, Lorenz Schlier, Tobias Schlordt, and Peter Greil. "Additive manufacturing of ceramic-based materials." In: *Advanced Engineering Materials* 16.6 (2014), pp. 729–754.

[69] Tobias Schlordt, Stanislaus Schwanke, Felix Keppner, Tobias Fey, Nahum Travitzky, and Peter Greil. "Robocasting of alumina hollow filament lattice structures." In: *Journal of the European Ceramic Society* 33.15-16 (2013), pp. 3243–3248.

[70] Friedrich Wolff, Christoph Kugler, and Helmut Münstedt. "Viscoelastic properties of a silicone resin during crosslinking." In: *Rheologica acta* 50.11-12 (2011), pp. 917–924.

[71] Tatsuhiro Takahashi, Joachim Kaschta, and Helmut Münstedt. "Melt rheology and structure of silicone resins." In: *Rheologica acta* 40.5 (2001), pp. 490–498.

[72] Herbert Barthel, Michael Dreyer, Torsten Gottschalk-Gaudig, Victor Litvinov, and Ekaterina Nikitina. "Fumed silica–rheological additive for adhesives, resins, and paints." In: *Macromolecular Symposia*. Vol. 187. 1. Wiley Online Library. 2002, pp. 573–584.

[73] *Anton Paar website*. Anton Paar Germany GmbH. URL: https://www.anton-paar.com/ca-en/products/details/rheometer-mcr-102-302-502/dmta/.

[74] M. Sottoriva. "Ottimizzazione della manifattura additiva di scaffold a base vetrosa." Master's thesis. Università degli Studi di Padova, 2019.

[75] Zongwen Fu, Matthias Freihart, Tobias Schlordt, Tobias Fey, Torsten Kraft, Peter Greil, and Nahum Travitzky. "Robocasting of carbon-alumina core-shell composites using co-extrusion." In: *Rapid Prototyping Journal* (2017).

[76] *X-Ray Diffraction – Bruker D8 discover*. Katholieke Universiteit Leuven. URL: https://fys.kuleuven.be/iks/nvsf/experimental-facilities/x-ray-diffraction-2013-bruker-d8-discover.

[77] Paolo Mazzoldi, Massimo Nigro, and Cesare Voci. *Elementi di fisica - Elettromagnetismo e onde*. EdiSES, 2008.

[78] *NC-Viewer*. URL: https://ncviewer.com/.

[79] Enrico Bernardo. *Dispense del corso Material Selection and Design*. Lecture notes. Università degli Studi di Padova, 2018-2019, p. 115.

[80] Xigeng Miao, Dawn Meifang Tan, Jian Li, Yin Xiao, and Ross Crawford. "Mechanical and biological properties of hydroxyapatite/tricalcium phosphate scaffolds coated with poly (lactic-co-glycolic acid)." In: *Acta Biomaterialia* 4.3 (2008), pp. 638–645.

[81] Xigeng Miao, L-P Tan, L-S Tan, and Xiao Huang. "Porous calcium phosphate ceramics modified with PLGA–bioactive glass." In: *Materials Science and Engineering: C* 27.2 (2007), pp. 274–279.

[82] Hui Gang Zhang and Qingshan Zhu. "Preparation of porous hydroxyapatite with interconnected pore architecture." In: *Journal of Materials Science: Materials in Medicine* 18.9 (2007), pp. 1825–1829.

[83] HY Yang, XP Chi, S Yang, and Julian RG Evans. "Mechanical strength of extrusion freeformed calcium phosphate filaments." In: *Journal of Materials Science: Materials in Medicine* 21.5 (2010), pp. 1503–1510.

[84] Fengzhang Ren, Gangjun Zhai, Zhanhong Ma, Xiaobo Chen, and Alex A Volinsky. "Microstructure and quality of SiC foam filters for casting." In: *Journal of Ceramic Processing Research* 12.6 (2011), pp. 691–694.

[85] Fengzhang Ren, Gangjun Zhai, Zhanhong Ma, Alex A Volinsky, and Baohong Tian. "Recoating slurry process effects on the SiC-based casting foam filter properties." In: *J. Ceram. Process. Res* 15 (2014), pp. 71–75.

[86] E Bernardo, P Colombo, and S Hampshire. "SiAlON-based ceramics from filled preceramic polymers." In: *Journal of the American Ceramic Society* 89.12 (2006), pp. 3839–3842.

[87] Giorgia Franchin, Halide Selin Maden, Larissa Wahl, Andrea Baliello, Marco Pasetto, and Paolo Colombo. "Optimization and characterization of preceramic inks for direct ink writing of ceramic matrix composite structures." In: *Materials* 11.4 (2018), p. 515.

[88] Xin Liu, Mohamed N Rahaman, Gregory E Hilmas, and B Sonny Bal. "Mechanical properties of bioactive glass (13-93) scaffolds fabricated by robotic deposition for structural bone repair." In: *Acta biomaterialia* 9.6 (2013), pp. 7025–7034.

[89] Michael Paris, Andreas Götz, Inga Hettrich, Cécile M Bidan, John WC Dunlop, Hajar Razi, Ivo Zizak, Dietmar W Hutmacher, Peter Fratzl, Georg N Duda, et al. "Scaffold curvature-mediated novel biomineralization process originates a continuous soft tissue-to-bone interface." In: *Acta biomaterialia* 60 (2017), pp. 64–80.